Investigations of the Effect of Transition Metal Substitution on the Pre-edge of X-ray Absorption Near-Edge Spectra

A thesis submitted to the College of Graduate and Studies and Research

in partial fulfillment of the requirements for the

Degree of Master of Science

in the Department of Chemistry

University of Saskatchewan

Saskatoon

By

John R. Hayes

PERMISSION TO USE

In presenting this thesis/dissertation in partial fulfillment of the requirements for a Postgraduate degree from the University of Saskatchewan, I agree that the Libraries of this University may make it freely available for inspection. I further agree that permission for copying of this thesis/dissertation in any manner, in whole or in part, for scholarly purposes may be granted by the professor or professors who supervised my thesis/dissertation work or, in their absence, by the Head of the Department or the Dean of the College in which my thesis work was done. It is understood that any copying or publication or use of this thesis/dissertation or parts thereof for financial gain shall not be allowed without my written permission. It is also understood that due recognition shall be given to me and to the University of Saskatchewan in any scholarly use which may be made of any material in my thesis/dissertation.

Requests for permission to copy or to make other uses of materials in this thesis/dissertation in whole or part should be addressed to:

Head of the Department of Chemistry
University of Saskatchewan
Saskatoon, Saskatchewan
S7N 5C9, Canada

OR

Dean
College of Graduate Studies and Research
University of Saskatchewan
107 Administration Place
Saskatoon, Saskatchewan S7N 5A2
Canada

"Every passing hour brings the Solar System forty three thousand miles closer to Globular Cluster M13 in Hercules— and still there are some misfits who insist that there is no such thing as progress."

– Kurt Vonnegut, *The Sirens of Titan*

ACKNOWLEDGEMENTS

While there are many people who I would like to thank for their help in completing this thesis, I would be remiss if I did not mention my family first. To my parents: Mom and Dad, I wouldn't be here if it wasn't for you (quite literally). Thank you very much for all your love and support throughout my entire academic career. Your advice and encouragement helped me understand that the difficult times are worth working through and the good times are worth savouring, and for this I am eternally grateful. I would also like to thank my brother Jeff, who through his love of theatre, helped teach me the value of art and the study of the human condition. My extended family has also been instrumental in helping me write this thesis. To my grandparents, Dinny and Gary, words fail me, and I cannot express how deeply grateful I am to have had your love and support over the last two years. You helped me adjust to life in Saskatoon, making a difficult transition easier. I appreciated being able to go to a familiar place when the city was unfamiliar, and Sunday dinners often provided much-needed rest and relaxation.

Over the course of my academic career, I have been fortunate to have had a large number of brilliant and nurturing advisors. To all these teachers, I am thankful. In the case of this thesis, my supervisor, Dr. Andrew Grosvenor, has provided immeasurable amounts of support and guidance. Andrew, thank you very much for the challenge and drive you provided. You guidance helped me achieve more than I ever thought I could. I would also like to thank my fellow Grosvenor Group members, both past and present. I think our group is unique in that beamtime, and all the fatigue associated with it, is a shared experience, regardless of whose samples are being run. Without my groupmates' support, I am sure this thesis would not have been possible. I would especially like to thank James Walker, who helped collect the spectra presented in Chapter 3. The work in this thesis has also been greatly enhanced by the advice and wisdom of a large number of other scientists as well. Dr. Weifeng Chen and Dr. Ning Chen are thanked for their help in carrying out experiments on the HXMA beamline at the CLS. Dr. Ning Chen is also thanked for his help in carrying out electronic structure calculations as well. I would like to thank Dr. Yongfeng Hu for his help in completing the experiments using the SXRMB beamline at the CLS. Mr. Thomas Regier and Mr.

David Chevrier are thanked for the guidance they provided while the experiments using the SGM beamline at the CLS were completed. Finally, I would like to thank Dr. Robert Gordon for his help in completing the experiments performed using the 20-BM beamline at the APS. I would also like to thank Dr. Gordon for showing me the glory that is Whole Foods, and for letting us make Spider-bike.

While completing this thesis, I have had the good fortune to meet and befriend a large number of interesting and helpful people, and no Acknowledgments section could ever do these friends justice. (It would end up being longer than the thesis itself!) To all my friends: please know that you have my gratitude, and that you have added the much-needed spice to life, turning my journey into an adventure! I would also like to take this opportunity to specifically thank my partner, Aimee. You have kept me sane while I have worked on this thesis, and you remind me to sit back and enjoy life. I am so happy to have met you out here (because really, what were the odds?), and I love you so much.

Finally, I have to thank the organizations that have provided the funding for the work done in this thesis. I thank the National Science and Engineering Research Council (NSERC) for financial support through the Canada Graduate Scholarship program and the University of Saskatchewan for support through the Herzberg Memorial Scholarship program. The Canadian Foundation for Innovation (CFI) is thanked for providing funds to purchase the PANalytical Empyrean powder X-ray diffractometer used in this work. PNC/XSD facilities at the Advanced Photon Source, and research at these facilities, are supported by the US Department of Energy - Basic Energy Sciences, a Major Resources Support grant from NSERC, the University of Washington, the Canadian Light Source and the Advanced Photon Source. Use of the Advanced Photon Source, an Office of Science User Facility operated for the U.S. Department of Energy (DOE) Office of Science by Argonne National Laboratory, was supported by the U.S. DOE under Contract No. DE-AC02-06CH11357. The CLS is supported by NSERC, the National Research Council of Canada, the Canadian Institutes of Health Research, the Province of Saskatchewan, Western Economic Diversification Canada, and the University of Saskatchewan.

ABSTRACT

Transition-metal K-edge X-ray absorption spectroscopy (XAS) describes a group of techniques that are element specific and provide information about the chemical environments and structures in a material. X-ray Absorption Near-Edge spectroscopy (XANES) is a particularly useful XAS technique as it provides information regarding the chemical environment of a transition-metal centre and the electronic structure of the material being studied. As such, XANES has found use in a variety of scientific fields including biochemistry, geochemistry, and fundamental physics. One particularly information rich region of a transition-metal K-edge XANES spectrum is the pre-edge region, which contains information about the oxidation state and coordination environment of the transition-metal. Due to the wealth of information contained in the pre-edge region, it is important to fully understand all the features contained in this region and the factors that may affect them. To this end, a series of studies have been performed, with the goal of increasing the understanding of the pre-edge region of transition-metal K-edge spectra and how it may be used to characterize a material.

A series of $Sr_2Fe_{2-x}Mo_xO_6$ ($0.25 \leq x \leq 1.0$) double perovskites have been studied in order to investigate how changes in the oxidation state and coordination environment may be studied when both change simultaneously. These materials were also studied due to their technological relevance, as the Sr_2FeMoO_6 double perovskite has been widely studied due to its interesting and technologically relevant physical properties. However, Sr_2FeMoO_6 is just a single composition in the $Sr_2Fe_{2-x}Mo_xO_6$ solid-solution, and it is important to understand how the composition impacts the transition metal valence states. Fe K- and Mo K-edge X ray absorption near-edge spectra have been collected to investigate how the oxidation state and coordination environment change with composition. When the Mo content is low, Fe adopts a 3+ oxidation state and Mo adopts a 6+ oxidation state. As the Mo content is increased, the Fe and Mo cations are both partially reduced, resulting in a mixture of Fe^{3+} and Fe^{2+} and Mo^{5+} and Mo^{6+}. The reduction of the metal centers apparently drives a change in unit cell from a cubic $Fm\bar{3}m$ structure to a tetragonal $I4/m$ structure. The results reported here show that by careful analysis of the pre-edge, simultaneous changes in

the oxidation state and coordination number may be discerned and analyzed separately.

In order to study the effects on the pre-edge from changes in the spin-state of the transition-metal centre and variations in the metal-ligand bond covalency, a series of $Cu_2FeSn_{3-x}Ti_xS_8$ thiospinels have been studied. The $Cu_2FeSn_{3-x}Ti_xS_8$ thiospinels exhibit an interesting magnetic phenomenon known as a spin-crossover transition (SCO), in which the Fe^{2+} transitions from a low spin state to a high-spin state (or vice versa). The effects of such a transition on the XANES spectrum has been studied by collecting a series of Fe K-edge XANES spectra at varying temperatures. Further, XANES has been used to investigate the changes in the electronic structure of these materials as Ti is substituted for Sn. The room-temperature Fe K-edge XANES spectra showed that the pre-edge intensity increased with increasing Ti content as a result of the Fe–S bond becoming more covalent. (Ti K- and S K-edge XANES spectra, supported by electronic structure calculations, confirmed this analysis.) Temperature-dependent Fe K-edge XANES spectra were also collected to study the SCO transition and showed that the main-edge features decreased in intensity with decreasing temperature, corresponding to variations in the average Fe^{2+} spin-state.

The rare-earth orthoferrites ($REFeO_3$, RE = rare-earth, Y) were studied in order to understand the relationship between the Fe–O–Fe bond angle and an ill-studied feature known as an intersite-hybrid peak contained in the Fe K-edge spectra of some materials. This feature is attributed to non-local transitions of Fe 1s electrons to Fe 3d states on the next-nearest-neighbor atom that are hybridized with Fe 4p states on the absorbing atom through O 2p states. In this study, it is shown that the intensity of this feature is strongly dependent on the Fe–O–Fe bond angle; the lower the Fe–O–Fe bond angle, the less intense the intersite-hybrid peak is. Fe L- and O K-edge XANES spectra were also collected in order to investigate the electronic structure of these technologically relevant materials.

Contents

List of Figures

List of Abbreviations

APS	Advanced Photon Source
CLS	Canadian Light Source
CMR	Colossal Magnetoresistance
CN	Coordination Number
COHP	Crystal Orbital Hamiltonian Population
ΔE_{HL}	High-spin to low-spin transition energy
DOS	Density of States
E_c	Bending Magnet and Wiggler Critical Energy
EXAFS	Extended X-ray Absorption Fine Structure
HS	High Spin
LS	Low Spin
MSR	Multiscattering Resonance
$\mu(E)$	Absorption Coefficient
NNN	Next-nearest-neighbour
NSLS	National Synchrotron Light Source
SCO	Spin-Crossover Transition
TB-LMTO-ASA	Tight-Binding Linear Muffin Tin Orbital Atomic Spheres Approximation
TMR	Tunneling Magnetoresistance
VUV	Vacuum Ultra-Violet
XANES	X-ray Absorption Near-Edge Spectroscopy
XAS	X-ray Absorption Spectroscopy
XRD	X-ray Diffraction

Chapter 1

INTRODUCTION

Acquiring fundamental knowledge of the complex interactions present in solid-state materials is essential for the rational design and engineering of materials for use in a variety of applications, and is at the heart of solid-state chemistry. To facilitate a better understanding of a material, it is necessary to fully develop techniques which provide insight into the nature and origins of the material's structure and physical properties. One technique that is especially useful to this end is X-ray absorption spectroscopy (XAS), which involves using X-ray radiation to excite core-electrons to conduction and continuum states. While XAS experiments have been performed for many decades, a complete understanding of how the features found in XAS spectra relate to the structure and physical properties of a material has yet to be achieved.

The focus of this thesis will be the exploration of how the features contained in the pre-edge region of a transition-metal K-edge XAS spectrum may be used to characterize the changes that occur within a material upon metal substitution. This thesis will discuss how changes in the pre-edge features can be analyzed to determine how both the oxidation state and coordination number of a metal center change with substitution through a study of $Sr_2Fe_{2-x}Mo_xO_6$ double perovskites (Chapter 2). The relationship between the pre-edge intensity and the covalency of the bond between the transition-metal centre and its neighboring ligands will be examined by studying the $Cu_2FeSn_{3-x}Ti_xS_8$ spin-crossover materials (Chapter 3). Finally, the relationship between the struc-

ture of a material and the intensity of a poorly understood pre-edge feature known as an intersite-hybrid peak will be illustrated by considering XAS spectra from a series of rare-earth orthorferrites (Chapter 4).

1.1 X-ray Absorption Spectroscopy: An Overview

X-ray absorption spectroscopy describes a group of powerful techniques that provide information about the structure and chemical environments in a material. The use of XAS techniques has flourished concurrently with the development of next-generation synchrotron radiation sources, higher-quality X-ray optics, and highly adaptable experimental set-ups. To better understand the experiments performed in this thesis, an overview of the theory and methods behind XAS will be presented.

1.1.1 XANES and EXAFS

X-ray absorption spectroscopy describes a set of techniques in which monochromatic X-rays are used to excite core-shell electrons to conduction or continuum states. Because core-state electrons are being excited, the technique is element specific and the spectra are highly sensitive to the oxidation state and chemical environment of the absorbing atom [1–3]. As such, XAS techniques have found use in a variety of fields, including materials science, earth science, and the life sciences [2, 4, 5]. An example of an XAS spectrum, the Fe K-edge from Fe_2O_3, is presented in Figure 1.1a. There is a large jump in the absorption coefficient at 7126.5 eV, and this feature is called an absorption edge [1–3]. The region starting just before the absorption edge and ending just after the absorption edge is often referred to as the X-ray absorption near-edge structure (XANES) region. Oscillations in the absorption spectrum are observed at energies higher than the absorption edge, and these oscillations are referred to as extended X-ray absorption fine structure (EXAFS). While XANES and EXAFS each represent one part of a total XAS spectrum, it is often beneficial to discuss the theory behind each phenomenon separately.

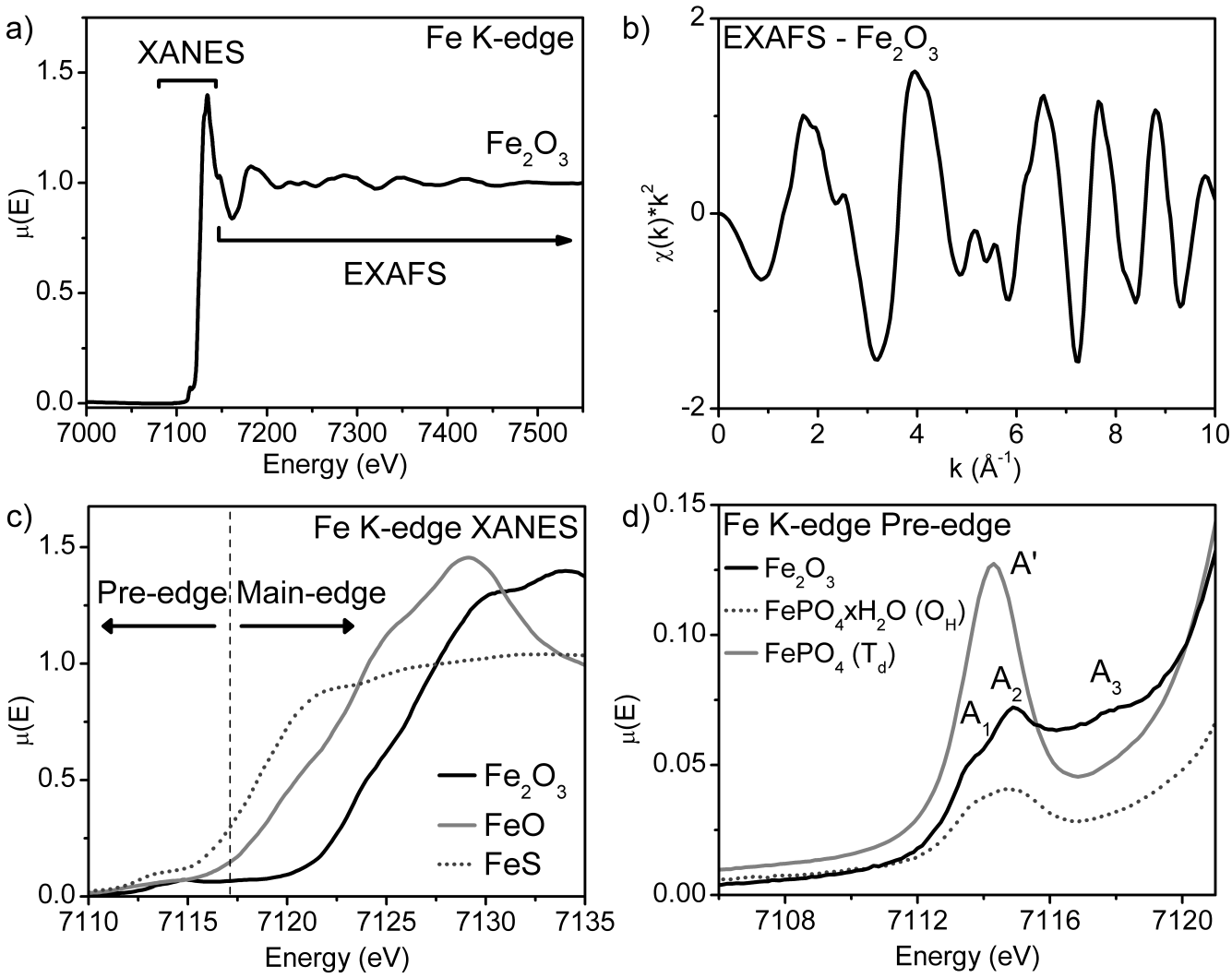

Figure 1.1: (a) The full Fe K-edge XAS spectrum from Fe_2O_3 is presented and may be divided into two regions: the XANES spectrum and the EXAFS spectrum. (b) The k-weighted EXAFS spectrum from the Fe K-edge of Fe_2O_3 is plotted as a function of *k*. These oscillations are a result of photoelectron interference patterns and can be used to determine the local structure around the absorbing Fe centre. (c) The Fe K-edge XANES spectrum from Fe_2O_3 is plotted with the Fe K-edge spectra from FeO and FeS. These spectra are divided into two regions: the main-edge and the pre-edge. Shifts in main-edge energy are observed when the oxidation state and coordinating ligands are changed. (d) The pre-edge of the Fe K-edge spectrum from Fe_2O_3 is compared to pre-edges from $FePO_4 \cdot xH_2O$ and $FePO_4$. Large changes in the lineshape and intensity are observed when the coordination geometry changes.

1.1.1.1 EXAFS

The EXAFS phenomenon is observed when a core electron is excited out of the atom. This photoelectron can scatter off the neighboring atoms [3,6,7]. If the scattering path includes the absorbing atom, then constructive and destructive interference of the photoelectron wave-function may occur, increasing or decreasing the probability of absorption [3, 6, 7]. Generally, the oscillations in intensity are plotted in *k*-space, as shown in Figure 1.1b. (*k* is the magnitude of the wave vector of the photoelectron and has units of $Å^{-1}$.) Assuming that there is no polarization dependence, and that the spectra are collected at low temperatures, the EXAFS may be expressed as [3, 6–8]:

$$\chi(k) = \sum_j \frac{N_j}{kR_j^2} S_o^2 F_j(k) e^{-2k^2\sigma^2} e^{-2R_j/\lambda(k)} \sin\left[2kR_j + \psi(k)\right] \tag{1.1}$$

Here, N is the number of atoms at a distance R_j away from the absorbing atom. S_o is an amplitude factor, which is usually set at 0.7-0.9, and F_j is a backscattering factor for the neighboring atom and is dependent on the number of electrons in the scattering atom. The first exponential term, $e^{-2k^2\sigma^2}$, is a Debye-Waller factor which accounts for disorder in the system (both from thermal vibrations and structural disorder), while the second exponential term, $e^{-2R_j/\lambda(k)}$, accounts for the mean-free path of the electron [3, 6–8]. Structural information can be elicited from this equation by fitting models to the data and, from such an analysis, the bond-distances, coordination number, and the identity of the coordinating atoms may be determined [3, 6–8]. However, a full discussion of such an analysis is beyond the scope of this thesis.

1.1.1.2 XANES

In contrast to EXAFS, where the electron is excited out of the absorbing atom, the XANES spectrum is observed when the core-electron is excited into a bound or partially bound unoccupied conduction state (Figure 1.2) [1]. These spectra are referenced by the principle quantum number (n) of the electron being excited, as shown in Figure 1.2 [3,9,10]. In this thesis, only K-edge spectra (excitation of 1s electrons) and $L_{2,3}$-edge spectra (excitation of 2p electrons) will be considered.

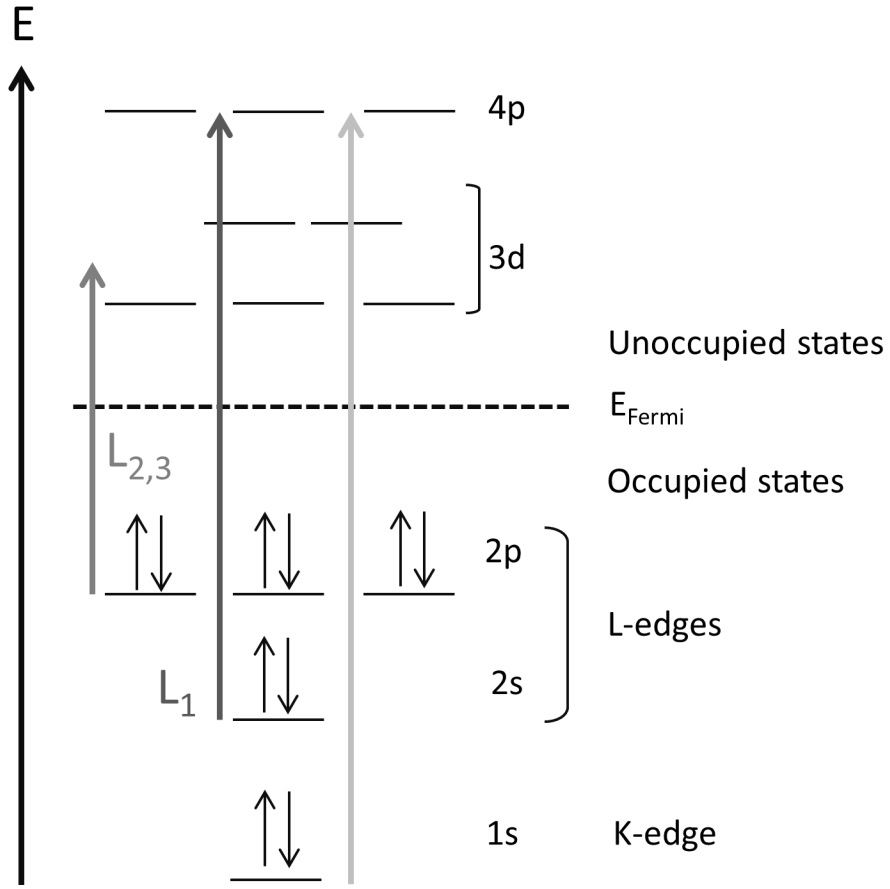

Figure 1.2: A typical energy diagram for transition-metal K- and L-edge XANES is shown. The K-edge mostly consists of 1s→np transitions (though 1s→3d transitions may occur) and the L_1 edge consists of 2s→ np transitions. The L_2 and L_3 edges occur when a 2p electron is excited into an (n-1)d state, and these edges are split by spin-orbit coupling.

The probability of a particular excitation occurring can be described using Fermi's Golden Rule [3, 10, 11]:

$$P = \frac{2\pi}{h} \left| \left\langle \Phi_f \left| \hat{T} \right| \Phi_i \right\rangle \right|^2 \delta_{E_F - E_i - \hbar\omega}. \tag{1.2}$$

Here, P is the probability of a transition, $\hbar$ is the reduced Planck's constant, $\hat{T}$ is the transition operator, δ is a Dirac delta-function, Φ_i and Φ_f are the initial- and final-state wavefunctions, respectively, E_f and E_i are the energies of the initial and final states, and ω is the angular frequency of the photon. $\hat{T}$ can be expressed as the sum of all the possible transition pathways (i.e. $\hat{T} = \hat{T}_1 + \hat{T}_2 + \hat{T}_3 \dots$) [1]. Here, only one-photon transitions will be considered, and the transition operator, $\hat{T}_1$, as a first approximation can be considered equal to the interaction Hamiltonian ($\hat{T}_1 = \hat{H}_1$). By considering the electric field of the photon, $\hat{T}_1$ can be expressed as:

$$\hat{T}_1 \propto \sum_q (\hat{\mathbf{e}}_\mathbf{q} \cdot \mathbf{p}) \, e^{i\mathbf{k}\cdot\mathbf{r}}. \tag{1.3}$$

where $\hat{\mathbf{e}}_\mathbf{q}$ is a unit vector indicating the polarization of the electric field, $\mathbf{p}$ is the momentum vector of the electron, and $\mathbf{k}$ is the wave-vector of the photon [1]. Expressing the exponential term as a Taylor expansion leads to:

$$\hat{T}_1 \propto \sum_q \left[(\hat{\mathbf{e}}_\mathbf{q} \cdot \mathbf{p}) + (\hat{\mathbf{e}}_\mathbf{q} \cdot \mathbf{p}) \, (i\mathbf{k} \cdot \mathbf{r}) + \dots \right]. \tag{1.4}$$

Here, the $(\hat{\mathbf{e}}_\mathbf{q} \cdot \mathbf{p})$ term expresses the electric dipole transition while the $(\hat{\mathbf{e}}_\mathbf{q} \cdot \mathbf{p})\,(i\mathbf{k} \cdot \mathbf{r})$ term expresses a quadrupolar transition [1]. In general, the quadrupolar term is 100 to 1000 times smaller than the electric dipole transition component and is often *approximated* to be 0 [1]. By incorporating this approximation, and considering the commutative relationship between the position operator and the atomic Hamiltonian, the transition operator can be as [1]:

$$\hat{T}_1 = \sum_q (\hat{\mathbf{e}}_\mathbf{q} \cdot \mathbf{r}). \tag{1.5}$$

Substituting Equation 1.5 in Equation 1.2 leads to an expression of Fermi's golden rule as:

$$P \propto \sum_{q} \left| \left\langle \Phi_f \left| (\hat{\mathbf{e}}_\mathbf{q} \cdot \mathbf{r}) \right| \Phi_i \right\rangle \right|^2 \delta_{E_F - E_i - \hbar\omega}. \tag{1.6}$$

The matrix element, $\left| \left\langle \Phi_f \left| (\hat{\mathbf{e}}_\mathbf{q} \cdot \mathbf{r}) \right| \Phi_i \right\rangle \right|^2$, is an integral over all space [1, 11, 12], i.e.,

$$\left| \left\langle \Phi_f \left| (\hat{\mathbf{e}}_\mathbf{q} \cdot \mathbf{r}) \right| \Phi_i \right\rangle \right| = \int \Phi_f \, (\hat{\mathbf{e}}_\mathbf{q} \cdot \mathbf{r}) \, \Phi_i d\tau. \tag{1.7}$$

Thus the matrix element may only be non-zero if the integrand in Equation 1.7 is an even function. The dipole operator, $(\hat{\mathbf{e}}_\mathbf{q} \cdot \mathbf{p})$, is an odd function, and therefore Φ_f must be an even function and Φ_i must be an odd function (or vice versa). (The product of an even function and an odd function is an odd function, while the product of two odd functions is an even function.) If a one-electron excitation process is assumed, then the only way to satisfy this symmetry requirement is if $\triangle l = \pm 1$, where l is the angular momentum number [1, 11, 12]. This result is often referred to as the dipolar selection rule, and is interpreted to result from the conservation of angular momentum [1, 11, 12]. It should be noted that this derivation indicates that quadrupolar transitions are allowed (the quadrupolar term of the transition operator was discarded as an approximation, see Equation 1.4), though they are expected to be much weaker than the dipolar transitions. Here, the Dirac delta function, $\delta_{E_F - E_i - \hbar\omega}$, maintains the conservation of energy and also implies that the probability of an excitation is proportional to the empty density of states (DOS) [1]. However, because exciting a core electron will result in the formation of a core hole, the XANES spectrum does not resemble the ground-state DOS, but instead resembles the DOS of a similar system where a Z+1 atom replaces the absorbing atom (Z is the atomic number of the probed atom) [1]. Further, the shape of the unoccupied DOS will also be convoluted by a Lorentzian function due to the finite core-hole lifetime, which limits the maximum attainable energy resolution, as per the Heisenberg uncertainty principle [1, 13].

Fe K-edge XANES spectra from Fe_2O_3, FeO, and FeS are presented in Figure 1.1c. These spectra are divided into two regions. The pre-edge, which arises from weak, quadrupolar Fe 1s

$\rightarrow$ Fe 3d states contains information about the oxidation state and coordination geometry around the excited atom [14–21]. (The pre-edge excitations also contain some ligand p character, which contributes dipolar character to these excitations.) The higher energy feature is the main-edge region, which consists of strong, dipolar Fe 1s $\rightarrow$ Fe 4p states and contains information about the oxidation state of the excited atom and some structural information [2, 5, 22–24].

The main-edge energy, defined as the inflection point of the lowest-energy most intense dipolar peak, is characteristic of the oxidation state of the material. A large change in the energy of the main-edge is often indicative of a change in the oxidation state, and the edge energy will increase as the oxidation state of an ion becomes more positive [2,5,22–25]. This is because an increase in the oxidation state reduces the amount of screening of the nucleus that the core electron experiences, increasing the amount of energy required to excite the electron away from the nucleus [2,5,22–25]. An example of this is shown in Figure 1.1c, where the absorption edge of FeO (Fe^{2+}) is found at much lower energy than that of Fe_2O_3 (Fe^{3+}). Similarly, changes in the electronegativity of neighboring atoms may also cause shifts of the edge energy. As the neighboring atoms become more electronegative, they withdraw electron density from the atom being probed. This will result in decreased screening of the nuclear charge, and the absorption-edge will be shifted to higher energy [2, 25, 26]. (The opposite trend will be observed if more electropositive neighbors are substituted into a system.) This is also illustrated in Figure 1.1c through a comparison of edge energies of FeS (Fe^{2+}) and FeO. (O is more electronegative than S [27].) In general, for transition-metal K-edge spectra, changes in the main-edge energy due to oxidation state versus changes due to variations in the electronegativity of the neighboring atoms may be distinguished by the magnitude of the change. Changes attributable to a varying oxidation state will generally be large (on the order of a few eV), while changes attributable to the electronegativity of the neighboring atoms are generally smaller [2, 5, 22–25].

The pre-edge region of a transition-metal K-edge spectrum provides information about the coordination environment and oxidation state of the absorbing metal centre [14–21]. Changes in the oxidation state of the transition metal will cause shifts in the energies of the pre-edge features,

similar to the main-edge [2, 24, 25]. More interesting though, is the information contained in the pre-edge regarding the coordination environment of the transition metal centre. When the degeneracy of the d-orbitals is broken by crystal field splitting, the line-shape of the pre-edge provides information on the coordination geometry and d-orbital occupancy of the transition-metal centre [17, 18, 28, 29]. Further, if inversion symmetry around the metal centre is lost, an increase in the intensity of the pre-edge will be observed as well [17, 18, 28, 29]. Losing inversion symmetry results in the local mixing of the transition-metal np and (n-1)d states, which increases the dipolar character of the excitation [17, 20, 21]. Because a small increase in dipolar character will have a large effect on the intensity, the increase in intensity is expected to be large even for very small increases in dipolar character. A comparison between octahedrally coordinated Fe in $FePO_4 \cdot H_2O$ and tetrahedrally coordinated Fe in $FePO_4$ is a good example of such behaviour (Figure 1.1d). In the Fe K-edge pre-edge from $FePO_4 \cdot H_2O$, two features (A_1 and A_2) are observed, and these arise from excitations to Fe 3d t_{2g} and Fe 3d $e_g{}^*$ states, respectively [28, 30]. When the coordinating water molecules are removed, the Fe occupies a tetrahedral site, and the line shape changes to reflect the new distribution of Fe 3d states [28]. Further, a large increase in intensity is observed, due to the increased dipolar character of the final states. Thus, by tracking changes in the lineshape and intensity of the pre-edge features, insight on changes in the oxidation state and oxygen deficiency in very complicated systems can be achieved. The study the $Sr_2Fe_{2-x}Mo_xO_6$ double perovskites presented in Chapter 2 details such an analysis.

Interestingly, in some oxides such as TiO_2, $Fe_{1-x}Ga_xSbO_4$ and $TbMnO_3$ (which is structurally analogous to the rare-earth orthoferrites discussed in this thesis), an anomalous structure has been observed that cannot be explained only by local 1s $\rightarrow$ (n-1)d transitions [15, 19, 22, 31–33]. This feature is also observed in Fe_2O_3 and is labeled as A_3 in Figure 1.1d. It has been proposed that this spectral feature, dubbed an intersite hybrid, is a result of excitations to non-local states arising from np states on the excited metal atom (M) interacting with (n-1)d states of next-nearest-neighbour (NNN) metal atoms (M') through O 2p states (M np–O 2p–M' (n-1)d) [15, 31, 32]. The mixing of NNN (n-1)d states with np states on the absorbing atom provides some dipolar character to

this excitation, which makes it discernible from the weak pre-edge structure resulting primarily from local quadrupolar 1s $\rightarrow$ (n-1)d transitions. It has been shown that the intersite hybrid peak is observed only when the M–O–M' bond angle is greater than 90°; however, no systematic study has been performed to study how the intersite hybrid peak is affected by changes in this angle [14]. This relationship was thoroughly investigated in the study of the $REFeO_3$ orthoferrites presented in Chapter 4.

1.1.2 Generating Synchrotron Radiation

While Schott first theorized synchrotron radiation in 1912, it became relevant in the 1940s when circular accelerators began to be developed with energies high enough for synchrotron radiation effects to be significant [34, 35]. When synchrotron radiation was first observed in 1947 at the General Electric Research Laboratory in Schenectady, New York, it was initially regarded as an unfortunate energy loss mechanism rather than as a tool for research [35]. (Interestingly, synchrotron radiation is named after the GE accelerator, independently dubbed a synchrotron, though both Schott and Schwinger developed their descriptions of the theory before the device was invented.) It was not until 1953 that the first experiments utilizing synchrotron radiation were performed, and in 1954, the first absorption spectrum collected using synchrotron radiation was reported by Tomboulain and Johnston at Cornell [35, 36].

Initial experiments using the parasitic synchrotron radiation from particle accelerators designed for high-energy physics experiments, were tenuous due to the operation schedules of the accelerators, which were tailored for particle physics experiments. Further, the lattices for these accelerators (i.e., the arrangement of the magnets which direct and accelerate the particle beams) were not optimized to produce synchrotron radiation [34, 35]. The idea of dedicated synchrotron light sources was first realized in the mid-1970s when Chasman and Green designed a lattice that was specifically optimized for the generation of bright synchrotron radiation by decreasing the horizontal emittance of the electron beam [34, 37]. (The emittance is essentially a measure of the width and angular divergence of the electron beam.) Brightness is defined as photons/s/mm^2/mrad^2/0.1%

bandwidth (where 0.1% bandwidth indicates only photons with energies of $\pm 0.1\%$ of a specified energy), and is important because it is characteristic of the light source and cannot be improved using optics [9, 10, 38]. The Chasman-Green lattice is now used in both second-generation synchrotron sources, such as the National Synchrotron Light Source (NSLS) at the Brookhaven National Laboratory, and modern-day third generation synchrotron sources such as the Advanced Photon Source (APS).[1]

Synchrotron radiation is generated when electrons moving at relativistic speeds are accelerated around a curve, and it is characterized by its high intensity and narrow divergence [10, 34, 38]. In general, a charged particle will emit radiation when accelerated, and this radiation will be emitted radially away from the direction of acceleration, forming a donut-like shape. This same phenomenon occurs in a synchrotron, and in the reference frame of the accelerated particle, the emitted pattern still resembles the radial donut shape. However, from the reference frame of the laboratory, the radiation will appear to be focused into a narrow cone that is emitted tangential to the path of the electron [10, 34, 38]. Thus, the relativistic effects create the high-intensity photon beams that characterize synchrotron radiation.

A series of accelerators are used in order to accelerate electrons to the relativistic speeds required to generate synchrotron light at most synchrotron facilities. At the Canadian Light Source (CLS), the journey of an electron first begins at a linear accelerator. The linear accelerator accelerates the electrons to 250 MeV. These high-energy electrons are then injected into a circular accelerator called a booster ring, which further accelerates them to 2.9 GeV. Once the electrons have been accelerated to 2.9 GeV, they are injected into the storage ring, which is where they are used to produce light. The storage ring consists of alternating straight sections and bends. The storage ring also contains a radio frequency (RF) cavity, which compensates for the electron energy lost to synchrotron radiation as electrons travel around the storage ring.

The electron beam is curved using dipolar bend magnets. In addition to causing the electron beam to curve, these bend magnets also produce light (because the electrons are changing direc-

[1] For further information regarding the development dedicated synchrotron radiation facilities the reader is referred to the fascinating account of the challenges of building the NSLS given by Crease in [35, 39].

tion) and this light can be used for experiments. The emission spectrum of the light produced by a bend magnet is broad, and depends on both radius of the turn (the bend magnet field strength) and the energy of the beam. Bend magnet sources are often characterized by a parameter referred to as the critical energy, E_c [10, 38]. The critical energy is defined as the energy where all the light below this energy accounts for half of the instantaneous power of the beam. It may be expressed as:

$$E_c = \frac{3\hbar c\gamma^3}{\rho} = 0.665 B_o E^2 \tag{1.8}$$

where c is the speed of light, $\hbar$ is reduced Planck's constant, ρ is the bend-magnet radius, B_o is the magnetic field strength, and γ is the relativistic factor [38]. γ is expressed as:

$$\gamma = \frac{1}{\sqrt{1-(v/c)^2}} \tag{1.9}$$

where v is the electron velocity [10, 38]. The maximum energy at which useable flux may be collected is usually $4E_c$. In convenient units, Equation (1.8) may be expressed as:

$$E_c(keV) = 0.665 B_o(T) E^2(GeV) \tag{1.10}$$

From Equations (1.8) and (1.10), it can be seen that E_c may be increased by decreasing the bend radius (increasing the magnetic field) or increasing the electron energy. However, neither option is easily realized, as changing the electron energy requires extreme redesign of the storage ring, and increasing the bend magnet strength often results in an increased electron beam emittance (which lowers the overall possible brightness of the beam) [37, 38]. However, superbend magnets, which use magnetic fields of up to 5 T do exist (most notably at the Advanced Light Source), and may be used to generate high-energy X-rays from relatively low-energy storage rings [40].

While bend magnets are the most obvious way to generate synchrotron light, it may also be produced in the straight sections by using magnetic arrays known as insertion devices. Insertion devices may be separated into two categories, wigglers and undulators, though both are related and

represent two extremes of a continuous gradient [10, 34, 38, 41]. Both types of insertion devices consist of a series of magnets with alternating dipoles aligned so that the oscillating magnetic field is perpendicular to the path of the electron beam. Wiggler and undulators are characterized by the strength of the magnetic field generated by these arrays and the number of magnets (which characterizes the magnetic period). These properties can be quantified using the dimensionless K-factor, which describes the deflection of the electrons, and is expressed as:

$$K = \frac{e}{2\pi m_e c} B_o \lambda_p, \tag{1.11}$$

where e is the charge of an electron, m_e is the mass of the electron, and λ_p is the magnetic period [9, 10, 34, 38, 41]. The K-factor has physical relevance as it can be used to describe the maximum angular deflection of the electron beam. Wigglers consist of a few strong magnets (i.e. large magnetic period and strong field strength), and the electrons travel on a path with a small number of large amplitude oscillations [9, 10, 34, 38, 41]. As a result, $K \gg 1$ in a wiggler. Wigglers produce a broad spectrum of high intensity light over a broad horizontal fan [9, 10, 34, 38, 41]. While the emission spectrum from a wiggler resembles that of a bend magnet, a wiggler produces light with greater brightness than a bend magnet [9, 10, 34, 38, 41]. E_c is expressed by Equation 1.8 for a wiggler, and in general, because stronger magnets can be used in a wiggler without significant distortion of the electron beam shape, E_c is higher for wigglers than for bend magnets [9, 10, 34, 38, 41].

In contrast to a wiggler, an undulator uses a large number of weak magnets (i.e. small magnetic period and weak field strength) and $K \sim 1$. This causes the electrons to follow a path with a large number of small-amplitude oscillations [9, 10, 34, 38, 41]. Interestingly, the oscillations are small enough that the light cones emitted from each oscillation may begin to interact with each other coherently [9, 10, 34, 38, 41]. The resulting constructive and destructive interference results in the formation of narrow emission regions (harmonics) which is very bright (relative to wigglers and

bend magnets). The wavelength of the nth harmonic is given by:

$$\lambda_n = \frac{\lambda_p}{2n\gamma^2}\left(1+\frac{K^2}{2}+\gamma^2\theta_{obs}^2\right) n = 1,2,3..., \tag{1.12}$$

where θ_{obs} is the observation angle relative to the average electron direction [9, 10, 34, 38, 41]. In convenient units, the energy of the nth harmonic is given by [9, 10, 34, 38, 41]:

$$E_n(keV) = 0.950\frac{nE^2(GeV)}{\lambda_p(cm)\left(1+\frac{K^2}{2}\right)} \tag{1.13}$$

The harmonics have too small an energy distribution for a typical XAS experiment, and the energy at which they appear must be changed. In order to achieve these shifts, the gap between the upper and lower magnet arrays is changed, resulting in either an increased (smaller gap) or decreased (larger gap) magnetic field strength. (Increasing B_o increases K, see Equation 1.11.)

1.1.3 The Beamline - A Typical Hard X-ray Set-up

Once synchrotron light has been produced, it is then collected, monochromated, and used in experiments. The equipment that is used for this purpose is generally referred to as a beamline. In general, a beamline consists of three parts: a front-end, an optics section, and an endstation. However, what occupies these parts of the beamline varies vastly from one set-up to the next, and, as such, it is difficult to describe a typical set-up. For instance, the optics used to produce monochromatic light will vary vastly depending on what energy of light is to be used. Given this, this introduction will only focus on a typical beamline set-up which may be used for hard X-ray EXAFS and XANES experiments. (Here, hard X-rays are defined as those with energies greater than 2 keV.)

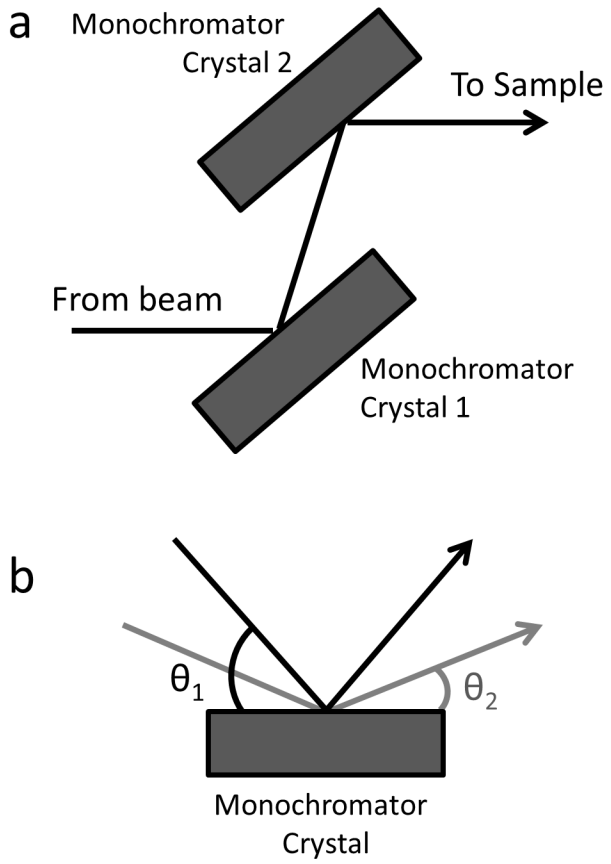

Figure 1.3: (a) A cartoon schematic of a double crystal X-ray monochromator is shown. The addition of a second crystal allows for the selection of different energies with minimal change in the beam position. (b) Bragg reflection off of a single crystal. The wavelength (energy) of the light reflected will depend on θ.

1.1.3.1 X-ray optics: The Double Crystal Monochromator

For an XAS beamline, the purpose of the X-ray optics is produce highly monochromatic, tunable X-rays in a shape and spot size appropriate to the sample. In this regard, the most important optical component (and perhaps the most important component in the entire beamline) is the double crystal monochromator [42]. This device consists of two single crystals mounted parallel to each other (Figure 1.3a) and uses Bragg diffraction to separate individual wavelengths of light.

Bragg diffraction is described by Bragg's law, which states:

$$n\lambda = 2d\sin\theta,\ n = 1,2,3... \tag{1.14}$$

where λ is the wavelength of the diffracted light, d is the lattice plane spacing, and θ is the angle of diffraction [12, 42]. The wavelength is inversely proportional to the energy of the photons, and by changing the angle between the crystal face and the incident beam, photons having a given energy can be selectively collected. As illustrated in Figure 1.3b, only one crystal is required to attain the energy separation, but the position of the beam spot would be energy dependent. To alleviate this problem, a second crystal is added (mounted parallel to the first crystal) and is connected to the same tracking motor as the first crystal. This ensures that the beam spot remains relatively constant across the entirety of a scan [42].

XAS beamlines typically use Si single crystals for the monochromator, owing in part to their favourable thermal properties and relatively low prices (due to the manufacturing advances made by the semi-conductor industry) [42]. Diamond crystals may also be used, but these are less common due to their high price [42]. In general, the material and crystal face must be chosen so that the crystal provides both high flux and high resolution. However, these two parameters are often mutually exclusive, and the beamline is designed to achieve a balance between both factors. For XAS beamlines, using either the Si(111) or Si(220) faces is common. Here, the former optimizes flux at the sacrifice of resolution, while the later increases resolution at the cost of flux [9,43,44]. It is also important to orient the crystal face, as crystal glitches may occur which dramatically reduce the flux at a given energy. Crystal glitches occur when the desired wavelength to be collected also satisfies the Bragg equation for another crystallographic plane in the crystal (but at a different θ value) [45]. This decreases the number of photons that may be used for the experiment.

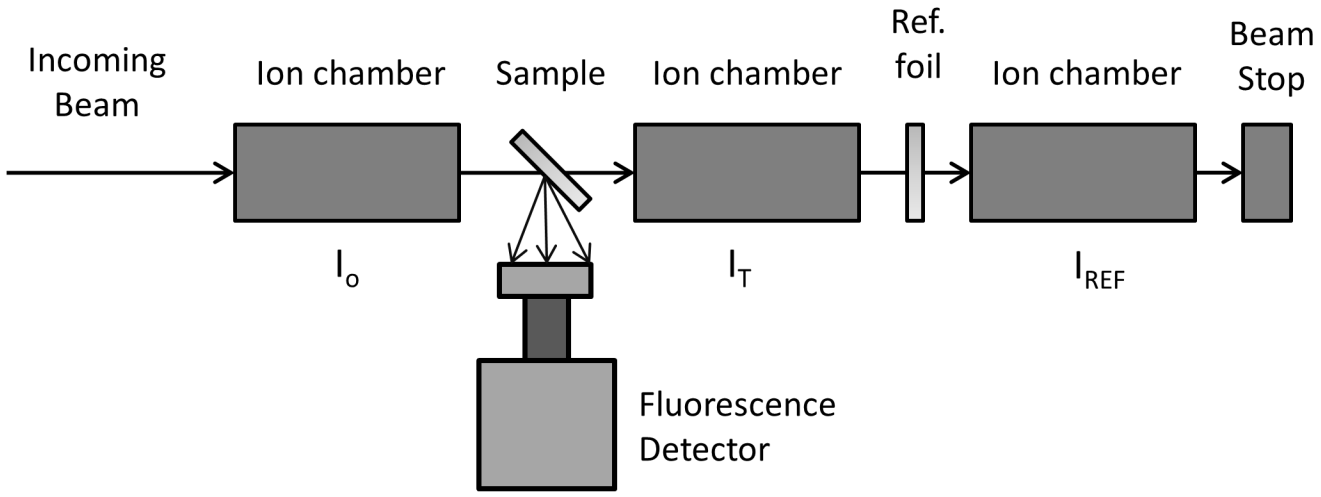

Figure 1.4: A schematic of a typical set-up for a hard X-ray XAS experiment. The photon beam first enters through the I_o ion chamber and is then transmitted through the sample and the transmitted beam is measured with the I_T ion chamber. Fluorescence can be collected simultaneously and a transmission spectrum from a known standard may also be measured concurrently with the sample spectrum to facilitate accurate energy calibration.

1.1.3.2 An Endstation Designed for XAS Experiments

Once monochromatic X-rays have been collected and shaped, they can be used for XAS experiments. These experiments are performed in the endstation section of the beamline. While the front-end and optics of a beamline can vary in minor ways, it is in the endstation where beamlines are truly differentiated, and where the experiment-specific set-ups are most commonly found. This is also the region of the beamline that the user will interact with the most. Generally, for hard-X-ray beamlines, the endstation equipment is designed to be modular, allowing for the endstation to be easily adapted for a variety of experiments. However, in some cases, such as for vacuum ultra-violet (VUV) and soft X-ray beamlines, the low-energy light requires a high-vacuum environment, and the endstation set-ups are less flexible. Given the wide variety of endstation set-ups possible (even for one beamline), only a typical setup used for hard X-ray XANES and EXAFS experiments will be described here.

A schematic of a typical hard X-ray XAS beamline experiment is illustrated in Figure 1.4, where both transmission and fluorescence signals are collected. The sample is generally mounted

at a 45° angle to the incident beam and placed between two ionization chambers, I_o and I_T. Usually, the sample is mounted in air, though various sample stages, including in-situ cells and cryostat systems sealed with X-ray transparent Be windows, may be used. An in-line measurement of a calibration spectrum can be collected by placing a reference sample (usually a metal foil) between the I_T and I_{REF} ion chambers (Figure 1.4) [3]. The ionization chambers measure the intensity of the X-ray beam, and allow for the measurement of transmission data. Ionization chambers consist of a tube that is sealed on both ends with an X-ray transparent material. Gas(es) is (are) flowed through the tube, and a potential is applied perpendicular to the gas flow. As the X-rays pass through the chamber, a small portion of the X-rays ionize some of the gas molecules, resulting in a current that is proportional to the intensity of the X-ray beam. (The current is converted into a voltage, which is the value that is measured.) The gases that are used in the ion chamber are varied based on what X-ray energies are being selected. Generally, He, N_2, or Ar (or some mix of the three) is used [9]. For low-energy beams, He or a He/N_2 mix is typically used, as it has a relatively low X-ray cross-section, so only a small number of the incident X-rays are absorbed [9]. For high X-ray energies, however, He is too poor an X-ray absorber, so too little signal will be registered, and a heavier gas with a larger absorption cross-section, such as Ar must be used. N_2 is generally used for medium-energy X-rays (i.e. $\sim$5 keV-10 keV).

Transmission measurements use the Beer-Lambert law to measure the absorption cross-section of a material. In this case, the Beer-Lambert law may be expressed as:

$$I_T = I_o e^{\mu(E)x} \tag{1.15}$$

where I_T is the transmitted beam intensity, I_o is the initial beam intensity, x is the sample thickness, and $\mu(E)$ is the absorption coefficient of the sample, which is a function of the photon energy and is related to the transition probability, P (see Equation equation (1.6)) [3, 8]. Because $\mu(E)$ is the sum of the absorption coefficients of all the components in a material (i.e., $\mu(E) = \sum_i \mu_i(E)$, where $\mu_i(E)$ is the absorption coefficient of the i^{th} component of the mixture), the sample must

be sufficiently concentrated for a change in $\mu(E)$ to be observed [3]. The Beer-Lambert law is only valid when transmission through the sample is uniform. Thus, when using the Kapton tape preparation method (see Section 2.2.2 on page 38), care must also be taken during sample preparation to prevent pinhole effects. These effects occur when the sample contains small regions that are either thicker or thinner than the average thickness of the powder layer, resulting in non-uniform transmission [3]. Pinhole effects can be minimized be ensuring that the sample is finely ground, and by using multiple sample tape layers.

It is better to collect fluorescence data when a sample is dilute and it is not possible to collect transmission data [3]. There are several types of fluorescence detectors currently available, and these are broken up into two categories: energy dispersive and non-energy dispersive. For hard X-ray experiments, it is advantageous to use an energy dispersive detector as the fluorescence emission lines are typically well-separated compared to low-energy fluorescence lines, allowing for the selective collection of the emission line relevant to the absorption edge being studied. While several energy dispersive fluorescence detectors are available, the most common is a multi-element Ge detector [46]. In this set-up, each detector element is essentially a mini-detector, and the signal from each element can be averaged to give a high quality spectrum.

When measuring XAS spectra via fluorescence, it is important that the sample is dilute *and* either very thin or infinitely thick (relative to the penetration depth of the X-rays). The reasons for this become evident upon consideration of the relationship between $\mu_i(E)$ and the ratio of I_F/I_o, expressed as:

$$\frac{I_F}{I_o} = A\frac{\mu_i(E)}{\mu(E)+\mu(E_F)}\left(1-e^{-x(\mu(E)+\mu(E_F))}\right) \tag{1.16}$$

where E_F is the fluorescence emission energy, A is a constant, x is the sample thickness, $\mu_i(E)$ is the absorption coefficient of the atom of interest, $\mu(E)$ is the total absorption coefficient, and $\mu(E_F)$ is absorption coefficient of the atom of interest at the fluorescence emission energy [3, 46, 47]. When x is very large (relative to the X-ray penetration depth), the exponential term approaches 0. Further, if the sample is dilute, $\mu_i(E) \ll \mu(E)$ and the term $\mu(E)+\mu(E_F)$ will be approximately independent of $\mu_i(E)$. Therefore, Equation 1.16 may be simplified, and $I_F/I_o \propto \mu_i(E)$. If the sample

is very thin, then x will be small and the exponential term may be approximated as:

$$e^{-x(\mu(E)+\mu_i(E_F))} \approx 1 - x(\mu(E) + \mu_i(E_F)) \tag{1.17}$$

and again, assuming the sample is dilute, $I_F/I_o \propto \mu_i(E)$. If the sample is not dilute, then $\mu(E)$ cannot be approximated as constant, and self-absorption effects will occur. (Self-absorption effects may occur even when the sample is very thin or very thick.) When self-absorption effects occur, the fluorescence photons are re-absorbed by the sample, resulting in the loss of the linear relationship between I_F/I_o and $\mu_i(E)$. Hence, it is important to choose a detection technique that is appropriate to the sample to be studied.

1.2 $Sr_2Fe_{2-x}Mo_xO_6$ Double Perovskites

Now that the theory and practice of XAS has been discussed, focus will now shift to exploring the properties of the systems studied by XANES in this thesis. Transition-metal oxides adopting the perovskite-type structure have been found to have many useful chemical and physical properties, and have been the subject of a wide variety of investigations over the past 60 years [48–51]. Oxide-based perovskites have a general formula of ABO_3, where A is a large cation (usually an alkaline earth metal) and B is a small cation (usually a transition metal) [48–51]. (Halide-containing perovskites are also known, but are less common.) In these materials, the B cations form a network of corner-sharing BO_6 octahedra and the A cations occupy the 12-coordinate interstitial voids between the octahedra, and the unit cell is normally cubic ($Pm\bar{3}m$) [48, 52–55]. A common variation of the perovskite-type structure is the double perovskite, which has the general formula $A_2BB'O_6$ (or $AA'B_2O_6$), where B and B' are two different cations. At present, over 300 different materials exhibiting the double perovskite structure have been discovered, and many of these were originally discovered between the early-1950s and mid-1970s [52, 56]. In the 1980s, research on the double perovskites was further aided by neutron-scattering experiments, which were better able to characterize the structures of the double-perovskites [56]. (Though based on the cubic perovskite

structure, double perovskites often exhibit distortions from cubic symmetry, and identifying the correct space group is often a challenge; *vide infra*.) However, while the double perovskites have been of interest to solid-state chemists for nearly 6 decades now, it was not until relatively recently (within the past 20 years) that these materials began to be heavily investigated for their interesting physical and chemical properties. One example of this is the Sr_2FeMoO_6 double perovskite, which is one of the subjects of study in this thesis. Though first discovered as early as 1963, intensive research of this system began only after Kobayashi's seminal 1998 Nature paper regarding the presence of colossal magnetoresistance (CMR) in Sr_2FeMoO_6 [52, 57]. (Sr_2FeMoO_6 is known to be oxygen deficient and is technically better expressed as $Sr_2FeMoO_{6-\delta}$, but for the sake of convenience it will be referred to as Sr_2FeMoO_6 [58–61].)

While Sr_2FeMoO_6 has been well studied, the exact structures of the $Sr_2Fe_{2-x}Mo_xO_6$ compounds are still poorly understood. When the Mo content is low ($x \leq 0.50$), the system is highly disordered and the powder XRD and neutron powder diffraction patterns from these materials are best fitted by a cubic, $Fm\bar{3}m$ structure (Figure 1.5) [52, 53, 62, 63]. When the Mo content is increased past x = 0.50, the system undergoes a tetragonal distortion, and the powder diffraction patterns from these materials are best fitted using either the $I4/m$ or $I4/mmm$ space group (see Section 2.1 on page 34 for a full discussion) [52,53,62]. The transition from a cubic $Fm\bar{3}m$ structure to the tetragonal $I4/m$ structure is caused by opposite rotations of the FeO_6 and MoO_6 octahedra and results in the formation of two distinct octahedral sites: a larger Fe site and a smaller Mo site [53]. While this transition is known, no satisfactory explanation of the mechanism of distortion has been proposed, and this issue has been studied using XANES in this thesis.

Determination of the structures of $Sr_2Fe_{2-x}Mo_xO_6$ is further confounded by possible changes in the Fe and Mo cation ordering. In $A_2BB'O_6$ double perovskites (such as the Sr_2FeMoO_6 double perovskite), the B and B' cations have been found to adopt three forms of ordering: 1) random occupation of the octahedral sites (i.e. no ordering); 2) a rock salt structure; or 3) layering of sheets of BO_6 and $B'O_6$ octahedra [56]. Which form of ordering is present largely depends on the differences between the oxidation state and size of the B and B' cations [56, 65]. The rock salt

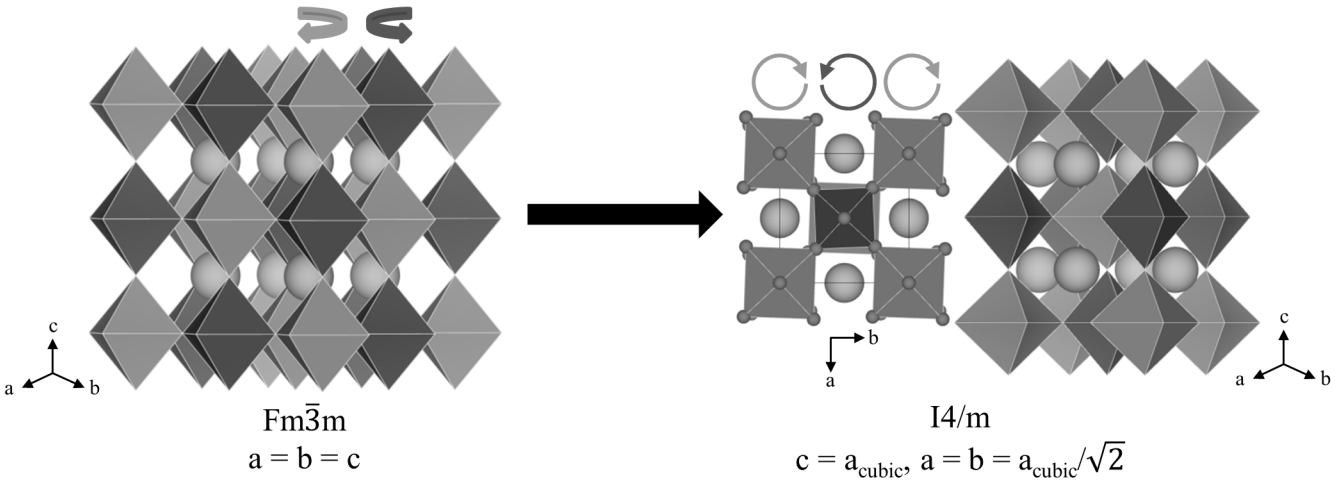

Figure 1.5: The $Sr_2Fe_{2-x}Mo_xO_6$ compounds adopt one of two crystal structures. At low values of x, the undistorted, ordered double perovskite structure is adopted (space group $Fm\bar{3}m$, left,), consisting of alternating Fe (grey) and Mo (dark grey) octahedra with Sr atoms (light grey) occupying the interstitial sites [64]. (The structure shown here represents a perfect Sr_2FeMoO_6 double perovskite.) As the value of x is increased, the Fe and Mo octahedra rotate (indicated by the circular arrows), resulting in FeO_6 octahedra that are stretched and MoO_6 octahedra that are compressed, and this results in a transition to a tetragonal unit cell (space group $I4/m$, right). The view along the c-axis (centre right), shows the rotation of the octahedra (O atoms are shown as grey spheres). The relationship between the lattice constants from the two space groups is shown below each structure.

structure will be adapted if the difference between the oxidation states of the B and B' cations is greater than 2 [56]. When the difference between the oxidation states of the B and B' cations is equal to 2, rock salt ordering of the cations is usually observed, though if the difference between the ionic radii of the B and B' cations is less than $\sim$0.2 Å then a random distribution of the B and B' cations in the octahedral sites may be observed (leading to a mixed-occupancy single-perovskite structure) [55, 56, 65, 66]. In the case of Sr_2FeMoO_6, the B and B' cations are ordered following the rock-salt ordering motif (Figure 1.5). In general, the layered double perovskite structure is relatively rare in $A_2BB'O_6$-type systems, with the Ln_2CuMO_6 (Ln = lanthanide, M = Ge, Mn, Ti, Ir, Sn, Zr, Pb) family comprising the majority of such examples [56, 67–69].

Though a system may have an overall ordering of the B and B' cations, it is still possible for local disorder to occur in the form of anti-site disorder (i.e., a B cation occupies a B' site, and vice versa). In Sr_2FeMoO_6, anti-site disorder significantly affects the magnetic properties of these materials (*vide infra*), and determining the nature of these anti-site defects has become a focus of recent research [70–76]. While composition will affect the propensity for anti-site disorder in a system, the amount of disorder in a given composition is also strongly affected by a number of other variables, such as synthetic method and annealing temperature [70–76]. As such, the physical properties of a given sample of Sr_2FeMoO_6 are highly dependent on the conditions of its synthesis, which tends to hinder the comparison of results published by different research groups. This provides further impetus to develop an understanding of anti-site disorder in these systems. To this end, a great number of strides have been made. It has been reported that at high temperatures ($>$1200 °C), a more disordered phase is favored, while at low temperatures, a highly ordered phase is favorable though unattainable due to the kinetic limitations of the reaction [63, 77, 78]. This work has helped to explain the link between synthetic conditions and anti-site disorder. Further, using EXAFS, X-ray diffraction (XRD), and electron diffraction techniques, the nature of the disorder present in these materials has been more fully understood [61, 65, 72]. These studies found that a single grain of material consists of many ordered domains, and the anti-site disorder is concentrated at the boundaries between these domains. However, despite these great increases in our knowledge

of the Sr_2FeMoO_6 system over the past several years, many other variables that may affect the properties of this material remain poorly understood. One example of such knowledge deficiency is the effect of composition on the formation mechanics of these materials. While Sr_2FeMoO_6 is usually regarded as a stoichiometric compound, it is actually a single composition in of the $Sr_2Fe_{2-x}Mo_xO_6$ solid solution [59]. Because of this, an understanding of how these materials are affected by deviations from the Sr_2FeMoO_6 composition would be highly beneficial. As such, a series of $Sr_2Fe_{2-x}Mo_xO_6$ ($0.25 \leq x \leq 1.0$) were studied via XANES in this thesis.

The Sr_2FeMoO_6 double perovskite has been investigated for use in a number of different applications. For instance, these materials have been investigated for use as anodes in solid-oxide fuel cells due to their oxygen deficient nature and the presence of both Fe^{2+}/Fe^{3+} and Mo^{5+}/Mo^{6+} redox couples [79]. However, while Sr_2FeMoO_6 may find use in a variety of applications, its magnetic properties have drawn the most attention in the literature. Sr_2FeMoO_6 is ferrimagnetic, having a Curie temperature between 410 K and 450 K [62]. The magnetic behavior of Sr_2FeMoO_6 has been best described assuming that only Fe^{3+} and Mo^{5+} are present in these materials; the Fe^{3+} cations form a ferromagnetic sub-lattice with S = 5/2, while the Mo^{5+} cations form an oppositely aligned ferromagnetic sub-lattice with S = 1/2 [52, 57, 76, 80, 81]. (Here S refers to the spin of the total electron spin of each magnetic centre.) The magnetic interactions in Sr_2FeMoO_6 arise from a Fe–O–Mo–O–Fe double-exchange mechanism, and, as such, are highly dependent on the ordering of the Fe and Mo cations. The double exchange mechanism also leads to the half-metallic nature of the Sr_2FeMoO_6 materials [52, 57, 82]. In this case, the Mo^{5+} 4d electrons occupy a conduction band when their spins oppose the Fe^{3+} 3d-electrons (i.e., the conduction band is spin-polarized) .

As a consequence of being both a half-metal and a ferrimagnet, Sr_2FeMoO_6 has been shown to exhibit magnetoresistance, which means that the resistance of the material changes upon the application of a magnetic field. Sr_2FeMoO_6 has been shown to exhibit both colossal magnetoresistance (CMR) and tunneling magnetoresistance (TMR) [57, 73, 83]. In colossal magnetoresistance, large changes in the resistivity of a material (orders of magnitude) are observed upon the application of a strong magnetic field (on the order of Tesla) whereas TMR is characterized by relatively

small changes in resistance upon the application of a weak magnetic field. TMR is analogous to giant magnetoresistance (GMR), and materials exhibiting TMR may be used in spin-valves (which are commonly used in memory storage applications) [84–86]. Interestingly, TMR is generally only found in layered thin-film materials, in which an insulating layer can be specifically engineered [84, 86]. However, compressed pellets of Sr_2FeMoO_6 have been shown to exhibit TMR without the insertion of an insulating layer, and this behavior has been proposed to arise from compositional variation within individual grains [61]. The presence of self-contained TMR is novel, making Sr_2FeMoO_6 an attractive material for use in a variety of spintronic applications. However, most of the theory describing the magnetic properties of Sr_2FeMoO_6 relies on the oxidation state assignments of Fe^{3+} and Mo^{5+}. There has been much debate in the literature regarding the oxidation states of Fe and Mo in Sr_2FeMoO_6, with assignments ranging between Fe^{2+} to Fe^{3+} and Mo^{5+} to Mo^{6+} [74, 75, 87–91]. In order to form a theory that accurately describes the properties of the Sr_2FeMoO_6 double perovskite, it is necessary to better understand understand how the oxidation states of Fe and Mo may change with composition. To this end, XANES has been used in this thesis to determine trends in the changes in the oxidation states of Fe and Mo across a series of $Sr_2Fe_{2-x}Mo_xO_6$ double perovskites.

1.3 $Cu_2FeSn_{3-x}Ti_xS_8$ Thiospinels

The transition-metal chalcogenides are a well-studied group of materials, which are known to exhibit a wide variety of interesting and novel properties. These materials are often structurally similar to transition-metal oxides with chalcogens (i.e. S, Se, and Te) replacing O as the primary anion. Because chalcogens have lower electronegativity values than O, transition-metal chalcogenides often contain bonds with a greater degree of covalency than their O-containing analogues, leading to complicated electronic structures [92, 93]. Transition-metal sulfides are of particular importance, which in addition to having interesting physical and chemical properties, constitute the majority of minerals which are exploited for harvesting non-Fe metals [92, 94–96]. For this,

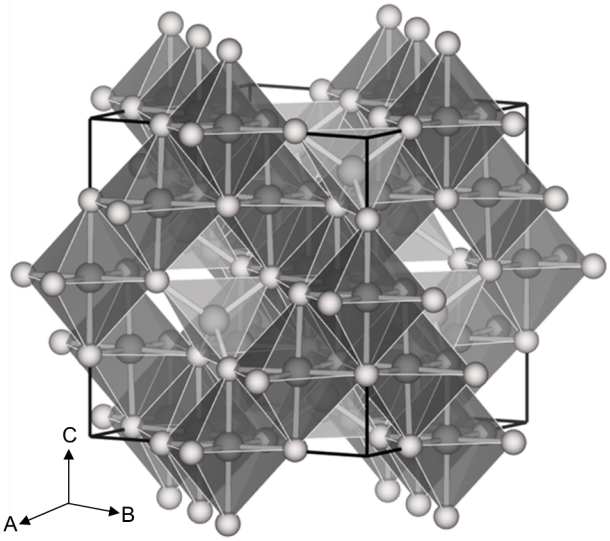

Figure 1.6: $Cu_2FeSn_{3-x}Ti_xS_8$ thiospinels may adopt a cubic ($Fd\bar{3}m$) structure [64]. The S ions (light spheres) are cubic close-packed, forming three non-equivalent tetrahedral voids and two non-equivalent octahedral voids. Fe, Sn, and Ti are randomly distributed in one of the unique octahedral sites (shown in dark grey) while Cu occupies only one of the two non-equivalent tetrahedral sites (shown in grey).

and other reasons, the chemistry of the transition-metal sulfides has been of particular interest to the geochemical community [92–96].

One particular group of transition-metal sulfides that have been well-studied are the thiospinels, which have been well studied and found to exhibit a wide variety of physical properties [97–103]. For example, the $Cu_{1-x}Fe_xCr_2S_4$ thiospinels have been shown to exhibit colossal magnetoresistance, while $CuRh_2S_4$ is known to be a superconductor [102, 104]. Of particular importance to this thesis are the $Cu_2FeSn_{3-x}Ti_xS_8$ thiospinels, which are usually studied for their use as cathodes in lithium-ion batteries. Thiospinels adopt a structure analogous to the cubic spinel-structure (space group $Fd\bar{3}m$), and have the general formula AB_2S_4, where A and B are transition metals [105,106]. In a normal spinel, the A cation has a lower oxidation state and occupies a tetrahedral site while the B cation has a higher oxidation number and occupies an octahedral site. (The inverse spinel structure occurs when the cation with the higher oxidation state occupies the tetrahedral site [105,106].) As with oxide-based spinels, the A and B sites can accommodate a large number of cations, allowing for the optimization of the properties of a given thiospinel. The structure of $Cu_2FeSn_3S_8$ is shown in Figure 1.6, and is illustrative of the spinel structure [107]. (Though single crystal studies

have shown $Cu_2FeSn_3S_8$ to have a tetragonal unit cell, the distortion from the cubic structure is slight, and these materials can generally be thought of as being cubic [99, 107–110].) In this structure, the S-atoms are approximately cubic close-packed, with Cu atoms occupying one of three distinct tetrahedral sites (the other two are empty) and the M atoms (M = Fe, Ti, Sn) randomly distributed in one of two unique octahedral sites (the other is empty) [98, 106, 110–112]. The large number of unoccupied sites allow for the intercalation of various small ions, and is one of the reasons why these materials are desirable for use in electrochemical applications [97, 100, 108, 110].

In the $Cu_2FeSn_{3-x}Ti_xS_8$ compounds, as Ti is substituted for Sn, the edge length of the unit cell contracts from $\sim$10.33 Å to $\sim$10.00 Å, resulting in a decrease in both the M–S and Cu–S bond lengths [98, 107, 108, 110]. Here, Fe adopts a 2+ oxidation state (d^6), while Cu a 1+ oxidation state (d^{10}), and Sn and Ti both adopt a 4+ oxidation state (d^{10} and d^0, respectively) [98, 99, 110]. Interestingly, while Cu^{+1}, Sn^{4+}, and Ti^{4+} all contain either empty or full d-orbitals, the Fe^{2+} ions have only partially-filled d-orbitals, which may adopt either a low-spin (LS; i.e., $t_{2g}{}^6e_g{}^{*0}$) or high-spin (HS; i.e., $t_{2g}{}^4e_g{}^{*2}$) electron configuration. Recently, the $Cu_2FeSn_{3-x}Ti_xS_8$ compounds have been shown to exhibit interesting magnetic behaviour, undergoing what is known as a spin-crossover transition [98].

The spin-crossover (SCO) transition is a phenomenon in which a transition-metal undergoes a transition from a LS state to a HS state, or vice versa [113–115]. When the crystal field-splitting is much greater than the electron-electron repulsion energy, the LS state is favoured. However, when the crystal field-splitting is small compared to the electron-electron repulsion energy, the system energy is minimized when the HS state is adopted [116]. A more interesting scenario arises when the crystal field-splitting energy and electron-electron repulsion energy are nearly equal, and the interplay between the two values leads to the observation of SCO transitions. Because the crystal-field splitting must be on the order of the electron-electron repulsion energy, the SCO transition is usually only observed when the metal centre is in an octahedral coordination environment [115–117]. However, a pressure-dependent SCO transition has been recently reported in $SrFeO_2$, where Fe occupies a square planar coordination environment [118]. Interestingly, the SCO transition is

often accompanied by a small changes in structure, making the relationship between the repulsion energy and crystal-field splitting energy dynamic [116].

An SCO transition may be induced by a number of different perturbations which change the energy of a system. These include irradiation with UV light, changes in pressure, changes in atmosphere, and changes in temperature [118–122]. Due to possible changes in structure, the spin-transition, in addition to changing the magnetic properties of a material, may also result in significant changes in the physical properties of the material as well. Because these systems react in a measurable and known manner, they have been explored for use in a number of applications including use as sensors, molecular switches, displays, and memory storage devices [123, 124]. While materials exhibiting the SCO have been known since the 1930s, study of the SCO transition has undergone a type of renaissance, with research focusing on optimizing how the SCO transition is exhibited so that it may be exploited for use in the previously mentioned applications [115, 117, 125].

An important parameter that characterizes an SCO material is the spin-transition temperature, defined as the point where the number of metal centres in a HS state equals the number of centres in a low LS state. An SCO material may be further characterized by the transition behaviour around the transition-temperature. For example, a gradual and reversible transition may be observed around the transition-temperature, as is the case for the $Cu_2FeSn_{3-x}Ti_xS_8$ thiospinels. Often, the transition may exhibit hysteresis, and the LS $\rightarrow$ HS transition temperature is different from the HS $\rightarrow$ LS transition temperature. Such behaviour is often desirable, as this behaviour can be used in a number of applications [115, 121, 124]. For example, polymers similar to $[Fe(NH_2trz)_3](tosylate)_2$ (trz = $C_2H_3N_3$, tosylate = $CH_3C_6H_4SO_3^-$) have been engineered to have a LS $\rightarrow$ HS transition temperature below room temperature and a HS $\rightarrow$ LS transition temperature above room temperature [124]. The materials change colour depending on spin-state, and a display may be fabricated by applying the materials to an array of Peltier heating elements. The individual Peltier elements then become pixels that can be operated using relatively small amounts of energy [124].

While the SCO transition has been well-studied in molecular systems where only a small num-

ber of metal centers may interact due to the separation caused by the steric bulk of the coordinating ligands, relatively little research has been performed on systems where the separation between the metal centers is small and the system contains a repeating, periodic structure. (Studies of $LaCoO_3$-based systems are a notable exception to this statement [126–128].) In ordered, crystalline systems, long-range magnetic interactions (e.g. ferromagnetism) are possible, and may affect the energy difference between the low-spin (LS) and high-spin (HS) states, ΔE_{HL} [98, 115, 129, 130]. For crystalline materials, generally $\Delta E_{HL} \gg kT$ (k is the Boltzmann constant and T is temperature), and the SCO transition is difficult to study under easily accessible laboratory conditions [98]. However, the spin transition may be readily manipulated at relatively moderate temperatures and pressures for some materials (e.g., $LaCoO_3$) where $\Delta E_{HL} \sim kT$ [98, 126–128].

It has been recently reported that the $Cu_2FeSn_{3-x}Ti_xS_8$ thiospinels exhibit an SCO transition where $\Delta E_{HL} \sim kT$, and the transition temperature has been reported to be $\sim$215 K in these materials. In this previous study, it was found that the amount of HS Fe^{2+} present at room temperature initially decreased as the Ti content was increased from x = 0 to x = 1.5 [98]. Interestingly, as the Ti content was further increased from x = 1.5 to x = 3.0, the amount of HS Fe^{2+} increased [98]. The increase in HS Fe^{2+} between x = 1.5 and x = 3.0 was thought to arise from magnetic interactions between neighboring HS Fe^{2+} ions [98]. In the $Cu_2FeSn_{3-x}Ti_xS_8$ thiospinels, interactions between next-nearest-neighbor Fe^{2+} ions (via S) can result in weak antiferromagnetic interactions that increase in strength with increasing Ti content. This leads to antiferromagnetic ordering with Néel temperatures of $\sim$2-7 K when the Ti content is greater than x = 1.5 [98]. These antiferromagnetic interactions appear to stabilize the HS state, reducing the amount of thermal energy necessary to induce a LS to HS SCO transition, resulting in the increased concentration of HS Fe^{2+} in $Cu_2FeTi_3S_8$ versus $Cu_2FeSn_3S_8$ [98].

The $Cu_2FeSn_{3-x}Ti_xS_8$ thiospinels present an opportunity to study the SCO transition in crystalline materials using XANES. Because the pre-edge excitations involve the excitation of transition-metal 1s electrons to (n-1)d states, it is expected that these features will change as the spin-state of the transition metal varies. In addition to changes in the pre edge, changes in the main-

edge features may also be observed. These features arise from 1s $\rightarrow$ np transitions and may be affected by changes in structure, oxidation state, and covalency [2, 28, 131]. The main-edge is also sensitive to changes in spin-state, as SCO transitions are usually accompanied by small changes in structure [4, 115, 124, 125, 132–134]. To this end, Chapter 3 discusses if and how the spin-crossover phenomenon may be investigated using K-edge XANES through a study of the $Cu_2FeSn_{3-x}Ti_xS_8$ thiospinels. Further, because thiospinels are more covalent than oxide-based spinels, this investigation also allowed for a study of how changes in the covalency of the metal-ligand bonds affected the intensities of the features found in the pre-edge regions of the metal K-edge spectra.

1.4 Rare-earth Orthoferrites

The rare-earth orthoferrites, which adopt a distorted perovskite structure, have the general formula of $REFeO_3$ (RE = rare-earth, Y). These oxides are an interesting set of compounds that have been investigated for use in a variety of applications. Some of these applications include use in solid-oxide fuel cells, gas sensors, photo-catalysis, and vehicle catalytic converters [135–141]. In addition, the rare-earth orthoferrites have also been found to exhibit antiferromagnetism, with Néel temperatures ranging from 623 K (RE = Lu) to 740 K (RE = La), making them potentially useful for data storage applications [142, 143]. In addition to rare-earth orthoferrites, analogous systems with transition metals other than Fe are also known, such as the rare-earth orthogallates ($REGaO_3$) and rare-earth orthoscandanates ($REScO_3$) [144, 145]. Because of the large number of ions that may be substituted into these materials, the physical and chemical properties of these materials can be optimized for use in a given application [48]. However, because of the large number of ways these systems can be manipulated, it is necessary to gain a better understanding of how the electronic structure of these materials varies as the RE atom is varied in order to facilitate a rational design framework for optimization of these compounds. XANES has been performed to investigate how the electronic structure and bonding environment in these materials change as the identity of the RE is varied.

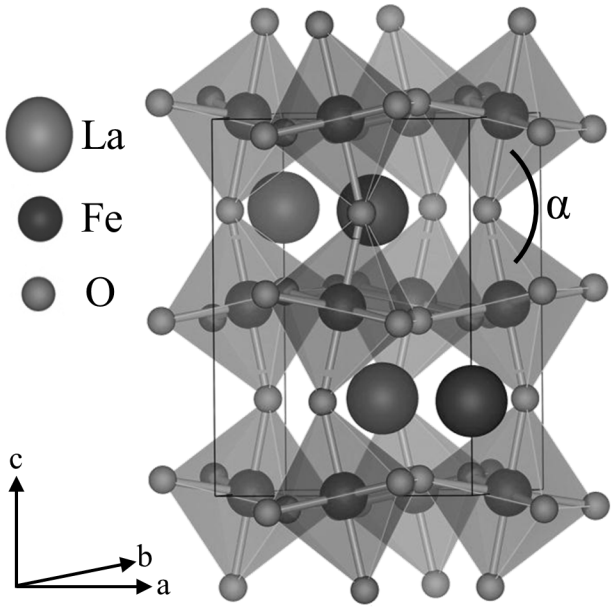

Figure 1.7: The unit cell of $LaFeO_3$ (space group Pnma) is shown. The angle between layers of FeO_6 octahedra is defined to be the octahedral tilt angle, α. The Fe–O bond lengths are 2.00 Å and the eight R–O bond lengths range from 2.41 Å to 2.80 Å [64].

The rare-earth orthoferrite unit cell is described by the Pnma space group [146–152]. Here, the RE^{3+} ion occupies the interstitial sites between layers of corner-sharing FeO_6 octahedra (Figure 1.7). The octahedra are tilted, resulting in the distortion from the regular perovskite structure. As the ionic radius of the rare-earth atom decreases, the tilt angle between the octahedra along the c-axis (α) decreases [146–153]. The antiferromagnetic ordering of these oxides has been related to the size of the tilt angle, with larger values of α leading to higher Néel temperatures [142,154,155]. While the A ion occupies a typically 12-coordinate site in a normal perovskite, the RE is shifted from the centre of the interstitial space in the rare-earth orthoferrites, resulting in the formation of two RE–O coordination shells [143, 144, 146].

Because this structure contains Fe–O–Fe angles between 90° and 180°, an intersite hybrid feature (See Section 1.1.1.2 on page 4) is found in the pre-edge. As the tilt angle of the FeO_6 octahedra in the rare-earth orthoferrites varies in a regular fashion with changes in the identity of the RE, this system provides an excellent opportunity to study the angular dependence of the intersite hybrid intensity in a controlled manner. To this end, the influence of a change in tilt angle between NNN Fe atoms on the intensity of the intersite hybrid peak intensity observed in the Fe

K-edge spectra from $REFeO_3$ has been studied in this thesis.

1.5 Synopsis

Due to the richness of information contained in the pre-edge, it is necessary to understand how different variables may affect the pre-edge features. Such comprehension of the various factors that affect the pre-edge may be achieved through systematic and focused studies of materials with known properties. This allows for the correlation of the changes in the pre-edge to changes in the material properties, allowing for insight into the mechanisms causing the changes in the pre-edge. These lessons may then be applied to the analyses of spectra from materials with relatively unknown properties. The studies presented in this thesis were designed to provide such knowledge.

In Chapter 2, the effect of changes in both the oxidation state and coordination number on the pre-edge are explored through a study of the $Sr_2Fe_{2-x}Mo_xO_6$ double perovskites. While the effects of changes in coordination number and changes in oxidation state on the pre-edge are well known, it is difficult to analyze the changes in the pre-edge when these effects are present simultaneously. In the $Sr_2Fe_{2-x}Mo_xO_6$ compounds, both the coordination number and oxidation state of Fe and Mo change. By evaluating the XANES spectra from these materials, the effects of changes in coordination and changes in oxidation state were separated. Here, it was found that when $x > 0.50$, the oxidation state of both Fe and Mo decreased while the oxygen deficiency of the system increased.

The effect of changes in the covalency of the metal-ligand bond is investigated in Chapter 3 through a study of a series of $Cu_2FeSn_{3-x}Ti_xS_8$ thiospinels. These materials also exhibit an SCO transition, and the effect of the SCO transition on the pre-edge was studied by collecting temperature-dependent Fe K-edge XANES spectra. These spectra showed that the intensity of the pre-edge is highly dependent on the covalency of the Fe–S bond, with increased covalency leading to an increased intensity of the pre-edge features. Interestingly, no change in the pre-edge was observed with changes in the spin-state of the Fe centres, and the reason for this is described in

Chapter 3.

Finally, Chapter 4 will present a study devoted to understanding the relationship between the bond angle and intensity of an ill-studied pre-edge feature known as an intersite hybrid peak. A XANES study of a series of $REFeO_3$ rare-earth orthoferrites is presented in this chapter. In $REFeO_3$, the Fe–O–Fe bond angle is known to vary linearly with the size of the RE atom, providing a well-understood environment where only changes in the bond angle may affect the intensity of the intersite hybrid peak. Here, experimental evidence was provided which showed, conclusively, that the intensity of the intersite hybrid decreases as the Fe–O–Fe bond angle decreases.

Through these studies, this thesis increases the general understanding of the features in the pre-edge and the variables that affect them. These findings will be useful to a wide variety of fields, ranging from geochemistry to chemistry to fundamental physics.

Chapter 2

AN INVESTIGATION OF THE Fe AND Mo OXIDATION STATES IN $Sr_2Fe_{2-x}Mo_xO_6$ ($0.25 \leq x \leq 1.0$) DOUBLE PEROVSKITES BY X-RAY ABSORPTION SPECTROSCOPY[1]

2.1 Introduction

Double perovskite compounds, having the general formula $A_2BB'O_6$ (A = Alkaline-earth, B/B' = transition metal), are well known to exhibit a variety of interesting and technologically relevant properties [156–159]. The basic double perovskite structure is an extension of the cubic perovskite structure (ABO_3) in which corner-sharing BO_6 and $B'O_6$ octahedra alternate, resulting in long-range ordering (Figure 1.5 on page 22). When the size difference between the B and B' cations is large, the structure may become tetragonally distorted, resulting in two distinct sites for the B and B' ions (here, B represents the larger cation) [55,65]. This distortion results in the formation of one of two possible crystal lattices; one described by the $I4/mmm$ space group and one described by the $I4/m$ space group [52,62]. In the $I4/mmm$ lattice, the B' octahedra undergo compression along the c-axis while the B octahedra are elongated along the c-axis. In the $I4/m$ unit cell, the B and B' octahedra undergo opposing rotations, causing the octahedra to buckle, which results in expanded BO_6 octahedra and compressed $B'O_6$ octahedra [52, 62]. The transition from the structure to the

[1] A version of this paper has been published. Copyright is owned by Elsevier B.V. Reprinted with permission from J.R. Hayes and A.P. Grosvenor, *Journal of Alloys and Compounds*, (2012) 537, 323-331. DOI: 10.1016/j.jallcom.2012.05.056

$I4/m$ structure is shown in Figure 1.5 on page 22. An example of a system that undergoes a transition from a cubic to a tetragonal lattice with variation in composition is the $Sr_2Fe_{2-x}Mo_xO_6$ double perovskite solid-solution. While X-ray diffraction studies have not conclusively shown whether Sr_2FeMoO_6 adopts the $I4/m$ or $I4/mmm$ space group, the results of these distortions are similar, and the $I4/m$ structure is assumed in this study [52, 74, 160]. This assumption is supported by a previous study which used group theory to suggest that $I4/m$ symmetry must be adopted [53]. (This system is known to be oxygen-deficient, but it will be referred to here as $Sr_2Fe_{2-x}Mo_xO_6$ for simplicity [59, 73].)

Sr_2FeMoO_6 has been shown to exhibit a variety of interesting magnetic properties [57, 73, 82, 87]. For example, these materials are ferrimagnetic, with a Curie temperature reported to be between 410-450 K [62]. Here, ferrimagnetism arises from a double-exchange mechanism, which results from the ferromagnetic alignment of Fe 3d electrons and the antiferromagnetic alignment of Mo 4d electrons [66, 87, 161]. This model assumes Fe adopts a 3+ oxidation state and Mo adopts a 5+ oxidation state, and the theoretical maximum saturation magnetization is 4 μB, though experimentally, the saturation magnetization has always been observed to be less [80, 162, 163]. This reduced experimental value has been linked to the amount of antisite disorder present, in which Fe occupies a Mo site (and vice versa), leading to antiferromagnetic coupling between adjacent Fe ions [59, 70, 72, 164–166]. In addition to being ferrimagnetic, Sr_2FeMoO_6 is known to exhibit magnetoresistive behavior, in which a decrease in the resistivity of the material is observed upon applying a magnetic field [70, 164, 167]. This behavior arises from the half-metallic character of Sr_2FeMoO_6, in which a spin-polarized band of Mo t_{2g}–O 2p–Fe e_g states crosses the Fermi level [57]. The magnetoresistive behavior has also been shown to be impacted by the presence of insulting grain-boundaries (when low magnetic fields are applied) and, because of this low-field magnetoresistance, Sr_2FeMoO_6 has been investigated for use in spintronic devices [61, 70, 83]. To better understand the origins of the aforementioned properties, and to better utilize these properties in technological applications, it is necessary to know what oxidation states are adopted by Fe and Mo in these compounds.

While there are a wide variety of studies on the valence states of Fe and Mo, no consensus has been reached [74, 75, 87–91, 166]. Although no definitive values have been reported, the average oxidation state of Fe is generally found to be between 2+ and 3+ while the oxidation state of Mo is found to be between 5+ and 6+ [75, 80, 87–91, 161]. This disagreement probably arises from the complex nature of Sr_2FeMoO_6, with the material being sensitive to a wide variety of variables. For example, Sr_2FeMoO_6 is not a stoichiometric compound, but rather a member of the $Sr_2Fe_{2-x}Mo_xO_6$ ($0 \leq x \leq 2$) solid solution. As such, the system is sensitive to both the composition and synthetic conditions employed [59, 63]. Despite this, no studies have directly investigated how the oxidation states of Fe and Mo vary in $Sr_2Fe_{2-x}Mo_xO_6$ materials with changing Mo content.

X-ray absorption near-edge spectroscopy (XANES) is a technique perfectly suited for such a study. In this study, Fe K- and Mo K-edge XANES spectra have been collected from a series of $Sr_2Fe_{2-x}Mo_xO_6$ compounds produced by the reaction of oxides under $H_{2(g)}$ in order to determine how the oxidation states of Fe and Mo depend on Mo content. These experiments have also provided information about how the oxygen deficiency (and coordination number) in these systems change with varying Mo content. Additionally, to better understand how preparation conditions might affect these oxidation states, Fe K- and Mo K-edge XANES spectra have been collected from samples that were annealed under a vacuum environment and compared to those from the originally prepared materials.

In this chapter, the effects of changes in oxidation state and coordination number on the pre-edge will be explored. Previous XANES studies have already provided insight into how to track changes in either the oxidation state or the coordination number when only one value is changing. However, determining how these values change when the oxidation state and coordination number is changing simultaneously is usually not explored. By combining the analysis of both the Fe K- and Mo K-edge XANES spectra from the $Sr_2Fe_{2-x}Mo_xO_6$ compounds, an enhanced understanding of how both the oxidation state and coordination number change with varying Mo content has been achieved. Providing examples of how to perform such an analysis will enhance general interpretation of the pre-edge from other materials where simultaneous changes in the oxidation

state and coordination number may occur.

2.2 Experimental

2.2.1 Synthesis

A series of $Sr_2Fe_{2-x}Mo_xO_6$ (x = 0.25, 0.50, 0.65, 0.85, 1.0) compounds were synthesized via a common solid-state synthesis route [59, 63, 74]. Stoichiometric amounts of $SrCO_3$ (Alfa Aesar, 99%), MoO_3 (Acrōs Organic, $>$ 99%), and Fe_2O_3 (Alfa Aesar, 99.945%) were mixed and ground using an agate mortar and pestle. In materials with x $\geq$0.65, the mixture was pressed into a pellet at 6 MPa and heated to 900 °C over 8 h under flowing 5% H_2 (balance N_2), held at 900 °C for 6-8 h (higher values of x required longer heating times), and cooled to room temperature over $\sim$4.5 h. For materials with x $\leq$ 0.575, it was found that pressing the precursor materials into a pellet resulted in a phase-impure material. In these cases, the loose powder was heated in air at 1100 °C for $>$ 12 h to decompose $SrCO_3$ to SrO. The powdered mixture was then heated to 900 °C over 8 h under flowing 5% H_2 (balance N_2), held at 900 °C for 3-4 h (higher values of x required longer heating times), and then cooled to room temperature over $\sim$4.5 h. While many other studies have reported the use of higher temperatures (1000-1200 °C) to synthesize these materials, in this study, an acceptable level of phase purity could not be achieved using temperatures $>$ 900 °C when heated under 5% H_2 (balance N_2) [59, 63, 74]. In all cases, the gas flow was monitored using a mineral oil bubbler and the flow was kept at 1-2 bubbles/s. The flow rate was found to strongly impact the purity of the resultant product, as too high or too low a flow rate resulted in the formation of phase-impure materials, with Sr_2MoO_4 (too high a flow rate) and $SrMoO_4$ (too low a flow rate) comprising the principle impurity phases. The as-synthesized materials were also annealed under vacuum to study the impact of ordering on the oxidation states of the metal ions [16]. Aliquots of the as-synthesized samples were loaded into alumina crucibles and sealed in fused-silica tubes under rough vacuum and the samples were heated to 1050 °C from room temperature over $\sim$7 h, held at this temperature for 12 h, and then slowly cooled to room temperature ($\sim$5 h).

Oxygen-deficient $SrFeO_{2.75}$-perovskite, $Sr_2Fe_2O_5$-brownmillerite, and FeO were also synthe-

sized to act as standards. To synthesize the $SrFeO_{2.75}$ and $Sr_2Fe_2O_5$ samples, stoichiometric amounts of $SrCO_3$ (Alfa Aesar, 99%) and Fe_2O_3 (Alfa Aesar, 99.945%) were mixed, pelleted at 6 MPa, and heated in air at 1100 °C for 24 h. To control the O-stoichiometry, the samples were then reground, and subjected to separate heat treatments. The $SrFeO_{2.75}$ sample was heated at 1200 °C for 48 h, cooled to 600 °C, and held at this temperature for 24 h before being slowly cooled to room temperature. The $Sr_2Fe_2O_5$ sample was heated at 1200 °C for 48 h and quench-cooled in liquid nitrogen [25]. FeO was synthesized by mixing stoichiometric amounts of Fe metal powder (Alfa Aesar 99.5%) and Fe_2O_3 (Alfa Aesar, 99.945%) and pressing the resultant powder into a pellet at 6 MPa. The pellet was then heated at 900 °C for 12 h under flowing $N_{2(g)}$ [168,169]. Phase purity of all materials synthesized was determined using powder X-ray diffraction (XRD). Diffraction patterns were collected using a PANalytical Empyrean X-ray diffractometer equipped with a monochromatic Cu $K_{\alpha 1}$ (λ = 1.5406 Å) X-ray source. Lattice parameters were determined using the UnitCell software program by assuming a double perovskite cubic unit cell for all values of x in the chemical formula [170].

2.2.2 XANES

Fe K-edge and Mo K-edge spectra of the as-synthesized and annealed $Sr_2Fe_{2-x}Mo_xO_6$ samples were collected using the Pacific Northwest Consortium/X-ray Science Division Collaborative Access Team (PNC/XSD-CAT, Sector 20) bending magnet beamline (20BM) located at the Advanced Photon Source (APS), Argonne National Laboratory. A silicon (111) double crystal monochromator with harmonic rejection was used, which at 7000 eV has a resolution of 1 eV and a photon flux of $\sim 10^{11}$ photons/second [171]. Samples were finely ground and sandwiched between layers of Kapton tape and the number of layers of tape was varied to maximize absorption. Samples were mounted at a $\sim 45°$ angle to the incident beam with transmission spectra being collected using N_2-filled ionization chambers while partial fluorescence yield spectra were collected using a Canberra 13-element Ge detector. The spectra were collected using an energy step of either 0.15 eV (Fe

K-edge) or 0.30 eV (Mo K-edge) through the edge energy. The Fe K-edge spectra were collected from 200 eV below the edge (7112 eV) to k = 15, which is 857.2 eV above the edge. The Mo K-edge spectra were collected from 200 eV below the edge (20000 eV) to k = 13 (643.9 eV above the edge). The Fe K-edge spectra were calibrated using either an Fe reference foil (having a known Fe K-edge absorption-edge energy of 7112 eV), while the Mo K-edge spectra were calibrated using a Mo reference foil (having a known Mo K-edge absorption energy of 20000 eV) [9]. The spectra from the reference foils were collected concurrently in transmission mode with the spectra from each oxide studied. All spectra collected were calibrated, normalized, and analyzed using the Athena software program [172]. The Fe K-edge spectra were normalized using a pre-edge range of -32 eV $\rightarrow$ -20 eV and a post-edge region ranging between 47 eV $\rightarrow$614 eV (relative to the absorption-edge energy, E_o). The Mo K-edge spectra were normalized using a pre-edge range of -66 eV $\rightarrow$-35 eV and a post-edge region ranging between 130 eV $\rightarrow$580 eV. As Sr_2FeMoO_6 materials have been shown to degrade into $SrMoO_4$ and other products over time, to eliminate the possibility of sample age significantly affecting the collected spectra, all spectra were collected within one month of sample preparation [173].

2.3 Results

2.3.1 Structure

To confirm phase purity, and to study how the structure of the $Sr_2Fe_{2-x}Mo_xO_6$ compounds change with varying Mo content, powder XRD patterns of the as-synthesized materials have been collected and are presented in Figure 2.1. With the exception of Sr_2FeMoO_6, single phase $Sr_2Fe_{2-x}Mo_xO_6$ compounds were prepared. In the case of Sr_2FeMoO_6, an 85-90% phase-pure material was synthesized, with small amounts ($<$ 6% each) of $SrMoO_3$, Sr_2MoO_4, and intermetallic $Fe_{1-x}Mo_x$ impurities being detected. (The exact composition of the intermetallic phase is not known [73].) The (101) reflection (denoted by an asterisk in Figure 2.1), which corresponds to ordering of the

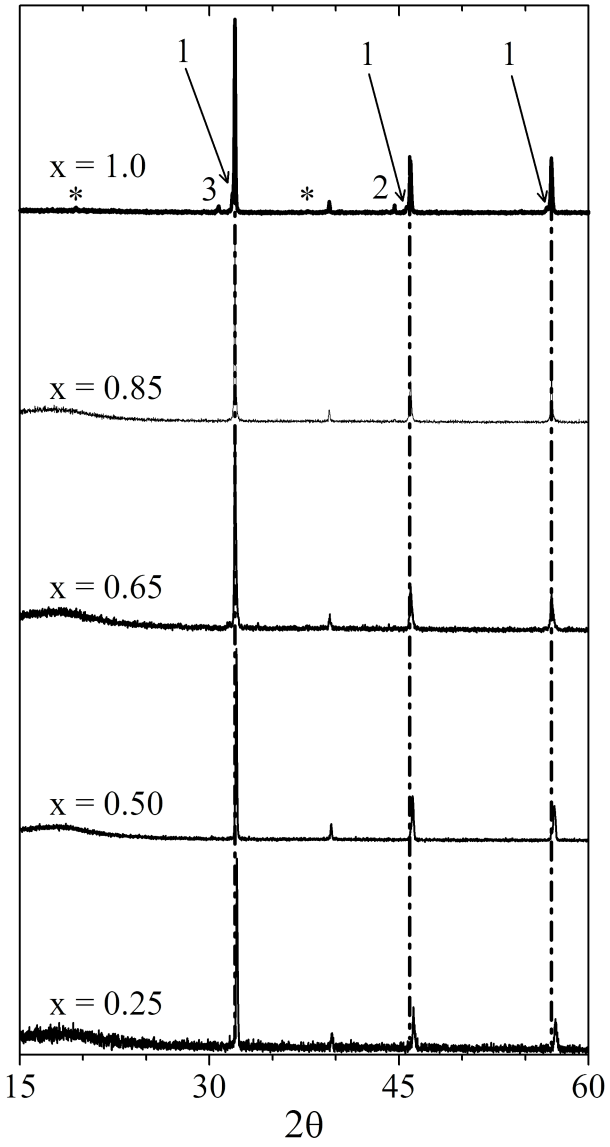

Figure 2.1: Powder XRD patterns from as-synthesized $Sr_2Fe_{2-x}Mo_xO_6$ materials. Sr_2FeMoO_6 (x = 1.0) showed the following impurities: 1) $SrMoO_3$; 2) $Fe_{1-x}Mo_x$ intermetallic; and 3) Sr_2MoO_4. In addition, superstructural peaks from the tetragonal structure (denoted by asterisks) are observed in the Sr_2FeMoO_6 sample. All reflections were observed to shift to lower 2θ angles with increasing x. The broad feature found at $\sim 18^\circ$ in the patterns with $x < 1.0$ are from mineral oil, which was used to mount these samples.

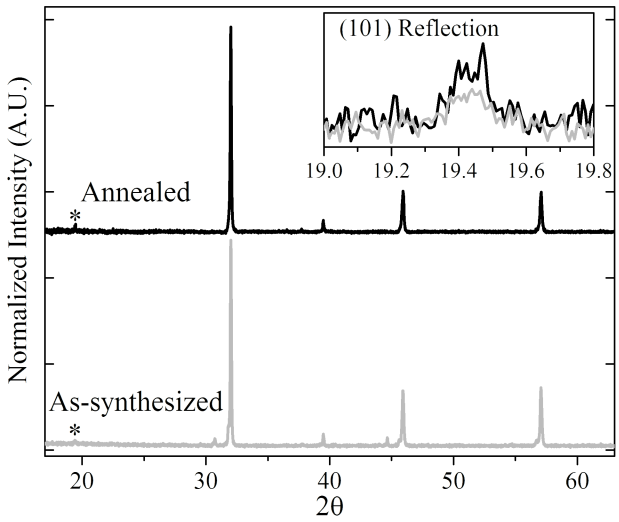

Figure 2.2: The normalized powder XRD patterns from the as-synthesized (grey) Sr_2FeMoO_6 material and after being annealed (black) are compared. Here, the patterns are offset along the y-axis for clarity. After annealing, the reflections at 30.6° and 44.7°, which are associated with impurity phases, were no longer observed. The (101) reflection (marked by an asterisk), is shown in the inset. The intensity of this reflection is greatly increased upon annealing in vacuum, indicating that a more ordered structure is present.

Fe and Mo sites was only observed in the Sr_2FeMoO_6 compound, indicating a high degree of disorder in the other compounds synthesized [76]. It has been previously shown that the intensity ratio of the (101) reflection to the sum of the (200) and (112) reflections may be used as a measure of the amount of antisite disorder experienced by the Fe/Mo sites, with high values corresponding to less antisite-disorder [76]. For the as-synthesized x = 1.0 sample, the (101):((200)+(112)) ratio is 0.024, indicating that there is high degree of antisite disorder in this material. (In the systems with $x \neq 1.0$, the ratio is zero, indicating that the amount of ordering of the transition metal sites in these systems is too low to be determined). Compared to previous studies, where the reaction temperature was higher (1200 °C), this ratio was $\sim$0.046, which suggests that the lower reaction temperature used in this study is not sufficient to achieve high levels of site ordering [74, 76].

Upon annealing under vacuum, the XRD pattern (Figure 2.2) shows that the ordering of Sr_2FeMoO_6 (x = 1.0) increases considerably compared to the as-synthesized version. The powder XRD patterns from the as-synthesized and vacuum annealed Sr_2FeMoO_6 samples (Figure 2.2) show that in the as-synthesized materials the (101):((200)+(112)) ratio is 0.024 while in the vac-

uum annealed sample, the ratio is 0.033. This observation implies that the material becomes more ordered upon annealing (i.e., the amount of antisite disorder is reduced) [76]. Additionally, the phase-purity of Sr_2FeMoO_6 increased dramatically with vacuum annealing, which was observed by the complete disappearance of peaks from the Sr_2MoO_4 and $Fe_{1-x}Mo_x$ phases in the powder XRD pattern (Figure 2.3). In the other annealed $Sr_2Fe_{2-x}Mo_xO_6$ compounds ($x < 1.0$), no super-structural reflections were observed in the corresponding powder XRD pattern; however, the other reflections were observed to narrow considerably (not shown).

The XRD patterns collected in this study were also used to calculate the lattice parameters of the $Sr_2Fe_{2-x}Mo_xO_6$ materials. The a lattice parameter was calculated assuming a cubic unit cell. The lattice constants are plotted as a function of Mo content in 2.3a, and show a sudden increase when $x \geq 0.65$. For all values of $x \geq 0.65$, the unit cell is observed to only increase slightly. This shift is also clearly observed in the powder XRD patterns (cf. Figure 2.3b). The sudden and relatively large change in the lattice constant between $Sr_2Fe_{1.50}Mo_{0.50}O_6$ and $Sr_2Fe_{1.65}Mo_{0.35}O_6$ is indicative of a large change in the crystal lattice. In other structural studies of $Sr_2Fe_{2-x}Mo_xO_6$, this change has been shown to coincide with a transformation from a cubic to a tetragonal crystal structure. These studies performed Reitveld refinements on powder XRD data, and found the quality of the fit determined using a tetragonal model was higher than that determined using a cubic model when $x \geq 0.7$ [62,63,160]. In this study, upon annealing under vacuum, no significant changes in the lattice parameter were observed between the as-synthesized and annealed samples of a given composition.

2.3.2 Fe K-edge XANES of the As-Synthesized Materials

Fe K-edge XANES spectra, which are presented in Figure 2.4 , were collected to determine the oxidation state of Fe in the $Sr_2Fe_{2-x}Mo_xO_6$ materials and to investigate the oxygen stoichiometry in these systems. Spectra from a series of standard compounds having known Fe oxidation states and coordination environments were also collected to aid in the interpretation of the $Sr_2Fe_{2-x}Mo_xO_6$

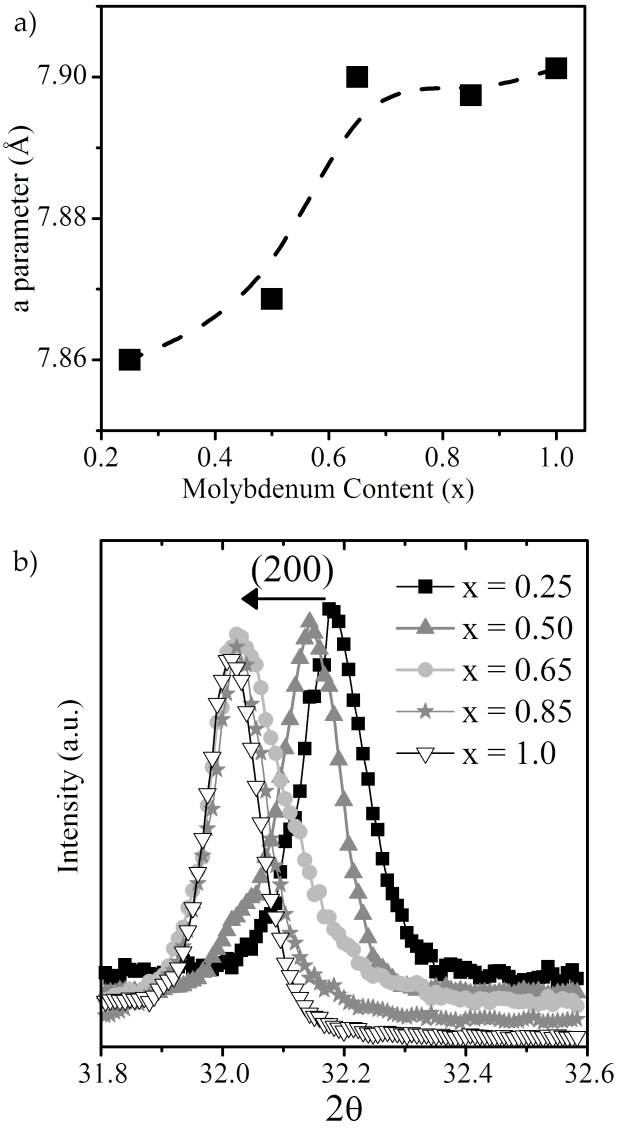

Figure 2.3: (a) The lattice parameters calculated using a cubic unit cell for the $Sr_2Fe_{2-x}Mo_xO_6$ system as a function of Mo content (x). Between x = 0.50 and x = 0.65, a large increase is observed. The dashed line is included as a guide to the eye and the size of the symbols is representative of the uncertainty of the measurement. (b) The 2θ angle of the (220) reflection (indexing assumes a cubic structure) was found to shift to lower 2θ values as x increases, reaching the lowest value when x = 0.65. The large change in 2θ between x = 0.50 and x = 0.65 is reflective of the significant variation in the lattice shape.

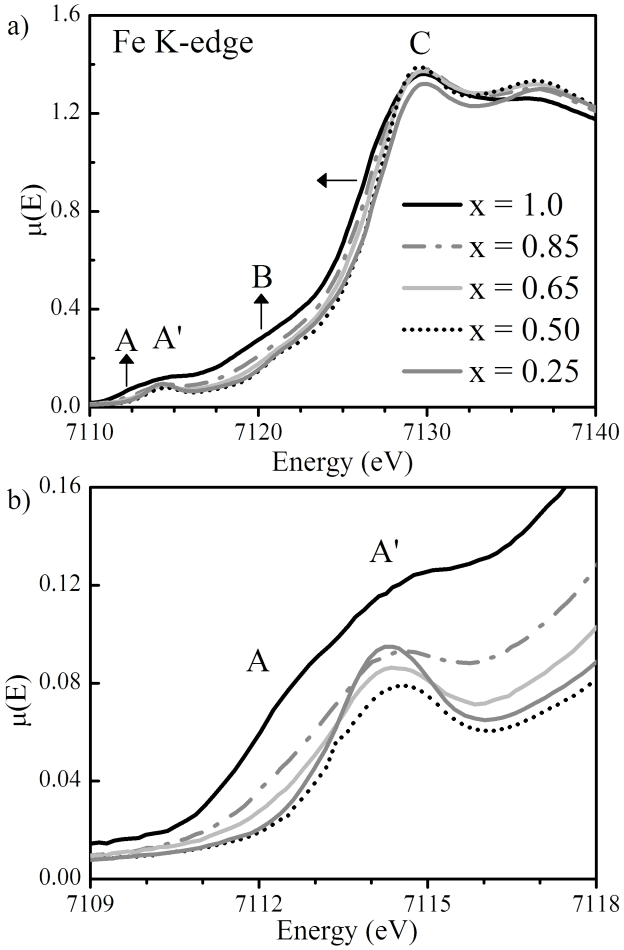

Figure 2.4: (a) Fe K-edge spectra from the as-synthesized $Sr_2Fe_{2-x}Mo_xO_6$ materials. Features A and A' make up the pre-edge region and consist of transitions to Fe 3d states while features B and C are attributed to main-edge excitations resulting from Fe 1s→Fe 4p excitations. As the Mo content increases, features A and B increase in intensity and the absorption edge energy shifts to lower energy, indicating that the average Fe oxidation state is reduced (changes are shown by arrows). (b) The pre-edge region of the Fe K-edge spectra. As the Mo content is increased, feature A significantly increases in intensity. The intensity of feature A' is linked to the O deficiency of the materials and initially decreases as x is increased from x = 0.25 to x = 0.50. As x is increased to values greater than 0.50, the intensity of feature A is observed to increase.

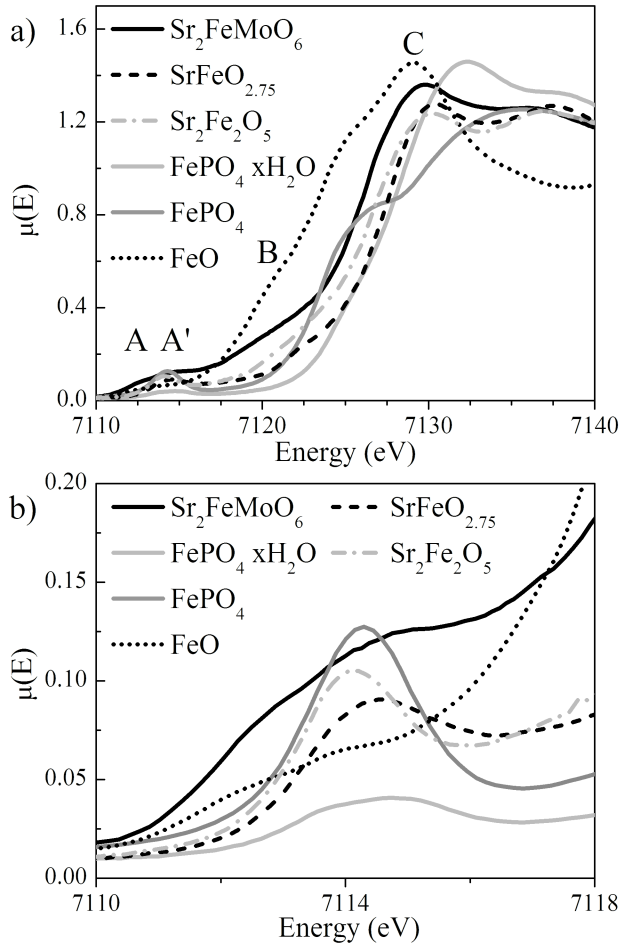

Figure 2.5: (a) Fe K-edge spectra from a series of standards is presented along with the Fe K-edge spectrum from the as-synthesized Sr_2FeMoO_6 sample. (The spectra of $FePO_4$ and $FePO_4 \cdot xH_2O$ are from [28].) (b) The pre-edge region of the Fe K-edge spectra. Comparison of the spectra from Sr_2FeMoO_6 and FeO indicates that feature A is linked to the presence of Fe^{2+} while the link between the oxygen deficiency and the intensity of feature A' is corroborated by comparison of the spectra from $SrFeO_{2.75}$ (CN $<$ 6) and $Sr_2Fe_2O_5$ (average CN = 5).

spectra, and are presented in Figure 2.5 . As is observed in Figure 2.4a, there are four distinct features in the spectra from $Sr_2Fe_{2-x}Mo_xO_6$, which have been labeled as A, A', B, and C. Features A and A' make up the pre-edge region (see Figure 2.4b), and are assigned to forbidden, quadrupolar, 1s $\rightarrow$ Fe 3d excitations [14]. By comparison with the Fe K-edge spectrum from FeO (Figure 2.5), feature A is assigned to Fe^{2+} 1s $\rightarrow$ Fe 3d excitations, while comparison to the Fe K-edge spectra from $SrFeO_{2.75}$ and $Sr_2Fe_2O_5$ indicates that feature A' is attributable to Fe^{3+} 1s $\rightarrow$ Fe 3d excitations. In $Sr_2Fe_{1.75}Mo_{0.25}O_6$, only feature A' is observed, implying that only Fe^{3+} is observed in

this compound. As the Mo content is increased to x = 0.50, feature A' decreases in intensity and no other features are observed. As the coordination number (CN) of the Fe centre decreases, and the local inversion symmetry is lost, 4p states overlap the 3d states, which adds a dipolar character to the pre-edge excitation. This increased dipolar character results in the observation of a more intense pre-edge peak (cf. spectra from $FePO_4 \cdot xH_2O$ (CN_{Fe}= 6) and $SrFeO_{2.75}$ ($CN_{Fe} < 6$) in Figure 2.5) [16, 25]. Here, it is noted that the increase in dipolar character is a result of changes in the local coordination structure only, and is not caused by distortions of the crystal lattice symmetry. Comparing the spectra presented in Figure 2.4 to those in Figure 2.5 leads to the conclusion that the decrease in intensity of feature A' observed in Figure 2.4b as the Mo concentration is increased from x = 0.25 to x = 0.65 is a result of the system becoming less O deficient (i.e., the Fe CN increases). As the Mo content is further increased to $x \geq 0.65$, the intensity of feature A' increases, as does the intensity of feature A, which implies that some Fe^{2+} is present. While feature A may contribute some intensity to feature A' as the two features are not fully resolved, the fact that the intensities of both features increase simultaneously as x changes from 0.50 to 1.0 indicates that $Sr_2Fe_{2-x}Mo_xO_6$ becomes more O deficient as x increases from 0.65 to 1, as an increase in the concentration of Fe^{2+} would decrease the number of unoccupied Fe 3d states. Examination of Figure 2.4b also indicates that the concentration of Fe^{2+} increases significantly as x is increased when $x \geq 0.65$.

To confirm the analysis of the changes in the pre-edge region, the main-edge can also be investigated. Features B and C comprise the main-edge, and arise from dipolar 1s $\rightarrow$ Fe 4p excitations. By comparing the $Sr_2Fe_{2-x}Mo_xO_6$ spectra (Figure 2.4) to the spectrum from FeO (Figure 2.5), it is clear that feature B arises from the excitation of Fe^{2+} metal centres. As was the case for feature A in the pre-edge region, almost no change in intensity of feature B was observed as x was varied from 0.25 to 0.50; however, the intensity of feature B was found to vary significantly with increasing Mo content when $x \geq 0.65$. The presence of Fe^{2+} in these materials with varying x is further supported by the observed shifts in the main-edge energy of these spectra, which is defined as the inflection point of the main-edge (determined from the derivative spectrum by finding the

peak maximum of the feature corresponding to the main-edge). The decrease in absorption energy with greater substitution of Fe for Mo ($\Delta E \approx 1.5$ eV), is ascribed to the presence of lower-energy valence Fe 4p-O 2p states, caused by increased ground-state screening of the Fe nuclear charge which results from a reduction of Fe^{3+} to Fe^{2+} [28].

The intensity of feature C initially increases between $Sr_2Fe_{1.75}Mo_{0.25}O_6$ and $Sr_2Fe_{1.50}Mo_{0.50}O_6$, but then remains relatively constant as the Mo content is further increased. This increase in intensity is likely linked to the O deficiency of the system. Given that there must be a fixed number of Fe 4p states, as the Fe 4p character of the pre-edge peak is reduced with increasing CN (i.e., decreased O deficiency; cf. Feature A' in Figure 2.4b), the remaining Fe 4p states interact with the O 2p states (feature C), resulting in the observation of the increase in intensity of feature C in Figure 2.4. Multiscattering resonances (MSR), which are part of the extended X-ray absorption fine structure (EXAFS), may also contribute to the intensity of feature C. The changes in the Fe K-edge XANES spectra as Mo content is increased may be summarized as follows:

1. For values of $x \leq 0.50$, Fe predominantly adopts a 3+ oxidation state
2. For $x > 0.50$, the average oxidation state of Fe decreases with increasing Mo content
3. The O deficiency of the structure decreases as Mo content increases when $x \leq 0.50$, but increases with increasing Mo content when $x > 0.50$
4. For no composition studied here was a fully oxygen stoichiometric compound synthesized.

2.3.3 Mo K-edge XANES of the As-Synthesized Materials

Mo K-edge spectra from the $Sr_2Fe_{2-x}Mo_xO_6$ compounds were collected to better understand how the Mo oxidation state changes with substitution, and are presented in Figure 2.6a . In addition, to interpret changes in these Mo K-edge spectra, XANES spectra from several reference compounds

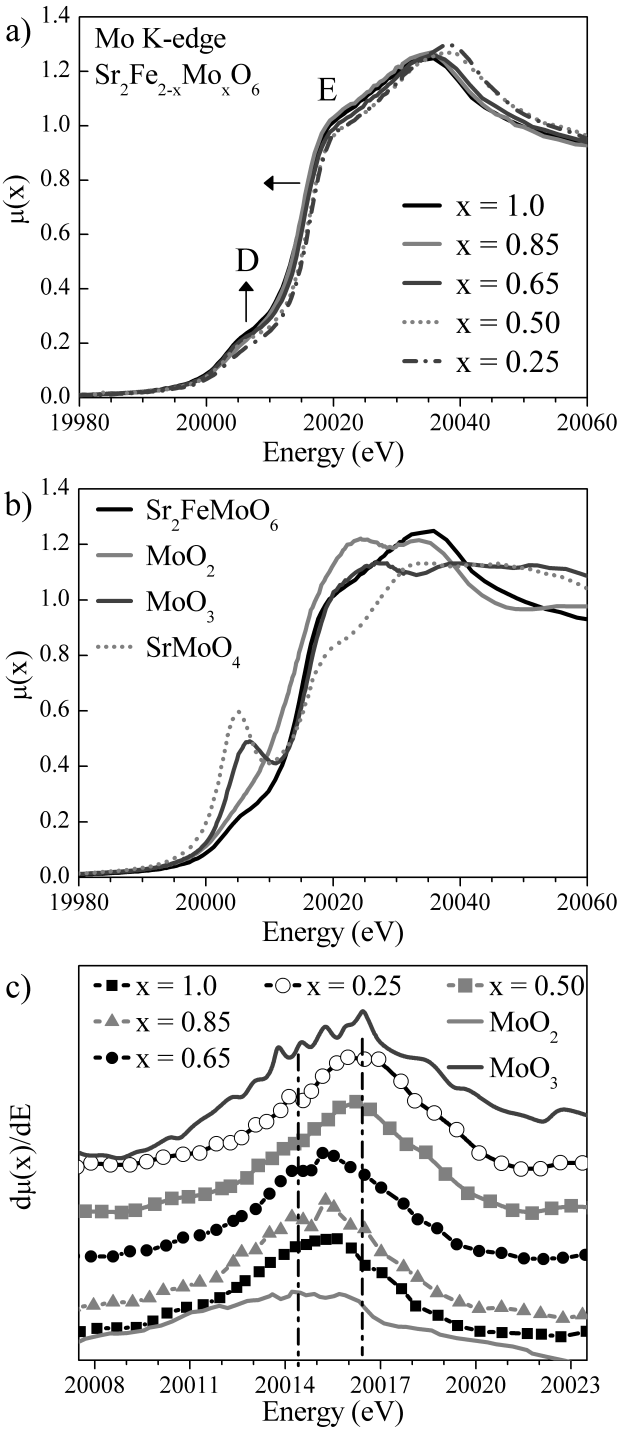

Figure 2.6: (a) Mo K-edge spectra from the as-synthesized $Sr_2Fe_{2-x}Mo_xO_6$ materials. As the Mo content (x) increases, feature D increases in intensity, indicating a decrease in the Mo CN. Arrows are included to show how features change as x increases. (b) The Mo K-edge spectra from a series of standards, as well as the as-synthesized Sr_2FeMoO_6 sample, are plotted. (Mo adopts a 4+ oxidation state in MoO_2 and a 6+ oxidation state in MoO_3 and $SrMoO_4$.) (c) The derivative plot of the K-edge spectra from the $Sr_2Fe_{2-x}Mo_xO_6$ samples as well as the MoO_2 and MoO_3 standards is shown. For clarity, the MoO_2 derivative spectrum has been smoothed and the lines represent the peak energies of MoO_2 and MoO_3.

were collected, and are presented in Figure 2.6b. Two prominent features are observed in these spectra, and are labeled as D and E.

Feature D in Figure 2.6 arises from forbidden transitions to Mo 4d states (much like in the Fe K edge), and the intensity of this feature appears to be related to the Mo content in $Sr_2Fe_{2-x}Mo_xO_6$ [26, 174–176]. When x = 0.25 in $Sr_2Fe_{2-x}Mo_xO_6$, this feature is muted, while for higher values of x, the intensity of feature D increases. In all cases, the intensity of feature D is far less than that observed in the spectra from $SrMoO_4$ and MoO_3, in which Mo occupies a tetrahedral site or a highly distorted octahedral site, respectively (Figure 2.6b). (In $SrMoO_4$, the highly distorted octahedra result in significant overlap between the Mo 4d and 5p states [177–179].) In the $Sr_2Fe_{2-x}Mo_xO_6$ compounds, the increase in the intensity of feature D with increasing Mo content suggests that, overall, the Mo coordination decreases with greater Mo content. However, this interpretation is tentative as it is difficult to separate changes in the intensity of feature D from shifts of the main absorption edge energy, given the poor energy resolution of Mo K-edge spectra ($\sim$4.5 eV when core-hole lifetime effects are considered) [26].

Feature E is attributed to the main-edge excitation, which arises from Mo 1s $\rightarrow$ Mo 5p excitations [26]. The main-edge energy is sensitive to changes in oxidation state and can be used to elucidate how the oxidation state of Mo in the $Sr_2Fe_{2-x}Mo_xO_6$ compounds changes with varying stoichiometry. Figure 2.6c shows the derivative spectra from the $Sr_2Fe_{2-x}Mo_xO_6$ compounds along with that from the MoO_2 and $SrMoO_4$ reference compounds. When the Mo content is low (x = 0.25), the derivative maximum is at the same energy as that from the $SrMoO_4$spectrum, indicating that Mo adopts an average oxidation state of 6+ in this material. As the Mo content increases in $Sr_2Fe_{2-x}Mo_xO_6$ to x = 0.50, the peak maximum of the derivative spectrum is observed to shift to lower energy, indicating a reduction in the Mo oxidation state (Figure 2.6c). When the Mo content is further increased (x = 0.65), the derivative peak again shifts to lower energy, though it is still slightly higher than that of MoO_2 (Mo^{4+}). This observation suggests that Mo largely adopts a 5+ oxidation state when $x \geq 0.65$, though given the width of the MoO_2 derivative peak, it is possible that a minor quantity of Mo^{4+} is also present. (The width of the derivative peaks also shows that

a small amount of Mo^{6+} is likely present also when $x > 0.25$). Interestingly, as the Mo content is increased beyond x = 0.65, no further shifts in energy are observed.

2.3.4 Vacuum Annealing

To understand how ordering of the Mo and Fe ions in $Sr_2Fe_{2-x}Mo_xO_6$ might impact the oxidation state and electronic environment of the metal centers, the as-synthesized compounds were annealed in an evacuated ampule and investigated by XANES. The Fe K- and Mo K-edge XANES spectra from these annealed compounds are compared to the corresponding spectra from the as-synthesized samples in Figure 2.7and Figure 2.8, respectively. Large changes in the Fe K-edge spectra were observed between the as-synthesized and annealed $Sr_2Fe_{2-x}Mo_xO_6$ compounds when $x \geq 0.65$ (Figure 2.7); however, no change was observed in the spectra from $Sr_2Fe_{1.75}Mo_{0.25}O_6$ and $Sr_2Fe_{1.50}Mo_{0.50}O_6$. For compounds where $x \geq 0.65$, features A, A' and B decreased in intensity while the intensity of feature C was found to increase. These changes are consistent with the oxidation of Fe^{2+} in the $Sr_2Fe_{2-x}Mo_xO_6$ materials and an increase in the Fe CN. The source of oxygen is attributed to residual $O_{2(g)}$ left in the evacuated ampule. In previous studies on the synthesis of $SrMoO_3$, a compound that is highly related to the $Sr_2Fe_{2-x}Mo_xO_6$ compounds studied here, it was shown that oxygen partial pressures as low as 10^{-14} Torr could lead to the oxidation of $SrMoO_3$ [179–181]. As the ampules containing the annealed samples were only sealed under rough vacuum, the partial pressure of $O_{2(g)}$ present was much higher than 10^{-14} Torr. Oxidation of the Fe centres leads to an increase in the Fe CN, which was observed as a decrease in the intensity feature A' owing to a decrease in mixing of the Fe 3d and 4p states. The decrease in intensity of feature A is also explained by the oxidation of Fe^{2+} to Fe^{3+}. Further, feature B (section 2.3.2) was also observed to decrease in intensity, compared to the as-synthesized compounds because of the oxidation of Fe^{2+} to Fe^{3+}. The increase in intensity of feature C was a result of the greater number of Fe 4p-O 2p states available for 1s electrons to be excited to, which is indicative of increased Fe CN. Interestingly, the magnitude of the changes observed upon annealing increased with greater Mo content. The reason for this observation is simple: at higher Mo concentrations, the amount of

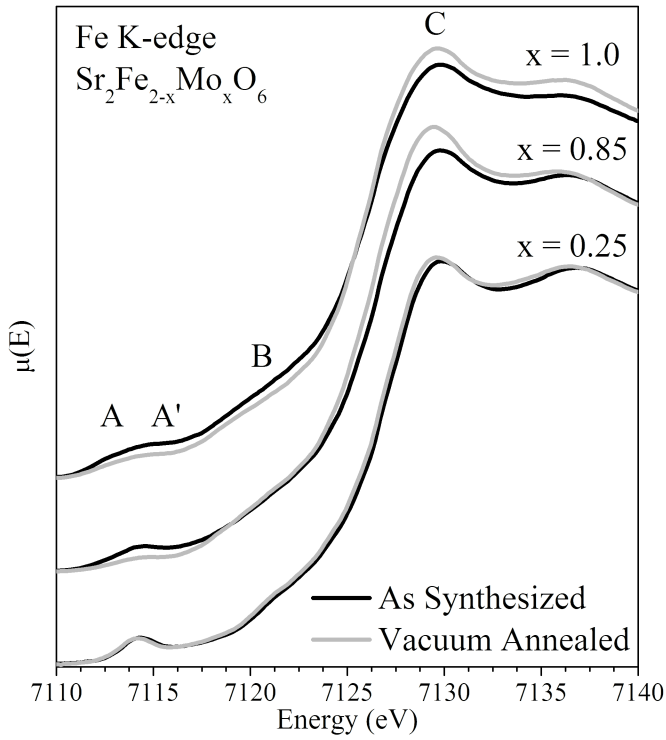

Figure 2.7: The Fe K-edge spectra from several of the vacuum annealed $Sr_2Fe_{2-x}Mo_xO_6$ samples are presented along with the corresponding as-synthesized materials (spectra are offset for clarity). No change in the spectra were observed upon annealing when the Mo content is low ($x \leq 0.50$). When $x > 0.50$, the intensities of features A' and B in the spectra from the vacuum annealed samples decrease compared to the as-synthesized samples while the intensity of feature C increases, indicating that the materials have been oxidized and that the Fe CN increases.

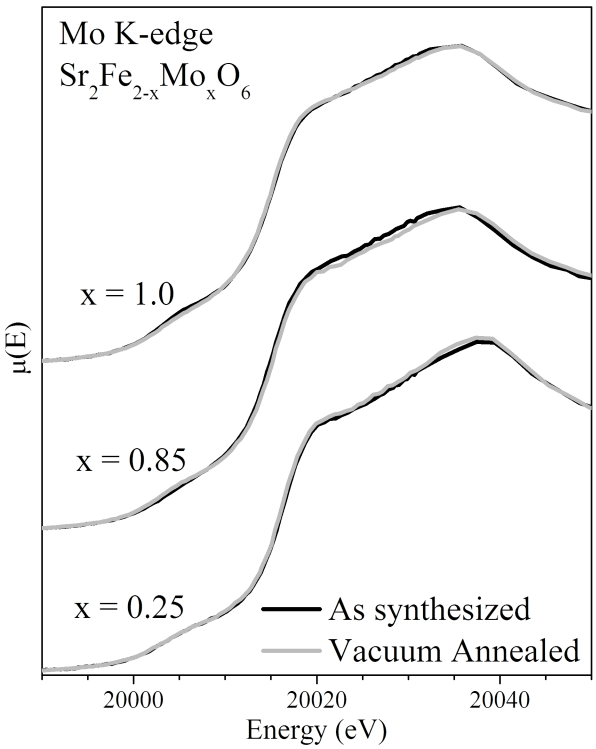

Figure 2.8: The Mo K-edge spectra from several of the vacuum annealed $Sr_2Fe_{2-x}Mo_xO_6$ spectra are presented along with the corresponding as-synthesized materials (spectra are offset for clarity). Little to no change in the spectra was observed for all values of x.

Fe^{2+} present which can be oxidized is greater.

The Mo K-edge spectra of the annealed and synthesized samples (shown in Figure 2.8) reveal that little to no change upon annealing. This observation does not indicate that no changes occur at the Mo sites. Instead, this result likely indicates that the magnitude of the changes is not detectable within the limits of the resolution of the Mo K-edge XANES spectra reported here.

2.4 Discussion

In this study, a series of $Sr_2Fe_{2-x}Mo_xO_6$ double perovskites have been synthesized and studied by XANES to better understand the relationship between the concentration of Mo and the oxidation states of Fe and Mo, and the level of O deficiency in these materials. In $Sr_2Fe_{1.75}Mo_{0.25}O_6$, the Fe K-edge XANES spectrum (Figure 2.4) indicates that Fe adopts a 3+ oxidation state while the

Mo K-edge XANES spectrum (Figure 2.6a) indicates that Mo adopts a 6+ oxidation state. Given the similarity of the effective ionic radii of Fe^{3+} and Mo^{6+} (0.645 Å and 0.59 Å, respectively), a near-random distribution of Mo^{6+} and Fe^{3+} would lead to an entropy stabilized system, which could be thought of as a solid-solution derivative of the cubic $SrFeO_{3-\delta}$ perovskite structure (here δ indicates an unknown, but small amount of O deficiency) [52, 55, 153]. This suggestion is confirmed in this study by the lack of observation of the (101) reflection in the corresponding powder XRD patterns (Figure 2.2). (While $SrFeO_{3-\delta}$ is reported to have a mix of Fe^{3+} and Fe^{4+} when δ is small, given the reducing conditions used to synthesize the $Sr_2Fe_{2-x}Mo_xO_6$ materials analyzed in this study, the formation of Fe^{4+} is not likely). In the case of $Sr_2Fe_{1.75}Mo_{0.25}O_6$, an oxygen deficient structure is required to achieve charge balance, as the maximum number of O atoms possible per formula unit is 5.4, assuming only Fe^{3+} and Mo^{6+} are present. Oxygen deficiency in this compound was confirmed in this study by the intense pre-edge feature in the Fe K-edge spectrum (Figure 2.4). As the Mo content is increased to $Sr_2Fe_{1.50}Mo_{0.50}O_6$, the level of O deficiency is reduced, consistent with the replacement of Fe^{3+} by Mo^{6+} (as this leads to an overall increase of the average cationic charge). The increase in O content also explains the small increase of the lattice parameter (Figure 2.3a) and the decrease in the pre-edge intensity in the corresponding Fe K-edge spectrum (Figure 2.4b) as addition of large O^{2-} anions would expand the unit cell and increase the number of octahedrally coordinated Fe centres.

As the Mo concentration was further increased to x = 0.65 ($Sr_2Fe_{1.35}Mo_{0.65}O_6$), the lattice parameter was calculated to be significantly larger than that of $Sr_2Fe_{1.50}Mo_{0.50}O_6$ (Figure 2.3), and a large increase in the amount of Fe^{2+} and Mo^{5+} was observed in these materials, as shown by the changes in the Fe K-edge (Figure 2.4; Section 2.3.2) and Mo K-edge spectra (Figure 2.5a; Section 2.3.3). Here, it is proposed that between x = 0.50 and x = 0.65, a critical concentration of Mo is reached which allows for a reduction of both Fe and Mo without creating a destabilizing amount of O vacancies, as the oxidation state of Mo is always greater than that of Fe. The large shift in the lattice parameter (Figure 2.3) is attributed to a change in the unit cell shape from a cubic ($Fm\bar{3}m$) structure to a tetragonal ($I4/m$) structure (Figure 1.5 on page 22) [62, 63]. As Fe^{3+}

is reduced to Fe^{2+}, there is a dramatic increase in the effective ionic radius ($r_{Fe^{2+}}$ = 0.780 Å vs. $r_{Fe^{3+}}$ = 0.645 Å) while there is only a minor difference between the effective ionic radii of Mo^{6+} and Mo^{5+} ($r_{Mo^{5+}}$ = 0.61 Å vs. $r_{Mo^{6+}}$ = 0.59 Å) [153]. Thus, the tetragonal distortion of the lattice is the result of the steric distortions necessary to incorporate a significant amount of Fe^{2+}, which occupies the larger octahedral sites in this structure [62, 160].

To determine how the ordering and O deficiency of the $Sr_2Fe_{2-x}Mo_xO_6$ materials is impacted by further heating, the as-synthesized materials were annealed in a vacuum environment. Through examination of the Fe K-edge XANES spectra, oxidation of the Fe cations was observed to occur upon annealing the as-synthesized materials under vacuum. While oxidation of the Fe site results in a decrease of the average Fe radius and would be expected to decrease ordering based on the discussion above, analysis of the powder XRD patterns showed that the ordering of the Fe and Mo sites increased in Sr_2FeMoO_6 (Figure 2.3;section 2.3.1). This may be explained by the increased temperature used to anneal these samples (the samples were reduced at 900 °C (as synthesized) and annealed at 1050 °C), which apparently leads to increased ordering. Thus, these results serve to further confirm the dependence of the degree of ordering in $Sr_2Fe_{2-x}Mo_xO_6$ materials on temperature, as has been found in previous studies [74, 83]. These results also suggest that the oxidation state of Fe found in Mo-rich $Sr_2Fe_{2-x}Mo_xO_6$ materials (those with $x \geq 0.65$) is highly sensitive to the atmosphere in which the materials are synthesized, consistent with studies of the related $SrMoO_3$ perovskite phase [180, 181].

2.5 Conclusions

A series of $Sr_2Fe_{2-x}Mo_xO_6$ compounds were synthesized and studied by powder XRD and XANES to determine how the oxidation state of Fe and Mo depends on the Mo concentration. The powder X-ray diffraction patterns indicated that a large variation in the lattice parameter of these compounds occurred between the compounds with $x \leq 0.50$ and $x \geq 0.65$. This is in agreement with previous studies in which a transition from a cubic to tetragonal unit cell was reported [62,63,160].

Accompanying this change in structure is a partial reduction of the Fe oxidation state from Fe^{3+} to a mixture of Fe^{2+} and Fe^{3+} and a partial reduction of the Mo^{6+} oxidation state to a mixture of Mo^{5+} and Mo^{6+} (minor amounts of Mo^{4+} may also be present). Here, changes in the oxidation states of Fe and Mo have been spectroscopically shown to occur with changing Mo-content. Further, the results in this study indicate that the change in oxidation state of Fe from Fe^{3+} to $Fe^{2+/3+}$ is the driving factor in the transformation of the cubic lattice to a tetragonal lattice, and that the reduction of Fe is possible only after a critical concentration of Mo has been reached. The Fe K-edge XANES spectra also indicated that a significant amount of O vacancies exist in all of the materials studied. Upon annealing under a vacuum environment, $Fe^{2+/3+}$ was oxidized to Fe^{3+} and the oxygen deficiency of these systems was significantly reduced. While O vacancies are already known to occur in these systems, using XANES, this study has shown that the amount of O deficiency is dependent on the amount of $O_{2(g)}$ present in the atmosphere in which these materials are reacted. The results reported here show that the composition strongly impacts the oxidation states of Fe and Mo in $Sr_2Fe_{2-x}Mo_xO_6$ materials, which are linked to structural changes within this system, and the dependence on both composition and preparation method likely accounts for the wide range of oxidation states and magnetic properties that have been reported previously.

Chapter 3

AN INVESTIGATION OF THE ELECTRONIC STRUCTURE OF $Cu_2FeSn_{3-x}Ti_xS_8$ ($0 \leq x \leq 3$) THIOSPINEL SPIN-CROSSOVER MATERIALS USING X-RAY ABSORPTION SPECTROSCOPY[1]

3.1 Introduction

The spin-crossover (SCO) transition is a magnetic phenomenon in which a transition-metal undergoes a transition from a low-spin state (LS; e.g., $t_{2g}^6 e_g^{*0}$ for a d^6 center) to a high-spin state (HS; e.g., $t_{2g}4e_g^{*2}$) [113–115]. The SCO systems have been the subject of a large number of studies and the SCO transition has been found to be induced by a wide variety of perturbations including irradiation with UV light, changes in pressure, changes in atmosphere, and changes in temperature [118–122]. In addition to the intrinsic value of studying this interesting process, transition-metal complexes exhibiting a SCO transition have been widely studied due to their potential use in a variety of applications, including: sensors, molecular switches, displays, and memory storage devices [123, 124].

It has recently been reported that the $Cu_2FeSn_{3-x}Ti_xS_8$ thiospinels contain an easily accessible SCO transition (from LS to HS with increasing temperature) with a transition temperature of $\sim$215 K [98]. (A full discussion of the SCO phenomenon is found in Section 1.3 on page 25.) Single

[1] A version of this paper has been published. Copyright is owned by Elsevier B.V. Reprinted with permission from J.R. Hayes and A.P. Grosvenor, *Journal of Solid State Chemistry*, (2012) Accepted. DOI: 10.1016/j.jssc.2012.08.057.

crystal studies of the $Cu_2FeSn_3S_8$ end-member (rhodostannite) have shown that the unit cell is distorted from the cubic spinel structure, and is best described as a tetragonal crystal lattice [108,182]. However, this distortion is small, and the $Cu_2FeSn_{3-x}Ti_xS_8$ materials can generally be considered to adopt the cubic spinel structure, as shown in Figure 1.6 [92, 108–110, 183]. Here, Cu occupies a tetrahedral structure while the Fe, Sn, and Ti are randomly distributed in an octahedral site (see Section 1.3 on page 25). In this structure, only the Fe^{2+} metal center may contain unpaired electrons, and it can alternate between a diamagnetic LS electron configuration and a magnetic HS electron configuration.

The $Cu_2FeSn_{3-x}Ti_xS_8$ thiospinels appear to present an excellent opportunity to study the SCO transition in crystalline materials using XANES. While XANES has been employed to study the SCO transitions in oxide-based materials, no temperature-dependent XANES study of the SCO transition in chalcogenide-based materials is known [4, 127, 128]. To this end, Fe K-edge XANES spectra were collected from a series of $Cu_2FeSn_{3-x}Ti_xS_8$ thiospinels at different temperatures and are reported here. Surprisingly, no changes in the Fe K-edge pre-edge region were observed as the temperature was varied, though large changes in the main-edge region were observed. Ti K- and S K-edge XANES spectra have also been collected and interpreted with the aid of electronic structure calculations to better understand these changes, and how the electronic structure of the thiospinels system changes with varying Ti content. The results reported in this study suggest that the use of Fe K-edge XANES is not appropriate to quantitatively study the SCO transition in these chalcogenide-based materials; however, significant changes in the electronic structure and covalency of $Cu_2FeSn_{3-x}Ti_xS_8$ as Ti is substituted for Sn were observed as Ti is substituted for Sn, and these changes will be the focus of this chapter.

In Chapter 2, the effects of simultaneous changes in coordination number and oxidation state on the pre-edge were investigated. In this chapter, the effects of changes in d-state occupancy, caused by an SCO transition, will be investigated. Further, this chapter will explore the relationship between the degree of covalency in the M–S bonds and the intensity of the pre-edge. In this regard, it was found that changes in the crystal structure can have marked effects on the electronic structure,

especially in highly covalent systems such as the $Cu_2FeSn_{3-x}Ti_xS_8$ system studied here.

3.2 Experimental

3.2.1 Synthesis

A series of $Cu_2FeSn_{3-x}Ti_xS_8$ (x = 0, 1, 1.5, 2, 3) thiospinels were synthesized from elemental precursors via a standard solid-state reaction route [98, 108, 109]. Stoichiometric amounts of Cu (Alfa Aesar, 99.5%), Fe (Alfa Aesar, 99.9%), Sn (Alfa Aesar, 99.85%), Ti (Alfa Aesar, 99%), and S (Alfa Aesar, 99.5%) were mixed and sealed in evacuated fused-silica ampules. The ampules were heated at 573 K for 1 day after which the temperature was elevated to 1023 K. The samples were held at this temperature for 6 days and then quench cooled in air. (Other cooling methods, like slow cooling and quench cooling in ice water were tried, but air quenching resulted in the highest purity materials.) The ampules containing the thiospinels were opened and ground in air, and the black powders were stored in a N_2-filled glovebox. The chemical formulas presented in this study are based on the stoichiometry of the elements used during the reaction.

A series of standards were either synthesized or purchased to aid in the interpretation of the XANES spectra from $Cu_2FeSn_{3-x}Ti_xS_8$. Cu_2FeSnS_4 was synthesized using conditions identical to those described above [95]. TiS_2 and FeS were synthesized by mixing stoichiometric amounts of the elements, sealing them in evacuated fused-silica ampules, and heating them at 1223 K for 15 days before cooling them to room temperature over 4 h. The ampules were opened and ground in air, and the powders were stored in a N_2-filled glovebox. A natural pyrite (FeS_2) sample was purchased from Alfa Aesar.

The phase purity of all of the materials studied was checked by powder X-ray diffraction (XRD) using a PANalytical Empyrean X-ray diffractometer equipped with a Co $K_{\alpha 1,2}$ X-ray source. The powder XRD patterns (Figure 3.1) showed that phase pure $Cu_2FeSn_{3-x}Ti_xS_8$ materials (or near-phase pure materials; $\geq 93\%$) were successfully synthesized [99, 110, 184–186]. Small amounts of a Cu_2FeSnS_4 impurity were present in the $Cu_2FeSn_2TiS_8$, $Cu_2FeSn_{1.5}Ti_{1.5}S_8$, and $Cu_2FeSnTi_2S_8$

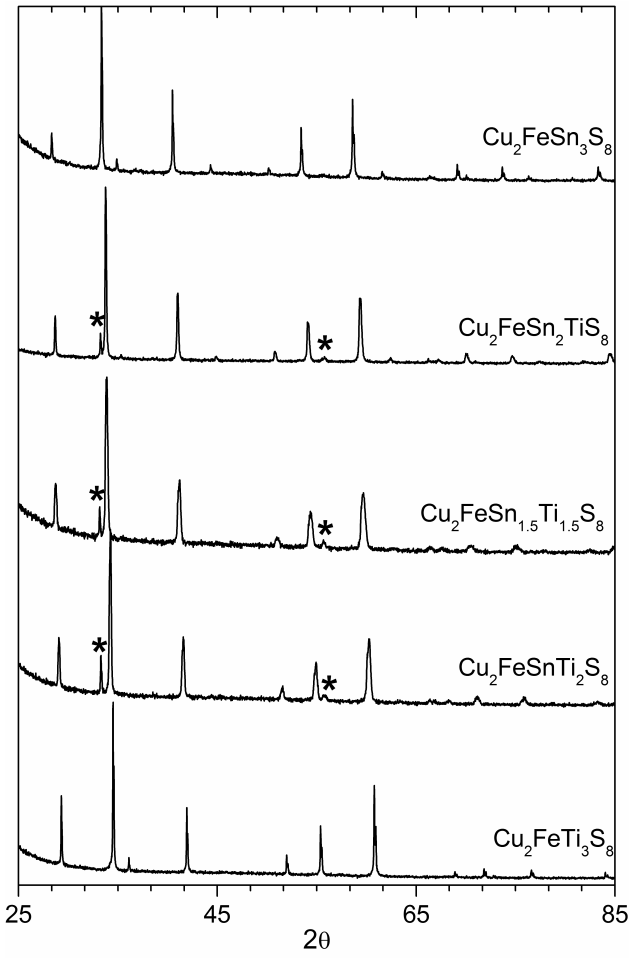

Figure 3.1: Powder XRD patterns from the $Cu_2FeSn_{3-x}Ti_xS_8$ samples are shown. As Sn is replaced by Ti, the size of the unit cell shrinks, as indicated by the shift of the diffraction peaks to higher angle. A Cu_2FeSnS_4 impurity phase was observed in some of the $Cu_2FeSn_{3-x}Ti_xS_8$ samples, as indicated by the peaks with an *.

samples, but in concentrations too low to significantly impact the XANES spectra.

3.2.2 XANES Measurements

Room-temperature Fe K-edge XANES spectra were collected using the Hard X-ray Micro Analysis (HXMA, 06ID-1) beamline at the Canadian Light Source (CLS). The flux is $\sim$6 x 10^{11} photons/s, and the maximum achievable resolution is better than 1 eV at photon energies below 10 keV using a Si (111) monochromator. Samples were finely ground and mounted on Kapton tape, which was then folded multiple times. Spectra were collected using a 0.15 eV step through the absorption edge. Samples were mounted at a $\sim$45° angle to the incident beam allowing simultaneous collection of both transmission and partial fluorescence yield-mode spectra. Transmission data was collected using ionization chambers filled with $N_{2(g)}$ and fluorescence data was collected using a 32-element Canberra Ge detector. Spectra were calibrated using the Fe K-edge spectra from an Fe metal reference foil collected in-line with the sample, which has a known absorption-edge energy of 7112 eV [9].

Room temperature Ti K-edge XANES spectra, and temperature dependent Fe K-edge XANES spectra, were collected using the Pacific Northwest Consortium/X-ray Science Division Collaborative Access Team (PNC/XSD-CAT, Sector 20) bending magnet beamline (20BM) located at the Advanced Photon Source (APS), Argonne National Laboratory. A silicon (111) double crystal monochromator with harmonic rejection was used, which at 7000 eV provides a resolution of 1 eV and a photon flux of $\sim 10^{11}$ photons/s [171]. Samples were finely ground and mounted on Kapton tape, which was then folded multiple times. The samples were mounted in a cryostat which had Be windows and was equipped with a CTI-Cryogenics model 8200 compressor that recirculated $He_{(g)}$ to a CTI-Cryogenics model 22 refrigerator when collecting the Fe K-edge spectra. The sample temperature was controlled by a Neocera LTC-11 temperature controller and spectra were collected at 50 K, 100 K, 200 K, and 290 K. The samples were mounted on an acrylic sample holder in air when collecting Ti K-edge spectra at room temperature. Samples were mounted at a $\sim$45° angle to the incident beam allowing for simultaneous measurement of transmission and partial flu-

orescence yield data. The initial beam intensity was measured using an ionization chamber filled with a 5:1 He:N_2 gas mixture, and transmission spectra were measured using ionization chambers filled with $N_{2(g)}$. The Fe K-edge partial fluorescence spectra were collected using a 13-element Canberra Ge detector, and the Ti K-edge partial fluorescence spectra were collected using a single-element Vortex Ge detector. Spectra were collected using a 0.15 eV step through the absorption edge in all cases. The Fe K-edge spectra were collected from 150 eV below the edge (7112 eV) to k = 12, which is 548.6 eV above the edge. The Ti K-edge spectra were collected from 200 eV below the edge (4966 eV) to k = 12. The Fe K-edge spectra were calibrated using an Fe metal reference foil, having a known Fe K-edge absorption-edge energy of 7112 eV [9]. The Ti K-edge spectra were calibrated using a Ti metal reference foil, having a known Ti K-edge absorption-edge energy of 4966 eV [9]. The reference spectra were collected in transmission mode concurrently with the spectra from each sample studied.

S K-edge spectra were collected using the soft X-ray microcharacterization beamline (SXRMB, 06B1-1) located at the CLS. The beamline has a photon flux of >1 x 10^{11} photons/second and provides a resolution of $\sim$0.25 eV when using a Si (111) crystal monochromator at X-ray energies less than 2500 eV [187]. Samples were prepared by pressing the finely ground powders onto C tape and spectra were measured in total electron yield (TEY) mode using a 0.10 eV step through the absorption edge. The S K-edge spectra were collected from 2430 eV to 2600 eV. Spectra were calibrated by setting the peak maximum in the plot of the first derivative from the most intense (lowest energy) peak of the S K-edge spectrum of S powder to 2472 eV [9]. All spectra collected were analyzed using the Athena software program and the default algorithm in Athena was used to normalize the spectra [172]. The Fe K-edge spectra were normalized using a pre-edge range of -45 eV $\rightarrow$-13 eV and a post-edge region ranging between 85 eV $\rightarrow$525 eV. (The energy values are relative to the absorption-edge energy, E_o). The Ti K-edge spectra were normalized using a pre-edge range of -150 eV $\rightarrow$-30 eV and a post-edge region ranging between 150 eV $\rightarrow$436 eV. The S K-edge spectra were normalized using a pre-edge range of -33 eV $\rightarrow$-6 eV and a post-edge region ranging between 25 eV $\rightarrow$112 eV.

3.2.3 Electronic Structure Calculations

Electronic structure calculations were performed on $Cu_2FeSn_{3-x}Ti_xS_8$ using a self-consistent tight-binding linear muffin tin orbital model with the atomic spheres approximation (TB-LMTO-ASA) to aid in the interpretation of the XANES spectra [188]. Due to the large number of atoms in the cubic unit cell, the smaller tetragonal unit cell reported for $Cu_2FeSn_3S_8$ was used instead [107]. To approximate the random distribution of Fe, Sn and Ti atoms over a single octahedral site, a super-cell containing two units of the tetragonal unit cell joined along the *a*-axis was created, and the Sn, Ti, and Fe atoms were individually allocated into the M sites. The symmetry of this new unit cell was determined using the symmetry reduction program provided in the TB-LMTO-ASA package, and the electronic structure calculations were then performed based on this new unit cell [188]. A total of 490 k-points were used in the calculation and both the total density of states (DOS) and partial density of states for the atomic orbitals were calculated. To better understand the S K-edge spectra, crystal orbital Hamiltonian population (COHP) curves were also calculated to understand the anti-bonding interactions between the constituent elements. No magnetic interactions between atoms were considered when performing these calculations.

3.3 Results and Discussion

3.3.1 Room Temperature Fe K-edge XANES

Fe K-edge XANES spectra from several of the $Cu_2FeSn_{3-x}Ti_xS_8$ thiospinels were collected at room temperature and are presented in Figure 3.2a. Two distinct features, labeled as A_1 and A_2, are found in the pre-edge region of Figure 3.2a and are also presented in the inset of this figure. These features are attributed to quadrupolar Fe 1s $\rightarrow$ Fe 3d transitions [2, 14, 18, 20, 28]. Along with the pre-edge features, three features are found in the main edge, and are labeled as B_1, B_2, and C in Figure 3.2a. These features primarily result from transitions to bound Fe 4p states, though multi-scattering resonances (MSR, *vide infra*) may also contribute to their intensity. The analysis

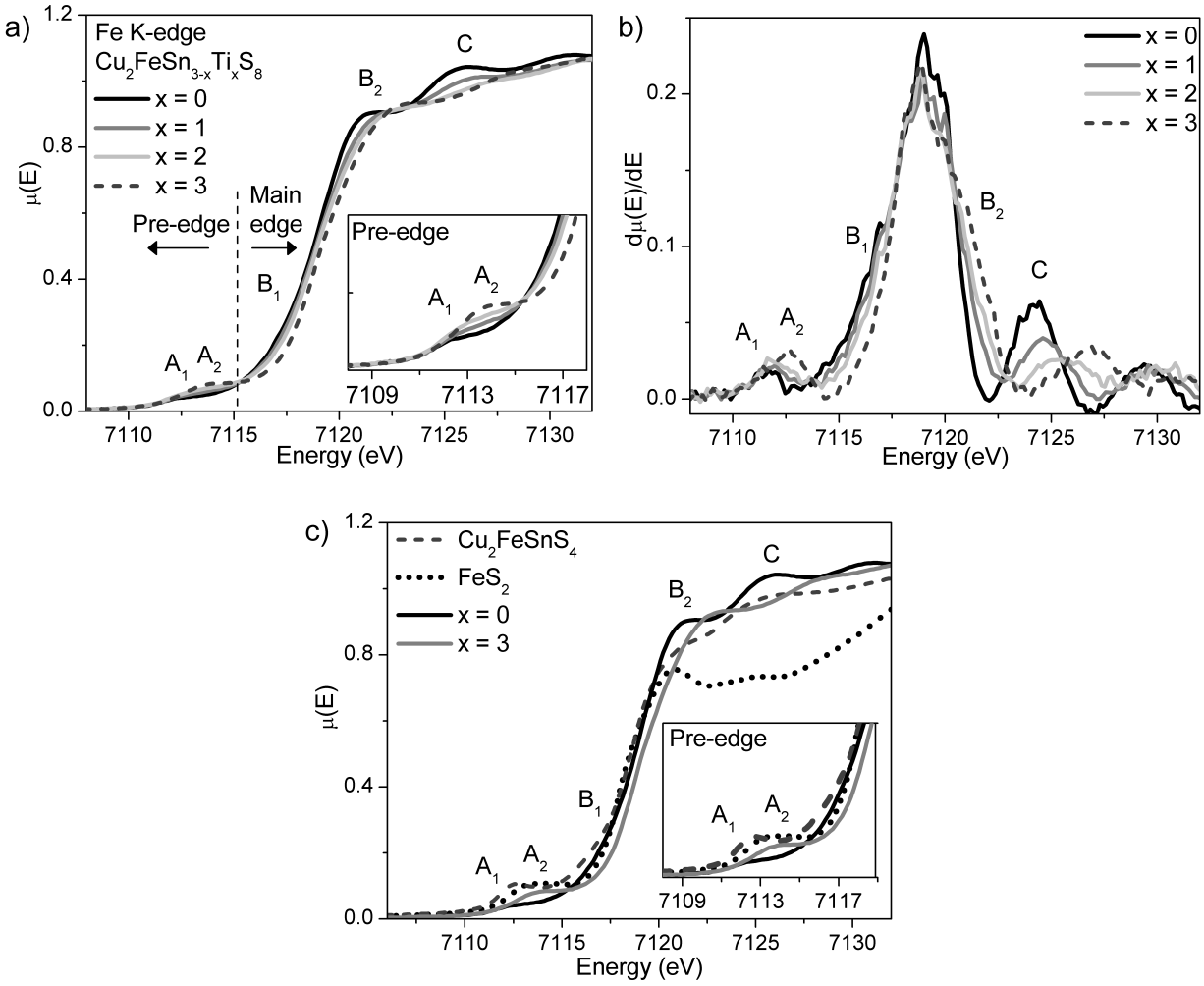

Figure 3.2: (a) Fe K-edge XANES spectra from the $Cu_2FeSn_{3-x}Ti_xS_8$ thiospinels collected at room temperature are presented. Two features, A_1 and A_2, were found in the pre-edge region while three features were found in the main edge region (B_1, B_2, and C). As the Ti content was increased, the intensity of feature B_1 decreased and the intensities of features B_2 and C increased. *Inset*: The pre-edge region is shown in an expanded view. The intensity of feature A_2 increased the most with increasing Ti content. (b) Derivative spectra of the Fe K-edge from the $Cu_2FeSn_{3-x}Ti_xS_8$ thiospinels are shown. No shift in the energy of the peak maximums associated with features A_1, A_2, B_1, or B_2 are observed with changing Ti content; however, feature C is observed to shift by 2.6 eV to higher energy across the series. As the Ti content increases, the intensity of the derivative peak of feature B_1 decreases while the intensity of the derivative peak from feature B_2 increases. (c) The Fe K-edge spectra (collected at room temperature) from Cu_2FeSnS_4 and FeS_2 are plotted along with the Fe K-edge spectra from $Cu_2FeSn_3S_8$ and $Cu_2FeTi_3S_8$. *Inset*: An expanded view of the pre-edge region from these spectra is shown.

of the main-edge features was aided by examination of the first derivatives of the Fe K-edge spectra (Figure 3.2b), which were used to analyze and quantify the shifts in the edge energy. Fe K-edge spectra from FeS_2 and Cu_2FeSnS_4 were collected to aid in the interpretation of these spectra, and are presented in Figure 3.2c.

Both pre-edge features (A_1 and A_2) were found to increase in intensity as the Ti content was increased (Figure 3.2a); however, the increase in the intensity of feature A_1 was small while the increase in the intensity of feature A_2 was relatively large. (The intensity of feature A_1 increased by less than 20% while the intensity of feature A_2 increased by $\sim$60%.) Based on examination of Fe K-edge spectra from oxide-based materials, and the octahedral coordination geometry of Fe^{2+} in the spinel structure, feature A_1 is attributed to Fe 1s $\rightarrow$ 3d t_{2g} excitations and feature A_2 is assigned to 1s $\rightarrow$ Fe 3d e_g^* excitations [2, 14, 18, 20, 28]. The intensity of the pre-edge is linked to the coordination environment of the excited metal center, and a reduced coordination number (or distortion from octahedral symmetry) can increase the intensity of the pre-edge [2, 14, 18, 20, 28]. As the coordination number decreases, the Fe 3d states can mix with local Fe 4p states, which results in a excitation with greater dipolar character leading to an increase in the pre-edge intensity [2, 14, 18, 20, 28]. In Cu_2FeSnS_4, Fe^{2+} occupies a tetrahedral site and in FeS_2, the low-spin Fe^{2+} occupies a highly distorted octahedral site [184, 186]. (In both materials, the Fe–S bond distances that are shorter than those found in the $Cu_2FeSn_{3-x}Ti_xS_8$ materials.) These large deviations from octahedral symmetry cause the pre-edge features from Cu_2FeSnS_4 and FeS_2 to be found at slightly lower energies and have higher intensities then for the $Cu_2FeSn_{3-x}Ti_xS_8$ compounds (cf. Figure 3.2c). Based on this comparison, it can be concluded that the changes in intensities of the pre-edge features in the Fe K-edge spectra from the $Cu_2FeSn_{3-x}Ti_xS_8$ samples (Figure 3.2a) are not related to changes in coordination environment, as the octahedral coordination environment of Fe^{2+} in $Cu_2FeSn_{3-x}Ti_xS_8$ does not become significantly distorted with substitution [108].

Instead of changes in coordination, the increased intensity of features A_1 and A_2 are attributed to the decrease in the Fe–S bond distance that occurs with increased Ti content [107, 108, 110]. The

reduced Fe–S bond length allows for better overlap between the Fe 3d and S 3p states, increasing the dipolar character of the pre-edge excitations, which results in the increased intensity of these features. The difference in the magnitude of the changes between feature A_1 and A_2 may be attributed to the different orientations of the Fe 3d t_{2g} and Fe 3d e_g^* orbitals. The Fe 3d t_{2g} orbitals are non-bonding in a perfectly octahedral coordination environment, and, as such, do not interact with the S 3p orbitals. However, the octahedra are slightly distorted from perfect O_h symmetry in the $Cu_2FeSn_{3-x}Ti_xS_8$ system, which allows for weak interactions between the Fe 3d t_{2g} and S 3p orbitals, though changes in these interactions with varying Fe–S bond length are expected to be slight [107, 108, 110]. In contrast, the anti-bonding e_g^* orbitals are aligned head-on with the S 3p orbitals (Feature A_2), and dipolar contributions are expected to be greatly enhanced as the overlap between the Fe e_g^* and S 3p orbitals increases with decreasing Fe–S distance. This explanation of the increase in pre-edge intensity is further supported by previous studies of Fe-containing chalcogenides, where similar changes in the Fe K-edge pre-edge structure have been observed with decreasing Fe–X distances (X = S, Se, Te) [189–191].

The main-edge region of the Fe K-edge XANES spectra from the $Cu_2FeSn_{3-x}Ti_xS_8$ materials was also found to vary as the Ti content was increased. As Ti substitutes for Sn, the main-edge energy shifts to higher energy. An analysis of the first derivative of the spectra (Figure 3.2b) indicates that this apparent shift may be due to changes in intensity, as the energy of the most intense first derivative peak, which results from a excitation of 1s electrons to 4p states on the absorbing atom, was found to consistently have an energy of $\sim$7118.2 eV regardless of the value of x in the chemical formula. The plot of the first derivative of the spectra also provides an interesting view of the changes in features B_1 and B_2 in Figure 3.2a. In the plot of the first derivative of the spectrum from $Cu_2FeSn_3S_8$ (Figure 3.2b), the main peak was asymmetric, with a low-energy shoulder. As the Ti content increased, the derivative peak initially broadened, becoming more symmetric. When the Ti content was further increased, the derivative peak again became asymmetric, with a shoulder at higher energy being observed. This pattern indicates that the changes observed in the main-edge region of the spectra presented in Figure 3.2a are likely a result of a decrease in the

intensity of feature B_1, and an increase in the intensity of feature B_2. Plots of the partial DOS (Figure 3.3a-c) showed overlapping regions of Sn 5p, S 3p and Fe 4p density between 4-7 eV above the Fermi edge. As a reference, a high density of Fe 3d states was found between $\sim$0-2 eV above the Fermi-edge (Figure 3.4), corresponding to feature A_1 in the Fe K-edge spectra presented in Figure 3.2a. Feature A_1 and feature B_1 in the Fe K-edge spectra (Figure 3.2a) are separated by $\sim$5 eV, matching the separation between the Fe 3d states and the Sn 5p, S 3p, and Fe 4p states in the plots of the partial DOS. Further, the calculated crystal orbital Hamiltonian populations (COHP) curves (Figure 3.4b,d,f) indicated the presence of strong Fe–S and Sn–S anti-bonding interactions in this energy range. Based on the electronic structure calculations (Figures 3.3 and 3.4), and the energy at which the feature is found, feature B_1 is attributed to the excitation of 1s electrons to hybridized Fe 4p–S 3p–Sn 5p states [2].

If B_1 is assigned to a transition of 1s electrons to Fe 4s–S 3p–Sn 5p states, then the observed decrease in intensity of this feature with the substitution of Ti for Sn may be easily explained: decreasing the number of Sn atoms reduces the number of Fe–S–Sn interactions, which decreases the intensity of this feature. The concurrent increase in the intensity of feature B_2 is also related to the changing number of Fe–S–Sn interactions. As the number of hybridized Fe–S–Sn states decreases, the Fe 4p states that were involved in these hybridized states become available for other interactions. The resulting excess Fe 4p density likely shifts to higher energy, leading to the observed increase in intensity of feature B_2. The COHP curves (Figure 3.4b,d,f), show increased Fe–S and Ti–S interactions 8-11 eV above the Fermi edge, and based on comparison with these curves, it is possible that feature B_2 in the Fe K-edge spectra presented in Figure 3.2a arises from the excitation of 1s electrons to Fe 4p states interacting with Ti 4p states through S 3p states (Fe 4p–S 3p–Ti 4p). (Interactions between neighboring Fe atoms are also possible; i.e., Fe 4p–S 3p–Fe 4p.) Thus, the intensity of this feature would be expected to increase as the Ti content is increased owing to the larger number of possible hybridized Fe 4p–S 3p–Ti 4p states available for 1s electrons to be excited to. This assignment is further supported by examination of the Ti K-edge spectra, which are discussed in Section 3.3.3.

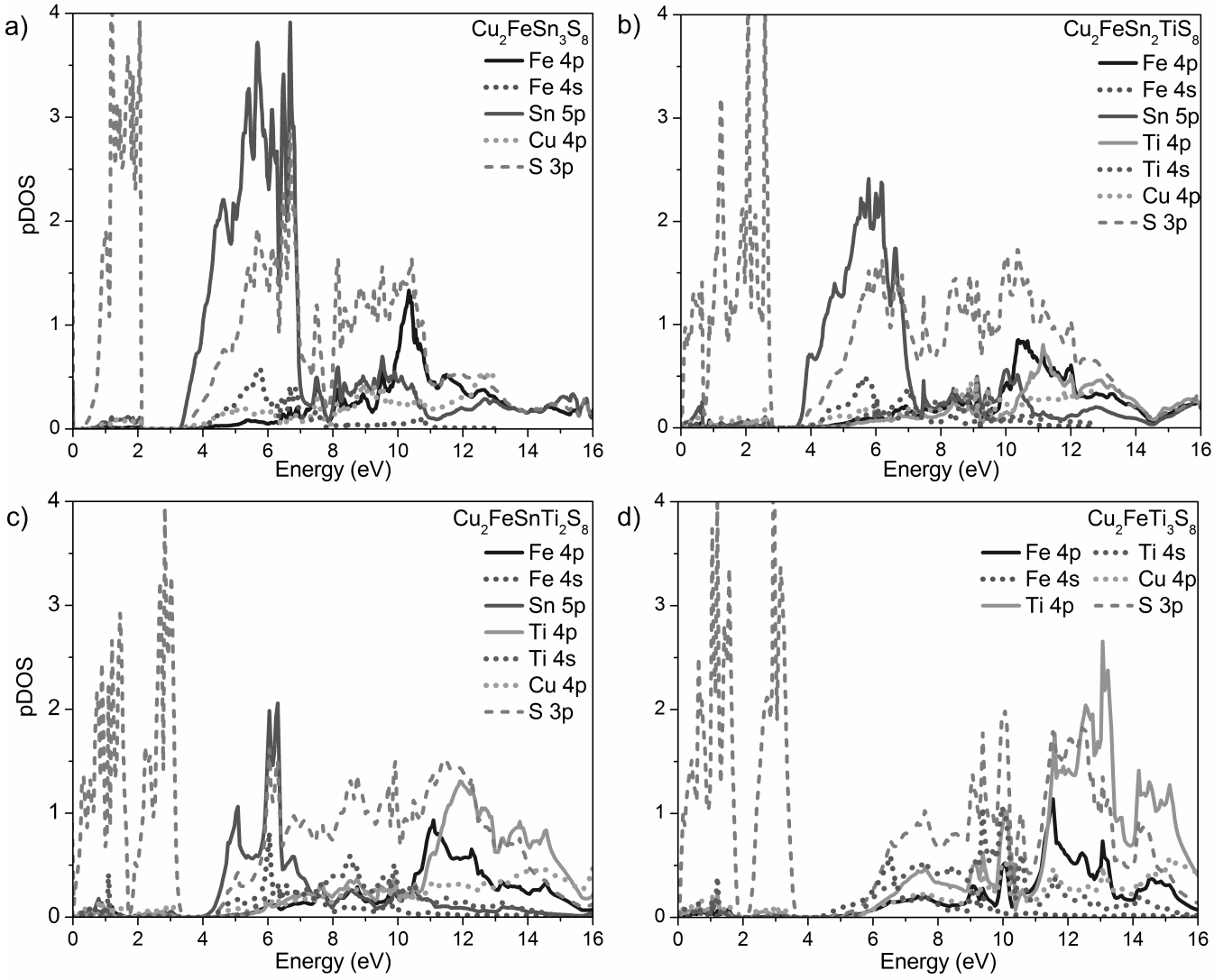

Figure 3.3: The Fe 4p, Sn 5p, and S 3p partial DOS are presented for (a) $Cu_2FeSn_3S_8$, (b) $Cu_2FeSn_2TiS_8$, (c) $Cu_2FeSnTi_2S_8$, and (d) $Cu_2FeTi_3S_8$ relative to the Fermi level (0 eV). The density of the Sn 5p and S 3p states was large between 4 eV and 7 eV. The the Sn 5p density in this region (4-7 eV) decreased with increasing Ti content, mirroring the changes in the B_1 and E_1 features in the Fe K- and Ti K-edge XANES spectra, respectively (Figures 3.2a and 3.6a).

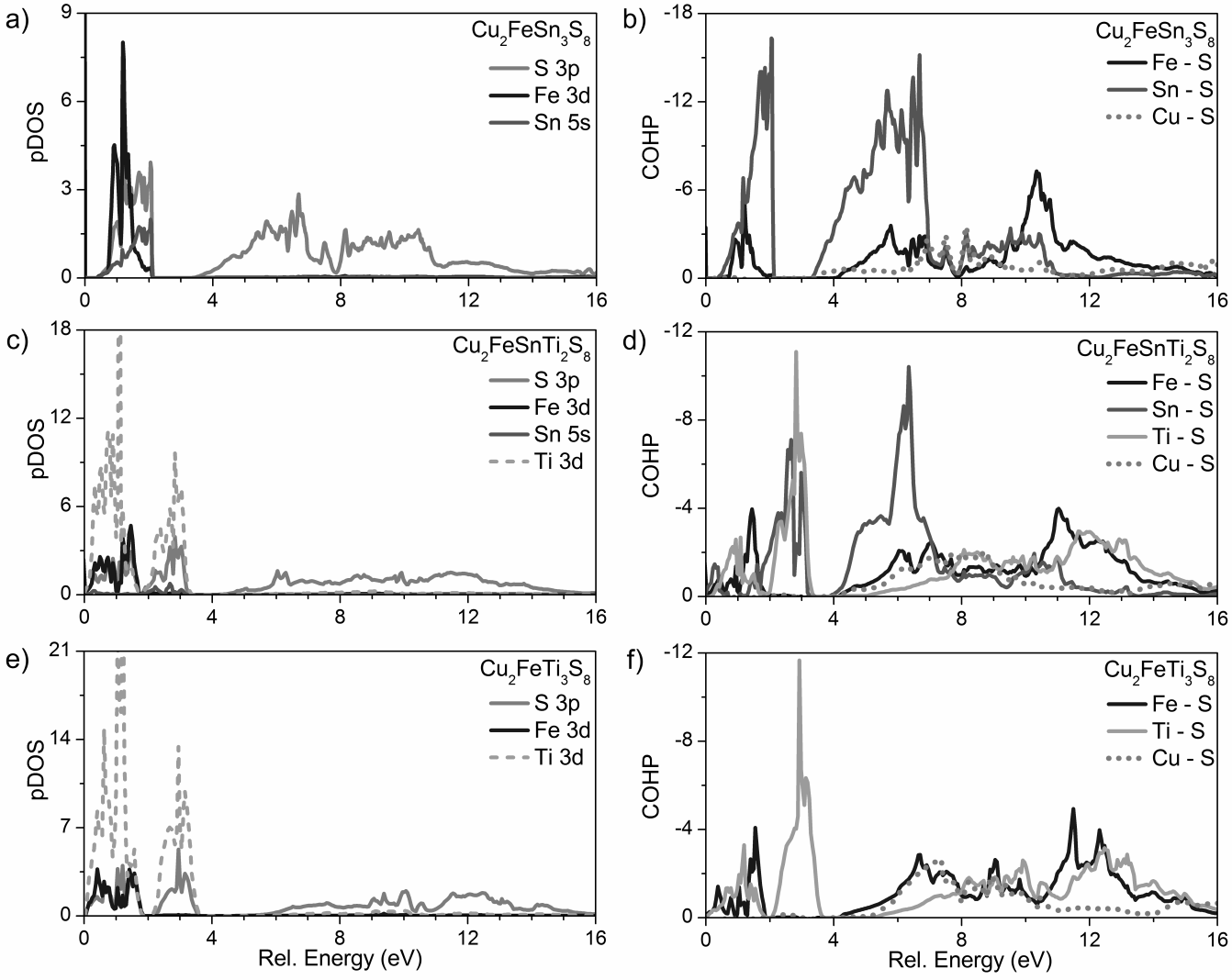

Figure 3.4: The S 3p, Fe 3d, Sn 5s, and Ti 3d partial DOS are plotted for (a) $Cu_2FeSn_3S_8$, (c) $Cu_2FeSnTi_2S_8$, and (e) $Cu_2FeTi_3S_8$ relative to the Fermi level (0 eV). The crystal orbital Hamiltonian population (COHP) curves are plotted for (b) $Cu_2FeSn_3FeS_8$, (d) $Cu_2FeSnTi_2S_8$, (f) $Cu_2FeTi_3S_8$ relative to the Fermi level, and show the anti-bonding interactions present in these materials.

The final feature labeled in Figure 3.2a (C) was found at ∼7126 eV in the spectrum from $Cu_2FeSn_3S_8$, and was observed to decrease in intensity and shift to higher energy ($\Delta E \sim 2.4$ eV) with greater Ti incorporation. These changes are largely attributed to changes in the multi-scattering resonances (MSR) that occur when the core electron is excited out of the atom. This photoelectron can scatter off of multiple neighboring atoms, resulting in constructive and destructive interference patterns, which increases or decreases the probability of photon absorption, respectively [6, 7]. The probability that the photoelectron will interact with a neighboring atom (the backscattering power of the neighboring metal center) is directly related to the number of electrons around the scatterer [6, 7]. As Ti is substituted for Sn, the average backscattering power of the neighboring metal atom decreases, resulting in the decreased intensity of feature C. Changes in the MSR contribution may also be responsible for the observed shift of feature C to higher energy. The energy at which a MSR is found is inversely proportional to the scattering path length [192]. As the Fe–S bond length decreases, the scattering path length of the photoelectron also decreases, resulting in a shift of feature C to higher energy.

3.3.2 Temperature-dependent Fe K-edge XANES

After developing an understanding of how the Fe K-edge spectra change with composition, the effect of a change in the average Fe^{2+} spin state on the spectra was studied by collecting spectra from several of the $Cu_2FeSn_{3-x}Ti_xS_8$ thiospinels at 50 K, 100 K, 200 K, and 290 K (Figure 3.5). As the temperature is decreased, it has been shown that Fe^{2+} will undergo a SCO transition in these materials from a HS state to a LS state [98]. The SCO transition temperature was determined to be 215 K based on magnetic measurements and Mössbauer spectroscopy [98]. Surprisingly, little change in the pre-edge region of the Fe K-edge XANES spectra was observed with varying temperature, and only changes in the main-edge region of the spectra were observed.

In the pre-edge region of the Fe K-edge XANES spectra, the intensities of features A_1 and A_2, which arise from excitations of 1s electrons to Fe 3d t_{2g} and 3d e_g^* states, respectively (see Section 3.3.1), were observed to change only very slightly with decreasing temperature (insets of

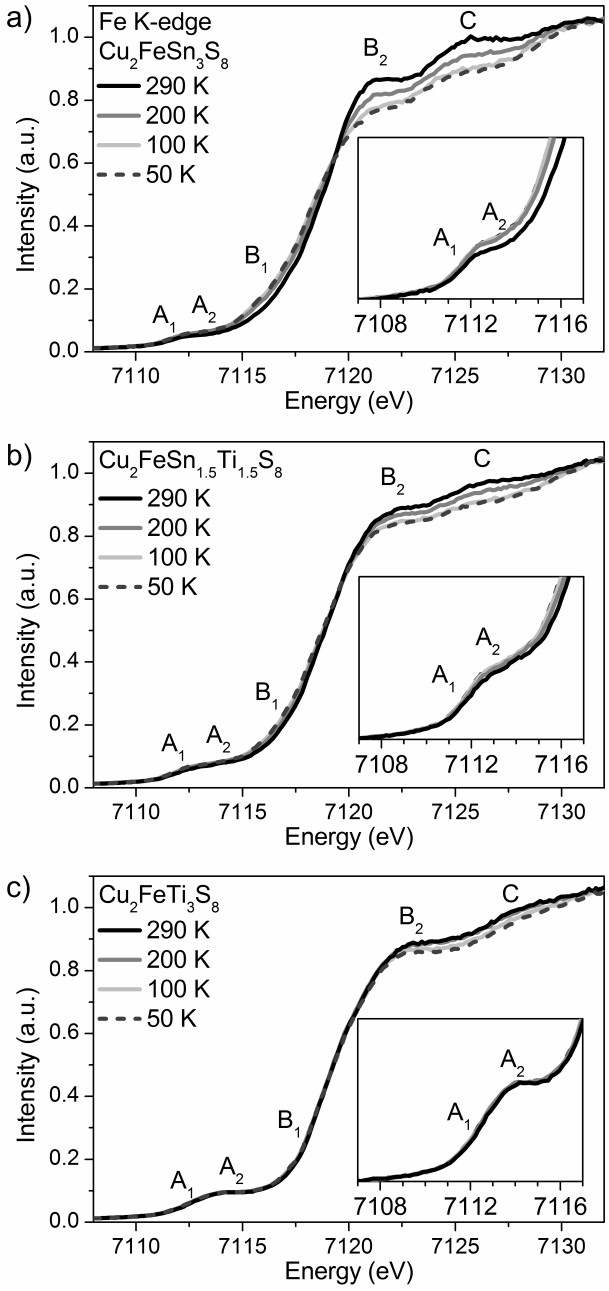

Figure 3.5: Fe K-edge spectra collected at 50 K, 100 K, 200 K, and 290 K from (a) $Cu_2FeSn_3S_8$, (b) $Cu_2FeSn_{1.5}Ti_{1.5}S_8$, and (c) $Cu_2FeTi_3S_8$ are presented. The insets of each show an expanded view of the pre-edge region. As the temperature was decreased from 290 K to 100 K, the intensity of features B_1, B_2, and C decreased in the Sn-containing samples. In $Cu_2FeTi_3S_8$, only features B_2 and C were observed, and both decreased with decreasing temperature. Very little change in the spectra was observed when the temperature was decreased from 100 K to 50 K. As the Ti-content was increased, the changes in the spectra with decreasing temperature were found to become more subtle.

Figure 3.5). While it is possible that this change is a result of the SCO transition, it is more probable that it is a result of the increasing intensity of feature B_1 in the main-edge region of the spectra (*vide infra*). It was expected that the intensity of the pre-edge features would change much more with temperature because the SCO transition involves changing the distribution of electrons in the Fe 3d states from $t_{2g}^4 e_g^{*2}$ (HS state) to $t_{2g}^6 e^{*0}$ (LS state), thus shifting the energy distribution of unoccupied states; however, this was not the case. Previous studies of oxides that undergo a SCO transition (e.g. $LaCoO_3$, $La_{1-x}Sr_xCoO_3$, and $La_{1-x}Sr_xFeO_3$) have shown changes in the pre-edge region of Co and Fe K-edge XANES spectra as the temperature is varied [127, 128]. While changes in the pre-edge region of the spectra presented here were expected as the temperature was varied based on previous studies of oxide-based materials, XANES studies of molecular SCO compounds where O is not the predominate ligand coordinated to the metal center have also failed to show significant changes in the pre-edge region with changing spin state [4, 193]. If the pre-edge features in the spectra from $Cu_2FeSn_{3-x}Ti_xS_8$ were to change with temperature, it would be expected that these changes would be relatively small, as the Fe^{2+} is not 100% HS at 300 K) or 100% LS at 50 K in the $Cu_2FeSn_{3-x}Ti_xS_8$ compounds [98]. It is likely then that any changes that occurred in the pre-edge region of the spectra from the thiospinels because of the SCO transition were masked by the highly covalent nature Fe 3d–S 3p bonds.

In contrast to the pre-edge, the intensities of the features found in the main edge region of the spectra were found to be dependent on temperature (Figure 3.5). Feature B_1 was observed to increase in intensity with decreasing temperature while the intensities of features B_2 and C were observed to decrease with decreasing temperature. The magnitude of the changes observed in these features decreased with increasing Ti content (Figure 3.5). The changes observed in this study are consistent with the changes found in the main-edge region of Fe K-edge spectra from molecular spin-crossover systems, in which a decrease in the intensity of main-edge features was observed as the systems switched from a high-spin to low-spin state [4, 113, 189]. Based on this, it is likely that the changes observed in the Fe K-edge spectra from the $Cu_2FeSn_{3-x}Ti_xS_8$ compounds are associated with a change in the average spin-state of the Fe centers. Changes in the Fe spin-state

are expected to result in a redistribution of the Fe valence states, which could explain the changes in intensity of features B_1 and B_2. Changes in the distribution of Fe 4p states would be expected to be more easily observed than changes in the Fe 3d states due to the strong, dipolar nature of the Fe $1s \rightarrow 4p$ transitions observed in the main-edge, as opposed to the weak, quadrupolar Fe $1s \rightarrow 3d$ transition in the pre-edge.

The decreased magnitude of the changes observed in the Fe K-edge spectra with increasing Ti-content is likely due to the decreased number of HS Fe^{2+} centers that undergo the SCO transition as the temperature is lowered [98]. This assertion is supported by the previous study of the SCO transition in $Cu_2FeSn_{3-x}Ti_xS_8$ by using magnetic susceptibility measurements and Mössbauer spectroscopy [98]. These measurements found that the percentage of HS Fe^{2+} decreased from$\sim$70% at room temperature to $\sim$20% at 50 K when x = 0. When the Ti content was increased to x = 3, $\sim$84% of the Fe^{2+} was HS at room temperature and at 50 K the percentage of HS Fe^{2+} only decreased to $\sim$74% [98]. In this previous study, it was reported that initially, when the Ti content was increased from x = 0 to x = 1.5, the amount of Fe^{2+} in a HS state at room temperature decreased. However, when the Ti content was further increased above x = 1.5, the amount of Fe^{2+} in the HS state at room temperature increased. This increase in HS Fe^{2+} when the Ti content was greater than x = 1.5 was proposed to result from increased antiferromagnetic interactions between the Fe^{2+} ions, lowering the energy of the HS state [98]. (The Ti concentration is low enough when $x < 1$ that the Fe^{2+} centers do not interact significantly [98].) Lowering the energy of the HS state reduces the amount of thermal energy required to excite the Fe^{2+} centers into a HS state, decreasing the number of Fe^{2+} ions that transition from a HS to LS state when the temperature is lowered from 290 K to 50 K [98]. The Fe K-edge XANES results reported here cannot be used to compare the concentrations of HS and LS Fe^{2+} between compositions, but they do show that the relative concentrations of HS and LS Fe^{2+} can be determined within a given composition.

3.3.3 Ti K-edge XANES

Ti K-edge XANES spectra from the Ti-containing $Cu_2FeSn_{3-x}Ti_xS_8$ thiospinels were collected and are presented in Figure 3.6a. In general, these spectra are similar to the Fe K-edge XANES spectra presented in Figure 3.2a, though the changes observed are more subtle. Two features are found in the pre-edge region of these spectra, labeled as D_1 and D_2, and arise from Ti 1s $\rightarrow$ 3d transitions. Three main-edge features are observed in the spectra and are labeled as E_1, E_2, and F. These features are generally attributed to Ti 1s $\rightarrow$ 4p transitions, though multi-scattering effects may also contribute. The Ti K-edge spectrum from TiS_2 was collected to aid in the interpretation of these spectra, and is compared to the Ti K-edge spectrum from $Cu_2FeTi_3S_8$ in the inset of Figure 3.6a. The intensities of the pre-edge features (D_1 and D_2) in the spectra from $Cu_2FeSn_{3-x}Ti_xS_8$ increase slightly as the Ti content was increased. This change is attributed to the shortening of the Ti–S bond caused by the contraction of the unit-cell with greater Ti incorporation. The contraction allows for better overlap between the Ti 3d and S 3p states, which increases the dipolar character of the excitation.

The discrepancy between the magnitude of the changes found in the pre-edge regions of the Ti K- and Fe K-edge spectra (cf. Figures 3.2a and 3.6b) may be explained by comparing the electronegativities of Ti, Fe, Sn, and S, which are 1.32, 1.64, 1.72, and 2.44, respectively [194]. Based on these values, it is expected that the Fe–S bond would be more covalent than the Ti–S bond. Therefore, changes in the M–S bond length would influence the pre-edge intensity in the Fe K-edge spectra more than in the Ti K-edge spectra, as increased covalency entails more S 3p character in the Fe 3d–S 3p bond, resulting in a transition with greater dipolar character. Further, as Ti is substituted for Sn, the average electronegativity of the neighboring metal center (M) decreases, allowing the electron density in the Fe–S–M interaction to be shifted towards the Fe–S bond, further increasing the covalency of this bond (relative to the Ti–S bond) [195, 196].

The main-edge features (E_1, E_2, and F) in the Ti K-edge XANES spectra were also observed to change as the Ti content was varied. Feature E_1 decreased in intensity as the Ti content was increased. This feature is analogous to feature B_1 found in the Fe K-edge spectra, and is attributed

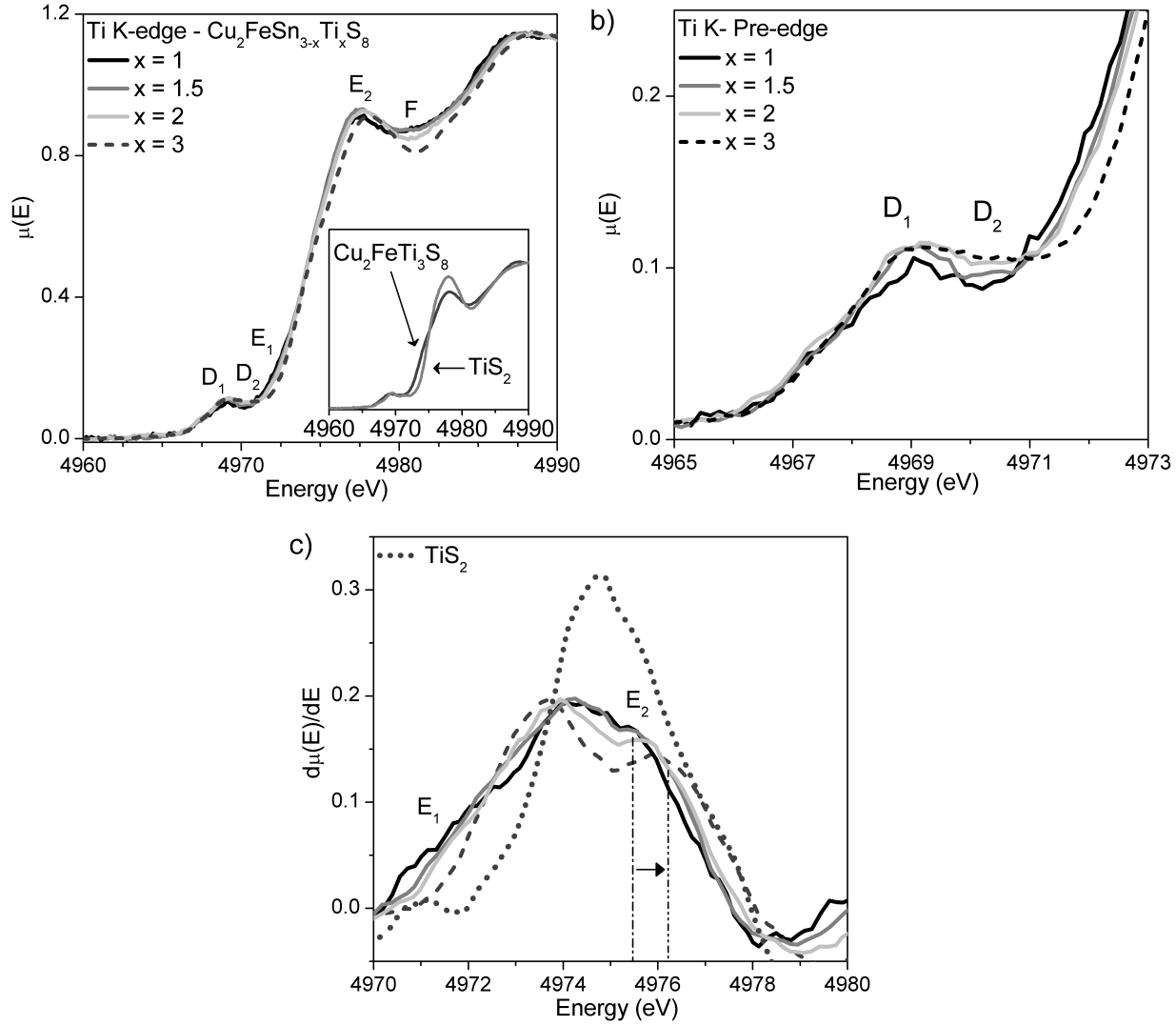

Figure 3.6: (a) Ti K-edge spectra from several $Cu_2FeSn_{3-x}Ti_xS_8$ thiospinels are shown. Features D_1 and D_2 are found in the pre-edge region while three features (E_1, E_2, and F) are found in the main edge region. Inset: The Ti K-edge spectra from $Cu_2FeTi_3S_8$ and TiS_2 are compared. (b) An expanded view of the pre-edge region of the Ti K-edge spectra shows that the intensities of both features (D_1 and D_2) increase as Ti is substituted for Sn. This trend is especially noticeable for feature D_2. (c) The main-edge region of the first derivatives of the Ti K-edge spectra is shown. The peak associated with feature E_1 shifts slightly to lower energy while feature E_2 shifts to higher energy by $\sim$1 eV with increasing Ti content as indicated by the arrow.

to excitations to Ti–S–Sn states. This conclusion is supported by plots of the partial DOS (Figure 3.3), which show Ti 4p density in the 4-7 eV energy range, where a high density of Sn 5p and S 3p states are also found. These states are $\sim$3 eV above a high-density region of Ti 3d states found at $\sim$ 0-3 eV in Figure 3.3, matching the separation between features D_1 and E_1 in the Ti K-edge spectra presented in Figure 3.6. The COHP curves (Figure 3.4) also support the assignment of feature E_1 to the excitation of 1s electrons to Ti 4p–S 3p–Sn 5p states, as they show anti-bonding Ti–S and Sn–S interactions in the 4-7 eV region as well. The origins of feature E_1 lead to a simple explanation for why the intensity decreases with increasing Ti content. As Ti replaces Sn, the average number of next-nearest-neighbor Sn atoms is reduced, decreasing the number of Ti–S–Sn interactions.

Continuing the analysis of the Ti K-edge spectra, feature E_2 was observed to shift to higher energy as the Ti content increased. This change is best observed by examining the first derivative of the spectra Figure 3.6c), where the peak maximum of feature E_2 shifts from 4975.5 eV to 4976.5 eV. Based on the Fe K-edge results, which possibly showed a Fe 4p–S 3p–Ti 4p interaction, it seems likely that a redistribution of Ti 4p states from Ti 4p–S 3p–Sn 5p like interactions to Ti 4p–S 3p–Fe 4p like interactions occurs upon substitution of Ti, shifting feature E_2 to higher energy. MSR contributions may explain the change in the intensity of feature F, which decreased in intensity and shifted to higher energy as the Ti content was increased. Similar to feature C in the Fe K-edge spectra (see Section 3.3.1 and Figure 3.2a), the average backscattering power of the neighboring atoms decreases as Ti is substituted for Sn, resulting in a lowering in intensity of the MSR contribution (Feature F). Further, as the Ti–S bond distance decreases, the path length increases, shifting the MSR feature to higher energy.

Interestingly, the changes between the Ti K-edge spectra from $Cu_2FeTi_3S_8$ and TiS_2 are similar to the changes between the Ti K-edge spectra from TiS_2 and Co_xTiS_2 reported previously [197]. The TiS_2 structure is best described as sheets of edge-sharing TiS_6 octahedra stacked along the c-axis [191, 197]. When Co is intercalated into the system, it occupies the octahedral voids between these sheets of octahedra [191, 197, 198]. The similarities between the Co_xTiS_2 spec-

tra reported previously, which have not been substantially interpreted, and the spectra from the $Cu_2FeSn_{3-x}Ti_xS_8$ materials reported here suggests that they change for similar reasons when the composition is varied.

3.3.4 S K-edge XANES

S K-edge spectra were collected from the $Cu_2FeSn_{3-x}Ti_xS_8$ materials (Figure 3.7a) to investigate how the electronic structure of these compounds was affected by changing Ti content. S adopts a charge of -2 in these compounds, resulting in a full 3p shell, and S 1s→3p excitations are therefore not expected. However, similar to O K-edge XANES spectra, interactions with orbitals on neighboring atoms create empty states with strong S 3p character, and, as such, S K-edge spectra provide information about the covalency of the M/Cu–S bonds and the distribution of anti-bonding states [199–203]. (Based on the origin of the features present, these spectra can be subdivided into pre-edge and main-edge regions similar to the Fe and Ti K-edge spectra discussed above.) To aid in the interpretation of these spectra, the S K-edge spectra from a series of reference compounds were collected and are presented in Figure 3.7b.

Three general features are observed in the spectra presented in Figure 3.7a, and are labeled as G (or G'_1 and G'_2), H, and I. $Cu_2FeSn_3S_8$ has one peak in the pre-edge region located at ∼2471.5 eV (G), and the transition that it results from can be determined by comparison to a plot of the partial DOS for this compound. The calculated partial DOS (Figure 3.4a) indicates that between 0-2 eV, a high density of both S 3p and Sn 5s states are present. This is the lowest-energy region of high S 3p density, and, as such, must be associated with feature G. The COHP curves (Figure 3.4b) indicate that strong anti-bonding interactions between Sn and S are observed in this same energy region. Thus, it is concluded that feature G in the spectrum from $Cu_2FeSn_3S_8$ arises primarily from the excitation of S 1s electrons to anti-bonding Sn 5s–S 3p states, consistent with a previous study of $Cu_2FeSn_3S_8$ [112]. This is further confirmed by the S K-edge spectrum from Cu_2FeSnS_4 (Figure 3.7b), which also shows a large, single peak at a similar energy. As the Ti content was increased in $Cu_2FeSn_{3-x}Ti_xS_8$, feature G was observed to split into two features, G'_1 and G'_1. The

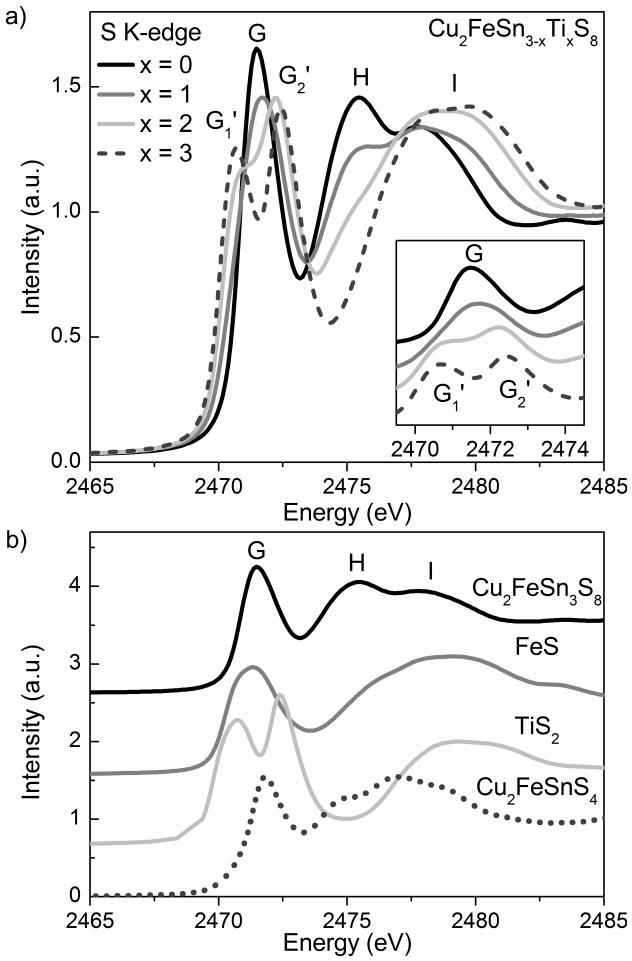

Figure 3.7: (a) S K-edge spectra from the $Cu_2FeSn_{3-x}Ti_xS_8$ thiospinels are presented. Feature G, at 2471.5 eV, was observed to split into two features, G_1' and G_2', at 2470.5 eV and 2472.5 eV with increasing Ti content. The intensity of feature H at 2475 eV was observed to decrease with increasing Ti content while feature I (2477.5 eV) broadened and shifted to higher energy. Inset: The spectra are plotted offset along the y-axis to better show the pre-edge features (G, G_1', and G_2'). (b) The S K-edge spectra from a series of S-bearing standards are presented along with the S K-edge spectra from the $Cu_2FeSn_3S_8$ sample. These spectra clearly indicate that feature G is due to Sn–S interactions, while features G_1' and G_2' are due to Ti–S interactions.

COHP curves from the Ti-containing thiospinels (Figures 3.4d and f) indicated the presence of strong Ti–S interactions near the Fermi level (0 eV). As the Ti content is increased, the Fe/Sn/Ti–S interactions split into two distinct energy regions, explaining the splitting of feature G. The nature of the Ti–S interactions may be further elucidated by examination of the plots of the partial DOS (Figures 3.4c and e), which show overlapping densities of S 3p and Ti 3d states in this energy region that increase with increasing Ti content. Based on this, and the 2 eV splitting of the G'_1 and G'_2 peaks, in good agreement with reported crystal-field splitting values of other titanium-containing compounds, feature G'_1 is assigned to S 3p–Ti 3d t_{2g} interactions and feature G'_2 is assigned to S 3p–Ti 3d e_g^* [112, 204, 205]. The S K-edge spectrum from TiS_2 serves to further confirm these conclusions, as it also exhibits two distinct peaks at 2470.7 eV and 2472.4 eV. No distinguishable features associated with S 3p–Fe 3d interactions are found in the pre-edge region of the S K-edge spectra from all of the thiospinels examined. This is attributed to both the low concentration of Fe in these systems, and the similar energy at which the Fe 3d–S 3p interactions are found compared to the Sn 5s–S 3p/Ti 3d–S 3p interactions (cf. the FeS spectrum in 3.7b).

Feature H ($\sim$2475 eV) in the spectra presented in 3.7a was observed to decrease in intensity with increasing Ti content. Comparison to the S K-edge spectra from the reference compounds presented in 3.7b shows that only the spectrum from Cu_2FeSnS_4 contained any features near 2475 eV, providing strong evidence that this feature is related to Sn–S interactions. The COHP curves (Figure 3.4) confirm this inference, as strong anti-bonding Sn–S interactions were observed between $\sim$3-7 eV above the Fermi-level. The plots of the partial DOS (Figure 3.3) show a high density of both S 3p states and Sn 5p states in this same energy region leading to the conclusion that feature H arises from excitations of 1s electrons to Sn 5p–S 3p anti-bonding states. This assignment leads to an obvious explanation of why feature H decreases with Ti content: as Ti replaces Sn, the number of Sn 5p–S 3p interactions must also decrease.

Like the change in feature H, the changes in feature I are also linked to changes in composition. Both the S K-edge spectra from Cu_2FeSnS_4 and FeS exhibit a feature in this energy region, and because of this similarity, feature I is concluded to arise from excitations to Fe 4p–S 3p and Cu

4p–S 3p interactions. The COHP curves for $Cu_2FeSn_{3-x}Ti_xS_8$ (Figure 3.4b, d, f) validate this conclusion as a region of relatively intense Fe–S and Cu–S anti-bonding interactions is found between 9-13 eV above the Fermi level. The plots of the partial DOS (Figure 3.3) also show high densities of S 3p and Fe 4p states in the same energy region, indicating that this feature arises from Fe 4p states interacting with S 3p states. As Ti was substituted for Sn in $Cu_2FeSn_{3-x}Ti_xS_8$, the intensity of feature I increased and the feature broadened and appeared to shift by $\sim$1.3 eV to higher energy (Figure 3.7a). These changes may be understood by considering a second, overlapping excitation which arises from transitions to S 3p states interacting with Ti states. Comparison to the S K-edge spectrum from TiS_2 (3.7b), which has a broad feature at 2479 eV, confirms that Ti–S interactions contribute to the intensity of feature I in the Ti-bearing $Cu_2FeSn_{3-x}Ti_xS_8$ materials. The COHP curves from $Cu_2FeSn_{3-x}Ti_xS_8$ (3.4) also showed strong, anti-bonding interactions between Ti and S in the region 12-14 eV above the Fermi level, further supporting the conclusion that excitations to Ti–S states contribute to the intensity of feature I in the S K-edge spectra from $Cu_2FeSn_{3-x}Ti_xS_8$. Based on an analysis similar to that used for feature H, the plots of the partial DOS allow the specific assignment of the Ti–S interactions to Ti 4p–S 3p anti-bonding states (Figure 3.3). This leads to the simple explanation for the correlation between Ti content and the intensity of feature I: as Ti replaces Sn, more Ti–S antibonding states are available for S 1s electrons to be excited to. Since these Ti 4p–S 3p interactions occur at higher energy compared to the Fe 4p–S 3p interactions, this results in the broadening and apparent shift of feature I to higher energy (and intensity) as the Ti content increases in $Cu_2FeSn_{3-x}Ti_xS_8$.

3.4 Conclusions

A series of $Cu_2FeSn_{3-x}Ti_xS_8$ thiospinels were synthesized and characterized using XANES and LMTO-based electronic structure calculations. It was found that the covalency of the Fe–S bond in this system was strongly influenced by the Fe–S bond distance, as evidenced by the large changes in the pre-edge region of the Fe K-edge XANES spectra. The Fe K- and Ti K-edge spectra also

showed that long-range Fe/Ti–S–Sn interactions are present, indicating that the molecular orbital approach that is typically used to understand transition-metal K-edge XANES is not appropriate for this system. Examination of S K edge spectra from the $Cu_2FeSn_{3-x}Ti_xS_8$ materials supported the interpretations of the room-temperature Fe K- and Ti K-edge XANES spectra. The $Cu_2FeSn_{3-x}Ti_xS_8$ materials were thought to provide a rare opportunity to study how the SCO transition affects the pre-edge region of the XANES spectra from crystalline materials. Surprisingly, the pre-edge features of the Fe K-edge XANES spectra showed little change as the temperature was varied. This is believed to be a result of the highly covalent nature of the system, in which S 3p character dominated the pre-edge intensity, overshadowing any changes due to the SCO transition. However, changes were observed in the main-edge region of the Fe K-edge spectra collected at different temperatures, enabling qualitative analysis of the relative change in Fe^{2+} spin-state in a given material depending on temperature. Such an analysis could be used to provide insight into how the HS/LS equilibrium varies with composition in other crystalline systems, as has been employed during the examination of Fe K-edge XANES spectra from molecular systems [4,113,189]. Finally, the XANES spectra and LMTO calculations presented in this study were able to accurately describe the electronic structure of the $Cu_2FeSn_{3-x}Ti_xS_8$ thiospinels, allowing for a better understanding of the bonding interactions present within these materials.

Chapter 4

AN X-RAY ABSORPTION SPECTROSCOPIC STUDY OF THE ELECTRONIC STRUCTURE AND BONDING OF RARE-EARTH ORTHOFERRITES[1]

4.1 Introduction

In Chapter 2, the pre-edge regions from Fe K- and Mo K-edge XANES spectra were used to investigate how the oxidation state and oxygen deficiency changed with Fe content in the $Sr_2Fe_{2-x}Mo_xO_6$ double perovskites. These investigations led to a method of how to differentiate changes in oxidation state from changes in coordination number. In Chapter 3, the effect of changes in covalency of the metal-ligand bond on the pre-edge features were investigated by studying a series of $Cu_2FeSn_{3-x}Ti_xS_8$ thiospinels. Overall, these previous chapters focused mainly on well-known, local excitations. In this chapter, a non-local pre-edge excitation, known as an intersite hybrid (see Section 1.1.1.2 on page 4) will be investigated. This feature arises from excitations to next-nearest-neighbour Fe 3d states which interact with the absorbing Fe 4p states through O 2p states. The properties of this feature are still experimentally uncertain. The effect of changes in the M–O–M' bond angle on the intensity of the intersite hybrid feature was systematically studied in this chapter by collecting the Fe K-edge XANES spectra from a series of $REFeO_3$ orthoferrites.

The rare-earth orthoferrites, having the general formula $REFeO_3$ (RE = rare-earth, Y), have

[1] A version of this paper has been published. Copyright is owned by the Interational Organizatin of Physics (IOP). Reprinted with permission from J.R. Hayes and A.P. Grosvenor, *Journal of Physics: Condensed Matter*, (2011) 23, 465502 . DOI: 10.1088/0953-8984/23/46/465502

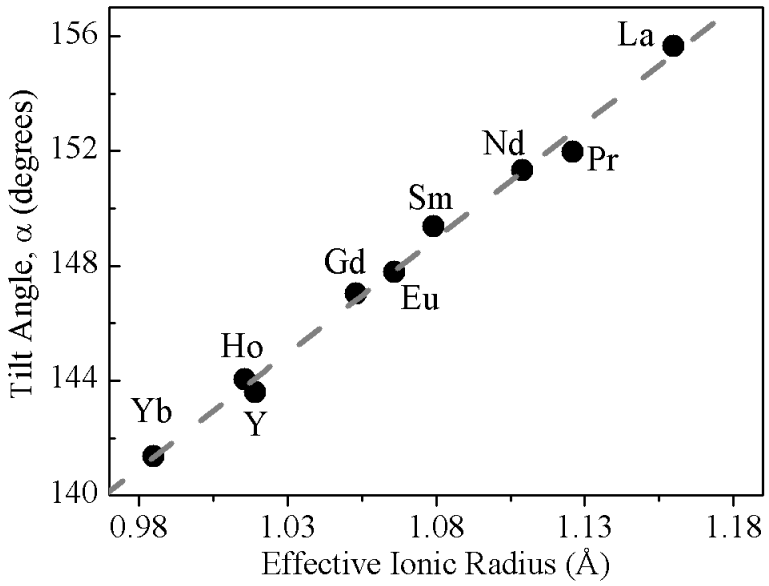

Figure 4.1: The octahedral tilt angle (α), defined as the angle between layers of FeO6 octahedra, is plotted as a function of the effect ionic radius of the RE atom [153]. As can be seen, α is directly proportional to the ionic radius of the RE.

been investigated for use in a wide variety of applications. Some of these applications include use in solid-oxide fuel cells, gas sensors, photo-catalysis, and vehicle catalytic converters [135–139]. Briefly, these oxides adopt a distorted perovskite-type structure, with space group *Pnma*, in which the rare-earth atom occupies interstitial sites between layers of corner-sharing FeO_6 octahedra (Figure 1.7 on page 31). The RE atom in this structure is surrounded by 12 O atoms, with eight of these atoms forming an inner coordination shell, while the remaining four create an outer coordination shell. Based on structural arguments, it has been proposed that only the eight inner coordination shell O atoms, which adopt a distorted square anti-prismatic coordination geometry, interact with the RE atom [143,144,146]. Because the rare-earth orthoferrites adopt an orthorhombic perovskite structure, the cation sites are highly substitutable, allowing the materials to be tuned for specific applications [48,206,207].

In the $REFeO_3$ orthoferrites, the BO_6 octahedra are tilted, resulting in a distortion from the regular perovskite structure. As the ionic radius of the rare-earth atom increases, the tilt angle between the octahedra along the c-axis (α) increases linearly (Figure 4.1) [146–154]. (A similar

trend is observed for the angle between octahedra in the a/b plane.) Based on the definition of tilt angle presented here and in Figure 1.7 on page 31, the structure becomes less distorted (compared to the ideal perovskite structure) with increasing α. This controlled and well-defined change in the Fe-O-Fe bond angle with different RE atoms provides an opportunity to perform a systematic study of the relationship between the Fe-O-Fe bond angle and the intensity of the intersite hybrid.

To investigate how the electronic structure and bonding environment in these materials change as the identity of the RE is varied, XANES has been performed. In this study, O K-, Fe L-, and Fe K-edge XANES spectra have been collected from a series of $REFeO_3$ compounds to investigate how the electronic structure and bonding environment varies depending on the identity of the RE cation. The influence of a change in bond angle between NNN Fe atoms on the intensity of the intersite hybrid peak intensity observed in the pre-edge region of the Fe K-edge spectra has also been studied, and is reported here.

4.2 Experimental

4.2.1 Synthesis

A series of $REFeO_3$ compounds (RE = La, Pr, Nd, Sm, Eu, Gd, Ho, Yb, Y) were synthesized via a solid-state synthesis route [207, 208]. Stoichiometric amounts of RE_2O_3 (Alfa Aesar REaction, $>$99.%) and Fe_2O_3 (Alfa Aesar, 99.945%) were ground, mixed, and pressed into a pellet at 6 MPa and the pellets were heated at 1473 K for 4-12 days, with intermittent grinding and re-pelleting. (The RE_2O_3 precursor was heated in air at 1073 K for 12 h prior to mixing to remove any adsorbed water.) In general, the compounds containing heavier rare-earth elements required longer heating times (e.g., $LaFeO_3$ was heated for four days while $YbFeO_3$ required 12 days of heating). Phase purity of the synthesized compounds was checked via powder X-ray diffraction (XRD) using a PANayltical Empyrean powder X-ray diffractometer using monochromatic Cu $K_{\alpha 1}$ radiation. The diffraction patterns (Figure 4.2) showed that, in all cases, the samples were either phase pure or nearly phase pure ($>$90%). In the Ho, and Yb orthoferrites, unreacted RE_2O_3 was present, and

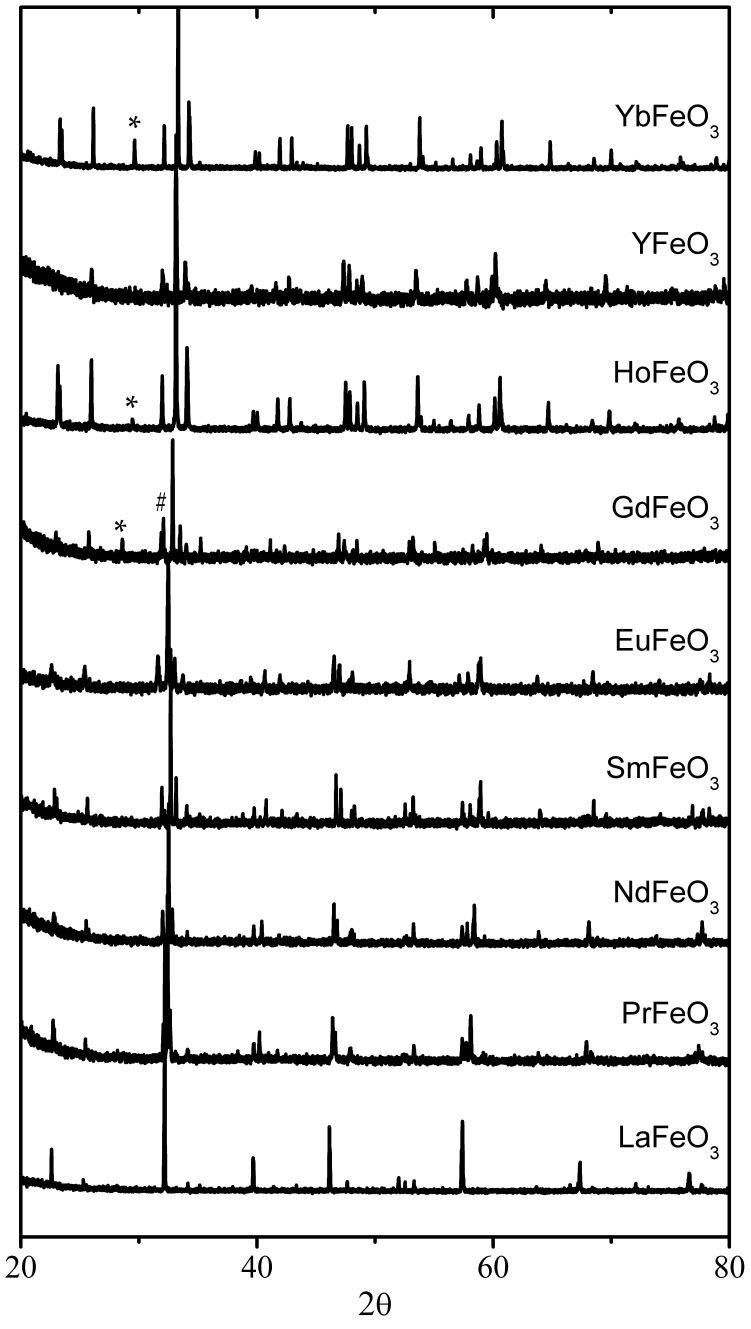

Figure 4.2: XRD diffraction patterns from the synthesized $REFeO_3$ compounds. Minor impurities were found in $GdFeO_3$, $HoFeO_3$, and $YbFeO_3$. *: RE_2O_3, #: $Gd_3Fe_5O_{12}$.

in $GdFeO_3$, a small amount of Gd and Fe containing garnet ($Gd_3Fe_5O_{12}$) was also present, but in concentrations too low to significantly impact the collected X-ray absorption spectra (<10%).

4.2.2 XANES Measurements

The Fe L- and O K-edge spectra were collected using the Spherical Grating Monochromator beamline (SGM, 11ID-1) located at the Canadian Light Source. The flux of the incident beam at 1900 eV is $\sim 10^{11}$ photons/second, and increases to $\sim$4 x 10^{12} photons/second at 250 eV. The resolution is better than 0.3 eV at excitation energies less than 1500 eV and the precision of the measured absorption energies is better than ±0.1 eV [209]. Finely ground powder samples were mounted on carbon tape and measured in either total electron yield mode (TEY, Fe L-edge) or fluorescence yield mode (FLY, O K-edge), and spectra were collected using a 0.1 eV step through the absorption edge. The Fe L-edge spectra were collected from 685 eV to 760 eV and the O K-edge spectra were collected from 498.5 eV to 600 eV. The Fe L-edge spectra were calibrated using a powdered Fe metal standard having a well-known L_3-edge energy of 706.8 eV and the O K-edge spectra were calibrated using powdered Cr metal as a standard with an L_3-edge energy of 574.1 eV [9].

Fe K-edge spectra of several $REFeO_3$ compounds (RE = La, Pr, Sm, Ho, Yb, Y) were collected using the Pacific Northwest Consortium/X-ray Science Division Collaborative Access Team (PNC/XSD-CAT, Sector 20) bending magnet beamline (20BM) located at the Advanced Photon Source (APS), Argonne National Laboratory. (It was not possible to collect spectra for $NdFeO_3$, $EuFeO_3$, or $GdFeO_3$ as the RE L-edges in these samples are too close in energy to the Fe K-edge to allow for appropriate normalization.) A silicon (111) double crystal monochromator with harmonic rejection was used, which at 7000 eV has a resolution of 1 eV and a photon flux of $\sim 10^{11}$ photons/second [171]. Samples were finely ground and sandwiched between layers of Kapton tape and the number of layers of tape was varied to maximize absorption. Samples were mounted at a $\sim$45° angle to the incident beam with transmission spectra collected using N_2-filled ion chambers and partial fluorescence yield spectra collected using a Canberra 13-element Ge detector. The Fe K-edge spectra were collected from -200 eV below the edge (7112 eV) to k = 15, which is 857.2

eV above the edge. Spectra were calibrated using an Fe reference foil, having a known Fe K-edge absorption-edge energy of 7112 eV [9]. The spectra from the reference foil were collected concurrently with the spectra from each oxide studied. All spectra collected were calibrated, normalized, and analyzed using the Athena software program [172]. The Fe K-edge spectra were normalized using a pre-edge range of -122 eV →-18 eV and a post-edge region ranging between 170 eV →725 eV (All energies are relative to the absorption-edge energy, E_o). The Fe L-edge spectra were normalized using a pre-edge range of -18 eV →-5 eV and a post-edge region ranging between 685 eV →760 eV. The O K-edge spectra were normalized using a pre-edge range of -32 eV →-6 eV and a post-edge region ranging between 18 eV →65 eV.

4.2.3 Electronic Structure Calculations

Electronic structure calculations were performed for $YFeO_3$ using a self-consistent tight-binding linear-muffin-tin orbital model with the atomic spheres approximation (TB-LMTO-ASA) to aid in the interpretation of the collected XANES spectra [188]. A total of 432 k-points were used in the calculation and the total density of states (DOS) of the system and partial DOS for Fe 4p and 3d, Y 5p and 4d, and O 2p orbitals were calculated. It was not possible to perform these calculations for the rare-earth containing compounds owing to the presence of f-orbitals which are not typically well handled by this package.

4.3 Results and Discussion

4.3.1 Fe L_3-Edge

The Fe L_3-edge spectra from some of the $REFeO_3$ samples studied along with a spectrum from Fe_2O_3 are presented in Figure 4.3. Based on dipolar selection rules, the spectral features primarily arise from Fe 2p→Fe 3d transitions. Peak A (708.6 eV) arises from transitions to non-bonding Fe 3d t_{2g} orbitals, while Peak B (710.3 eV) is assigned to transitions to anti-bonding Fe 3d e_g^*

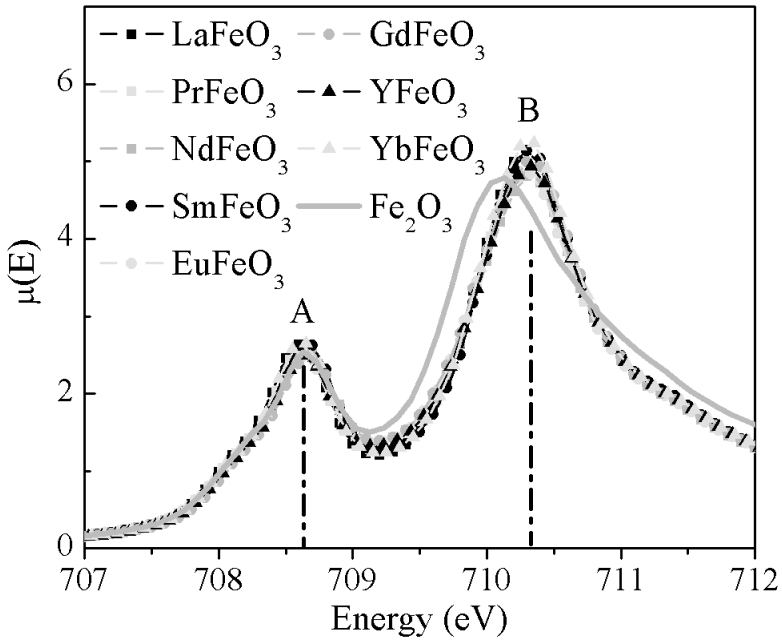

Figure 4.3: The Fe L_3-edge spectra are shown. Peak A is a result of excitations to 3d t_{2g} orbitals while Peak B results from excitations to 3d e_g^* orbitals. Peak B is narrower and shifted 0.2 eV to higher energy in the spectra from the $REFeO_3$ compounds compared to in the spectrum from Fe_2O_3 due to the less distorted FeO_6 octahedra found in the $REFeO_3$ compounds.

states [210, 211]. The intensity ratio between the two peaks is approximately 1:2 (A:B), which deviates from the expected 3:2 ratio based on orbital occupancy (assuming Fe adopts a +3 oxidation state). This deviation from the expected value is attributed to multiplet splitting effects, in which multiple final states are created when the resulting unpaired core-electron couples with the valence d-electrons (and possibly the excited electron), creating a myriad of final states [1].

The similarity in energy of peak A in all of the $REFeO_3$ compounds studied to that in Fe_2O_3 confirms that Fe adopts a 3+ oxidation state in $REFeO_3$. However, peak B is 0.2 eV lower in energy in Fe_2O_3 than is observed for the orthoferrites, which is a result of the FeO_6 octahedra being less distorted in the $REFeO_3$ materials, leading to a larger crystal field splitting energy [28, 210, 211]. The change in the line-shape of peak B, which is broader and less intense in Fe_2O_3 than in $REFeO_3$, provides further evidence that there is less distortion of the FeO_6 octahedra in the $REFeO_3$ materials. The broadening of peak B in the spectrum from Fe_2O_3 is a result of breaking the degeneracy of the e_g^* orbitals, which is consistent with a deviation from ideal O_h symmetry

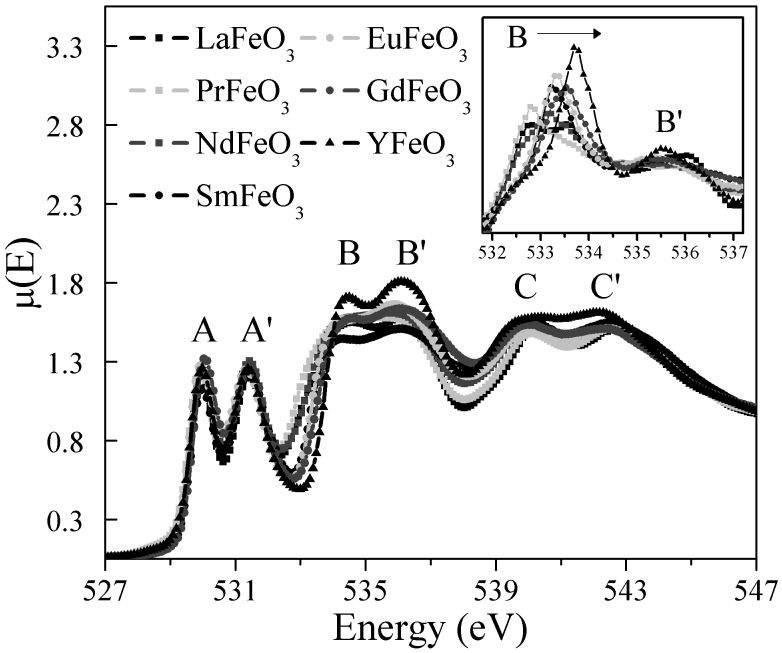

Figure 4.4: The O K-edge spectra from the $REFeO_3$ compounds are presented. Peaks A and A' arise from excitations to O 2p states interacting with Fe 3d t_{2g} and Fe 3d e_g^* states, respectively. Peaks B and B' arise from excitations to O 2p states interacting with RE states and peaks C and C' appear to arise from excitations to O 2p states interacting with Fe 4p/4s states (cf. 4.6). *Inset*: The derivative plot of the spectra shows that the inflection point of Peak B is shifted to higher energy as the ionic radius of the RE atom decreases.

[22]. Overall, the line shape and position of the peaks in the $REFeO_3$ spectra do not change as the identity of the RE is varied.

4.3.2 O K-edge

O K-edge spectra were collected to understand how the bonding and distribution of conduction states change within the $REFeO_3$ compounds through substitution of the RE and are presented in Figure 4.4. As these spectra result from the excitation of O 1s electrons to anti-bonding states that arise from O 2p orbitals interacting with orbitals on the coordinating atoms, they are very sensitive to changes in composition. These spectra are complex, but assignment of the spectral features observed can be made by comparing the $REFeO_3$ spectra to Fe_2O_3, as was done for $YFeO_3$ (Figure 4.5). This comparison clearly shows that peaks A, A', C, and C' arise from interactions of the O 2p orbitals with Fe orbitals and can be more specifically assigned as transitions to O 2p–Fe 3d t_{2g}

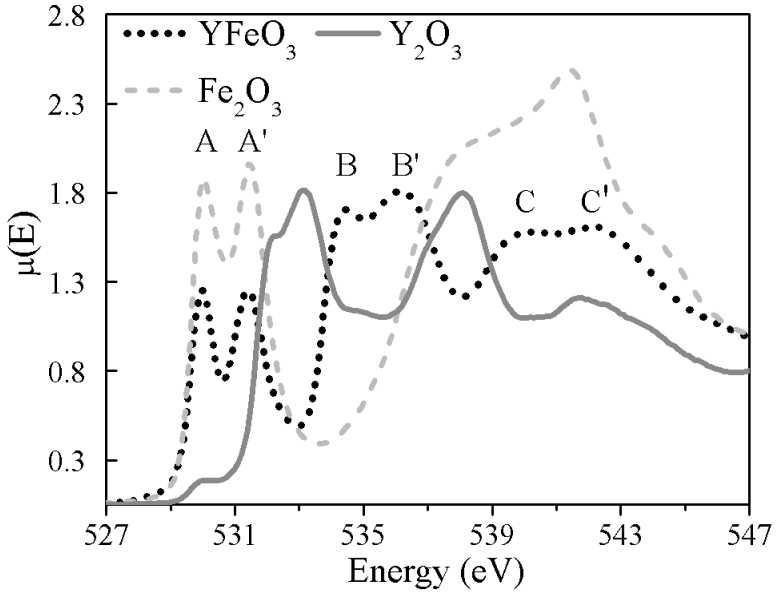

Figure 4.5: The O K-edge spectrum of $YFeO_3$ is compared with that from Y_2O_3 and Fe_2O_3. It can be clearly seen here that peaks A, A', C, and C' in $YFeO_3$ result from excitations to O 2p orbitals interacting with Fe orbitals.

(A), O 2p–Fe 3d e_g^* (A'), and O 2p–Fe 4p/4s (C,C') final states [199]. The crystal field splitting between A and A' is found to be 1.4 eV, which is reasonably close to the value of 1.8 eV found in the Fe L-edge spectra and 1.5 eV found in the Fe K-edge (*vide infra*), given the slight differences of the final state associated with the nature of each edge, further validating the assignment of peaks A and A'. No significant changes were observed in peaks A and A' as the RE was varied, confirming the observation from the Fe L_3-edge spectra (*vide supra*) that the FeO_6 octahedra are not affected by substitution of the RE atom.

Two peaks (B and B') are observed in the spectrum from $YFeO_3$ that do not correlate with the lowest-energy features observed in the spectrum from Y_2O_3. If one considers the effects of a shift in these peaks in the spectra from Y_2O_3 and $YFeO_3$ to be due to the difference in crystal structure between the two materials, peaks B and B' may tentatively be assigned to interactions between the RE atom and O. This assignment of peaks B and B' to RE–O interactions is reinforced by previous studies of comparable perovskite systems in which interactions between cations residing in the interstitial sites and O have been observed to occur at similar energies [212–214]. The assignment

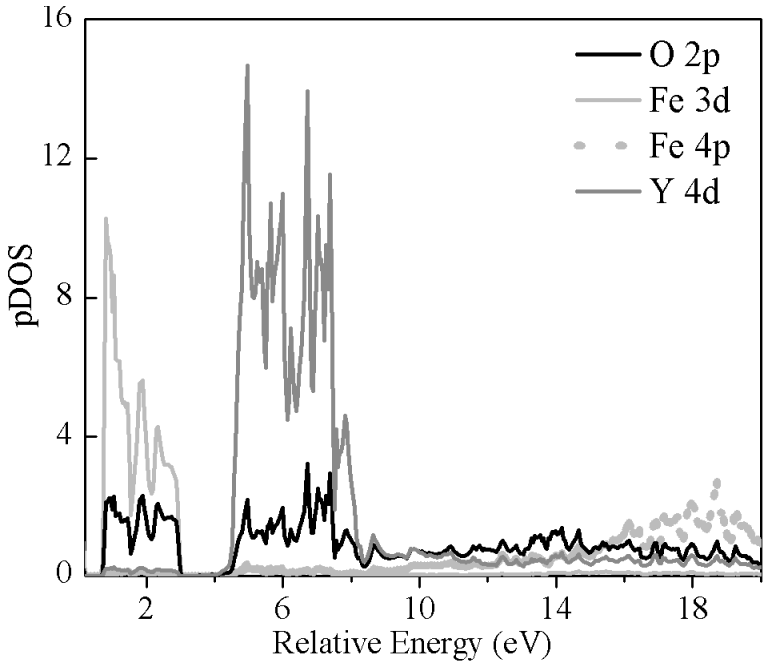

Figure 4.6: The partial DOS are presented and have been plotted relative to the Fermi-level. Significant overlap of Fe 3d and O 2p density is found at ∼0.7-2.9 eV while the Y 4d and O 2p densities are observed to overlap at ∼4.5-7.5 eV. The separation of these two regions of overlap matches well with the separation between peaks A' and B in the $REFeO_3$ O K-edge spectra (4.5), further confirming the assignment of peaks B and B' as resulting from excitations to O 2p states interacting with RE states.

of peaks B and B' to RE–O interactions is further confirmed by partial DOS calculations that were performed on $YFeO_3$ (Figure 4.6). These calculations indicate a strong overlap of O 2p and Y 4d density approximately 3 eV above a region of strong O 2p–Fe 3d overlap. The separation in energy observed in these calculations is mirrored in the O K-edge spectra, as peaks A' and B are separated by ∼3.1 eV. It should be noted that the observation of peaks B and B' at higher energy than A and A' does not imply stronger bonding between the RE and O than between Fe and O, but rather just that the RE 5d states are found at higher energy than Fe 3d states (as shown in the $YFeO_3$ DOS calculations presented in Figure 4.6).

With decreasing radius of the RE atom, peak B in the O K-edge spectra from the $REFeO_3$ oxides studied shifts to higher energy by ∼1.0 eV over the entire series (see derivative spectrum in the inset of Figure 4.4). The absolute reason for this observation is not known, but it appears to be related to changes in the coordination geometry and variations in the RE–O bond distances. The RE–O distances decrease with decreasing radius of the RE atom and may result in a change

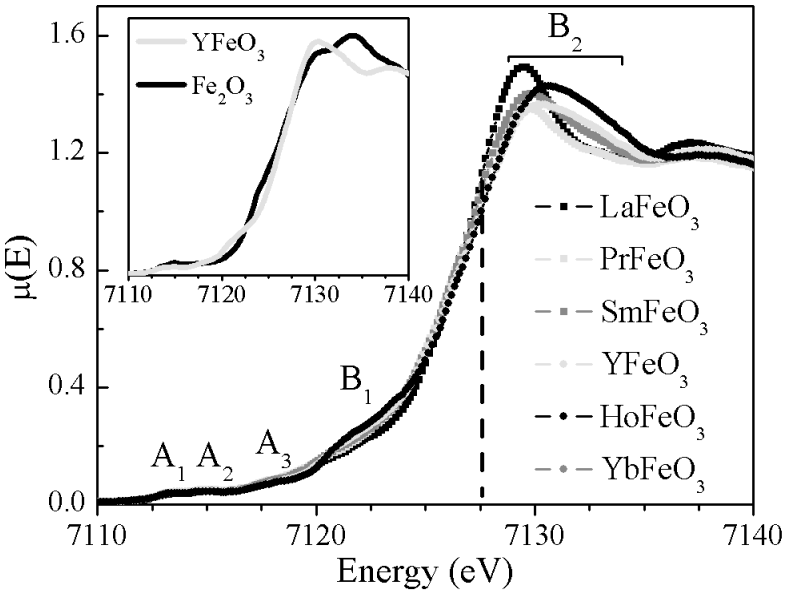

Figure 4.7: The Fe K-edge spectra from $REFeO_3$ compounds are plotted along with an Fe_2O_3 reference spectrum (solid line). Features A_1, A_2, and A_3 comprise the pre-edge region and arise primarily from 1s $\rightarrow$ 3d excitations. Features B_1 and B_2 make up the main-edge region and result from 1s$\rightarrow$4p transitions. The edge energy is represented by the dashed vertical line, and its position does not change between the spectra. Inset: Comparison of spectra from Fe_2O_3 and $YFeO_3$.

in the bonding interaction leading to a shift of the RE–O anti-bonding states. Alternatively, the shift in energy of peak B may be related to changes in the geometry around the RE centre. As the ionic radius of the RE decreases, the geometry of the O atoms around the RE atom changes such that it is closer to an ideal square anti-prismatic arrangement, which may result in more degenerate anti-bonding states [144]. In addition to these changes, the role of the f- orbitals in the RE–O interaction also cannot be discounted. It is likely that the origin of the shift in energy of peak B is not due to one single reason, but rather is a result of a mixture of the reasons suggested above.

4.3.3 Fe K-edge

To better understand how substitution of the RE impacts the electronic structure of the $REFeO_3$ compounds studied here, Fe K-edge spectra from several $REFeO_3$ compounds as well as Fe_2O_3 were collected and are presented in Figure 4.7. Examination of these spectra also provided an

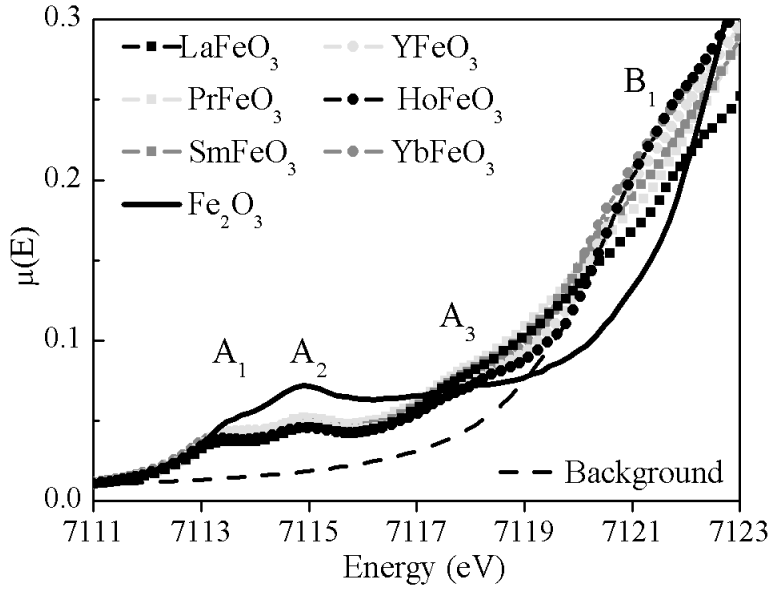

Figure 4.8: The pre-edge region of the $REFeO_3$ and Fe_2O_3 Fe K-edge spectra are plotted as well as the background resulting from dipolar contributions, which was modeled by an arctangent function (dashed line). The changes in intensity of features A_3 and B_1 depending on the RE atom are described in the text.

opportunity to observe how the intersite hybrid feature, found in the pre-edge region, is impacted by changes in the Fe–O–Fe bond angle. The Fe K-edge can generally be split into two regions; a pre-edge consisting of low intensity Fe 1s $\rightarrow$ Fe 3d excitations (A_1, A_2, and A_3 in Figure 4.7), and the main-edge region which arises from dipolar Fe 1s $\rightarrow$ 4p excitations (B_1 and B_2 in Figure 4.7) [2, 18, 24]. Multiple changes in the pre-edge and main-edge region of these spectra were observed depending on the RE and are discussed separately below.

4.3.3.1 Pre-edge Excitations

The pre-edge region of the Fe K-edge spectra are presented in Figure 4.8, and three significant features (A_1, A_2, and A_3) can be identified (B_1 is attributed to main-edge excitations, *vide infra*). In accordance with previous studies, and comparison to the Fe_2O_3 spectrum, features A_1 and A_2 are attributed to local excitations of 1s electrons to Fe 3d t_{2g} and e_g^* states, respectively [2, 18, 24]. Little change is observed in these features as the RE atom is changed, in agreement with the Fe

L_3-edge (Figure 4.3) and O K-edge (Figure 4.4) results. Of more interest is feature A_3, which is proposed here to result from a non-local Fe 4p–O 2p–Fe 3d intersite hybrid excitation [14]. Intersite hybrid peaks have been observed in many systems, including Fe_2O_3, TiO_2, $Fe_{1-x}Ga_xSbO_4$, and $Ca_{2-x}CuO_2Cl_2$, and are generally found at energies only slightly higher than the local, quadrupolar $1s \rightarrow 3d$ excitations [14, 15, 19, 22, 28]. The assignment of feature A_3 may also be made by direct comparison to the Fe_2O_3 reference spectrum (Figure 4.8), which is well known to exhibit an intersite hybrid feature at a similar energy to those observed in the spectra from the $REFeO_3$ compounds studied here [28].

To better visualize how the intersite hybrid feature (A_3) changes with the identity of the RE atom, the background arising from the main-edge dipolar excitation has been modeled using an arctangent function and the background-removed spectra are presented in [28]. While issues arising from the difficulty in fitting the background prevent quantitative analysis, it is qualitatively observed that the intensity of the intersite hybrid peak (A_3) decreases relative to the intensities of peaks A_1 and A_2 as the ionic radius of the RE decreases. In the $REFeO_3$ system, the Fe L_3- and O K-edges, coupled with crystallographic data, have shown that the Fe–O bond lengths are not affected by the identity of the RE atom, and only the tilt angle (α) between the FeO_6 octahedra change significantly [146–152]. Thus, the observed changes in the intensity of the intersite hybrid peak (A_3) cannot be attributed to changes between the Fe and O atoms and, therefore, must result from another reason. Here, the variation in intensity of the intersite hybrid peak is attributed to the change in the Fe–O–Fe bond angle with substitution of the RE atom (cf. Figure 2).

The influence of the bond angle on the intersite-hybrid feature can be understood by considering the interaction between the 4p orbitals on the absorbing Fe atom, the nearest-neighbor O 2p orbitals, and the NNN Fe 3d orbitals. The strength of the Fe 4p and NNN Fe 3d orbital interaction is maximized when the Fe–O–Fe bond angle is 180°. This is because both orbitals overlap with the same O 2p orbital. In contrast, no overlap between the Fe 4p and NNN Fe 3d orbitals may occur when the Fe–O–Fe bond angle is equal to 90°, resulting in a total quenching of the intersite hybrid feature. Between these two limiting cases, as the Fe–O–Fe bond angle approaches 90°, the amount

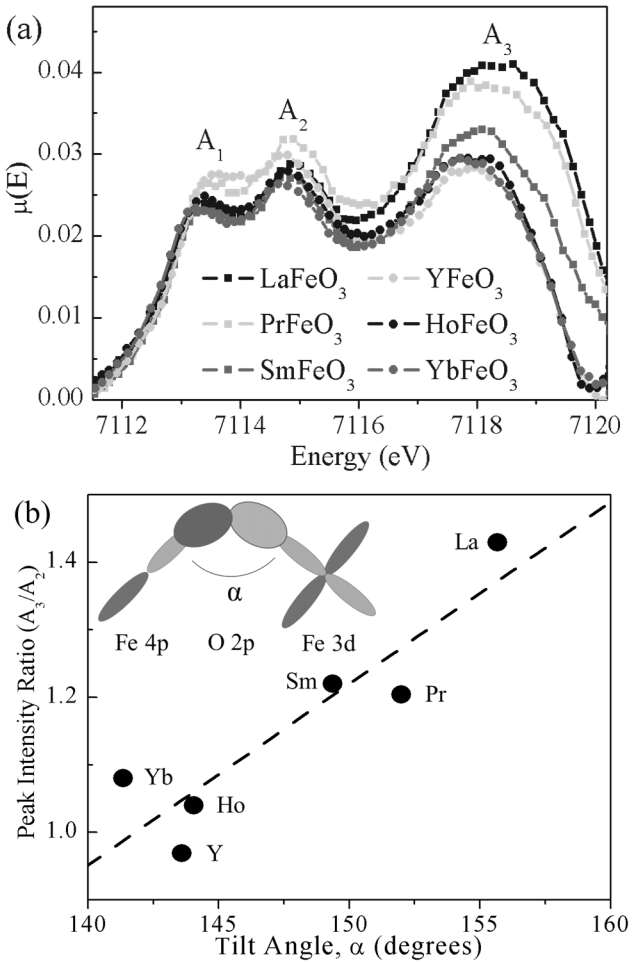

Figure 4.9: a) The background subtracted pre-edge region of the Fe K-edge spectra from the $REFeO_3$ compounds is plotted. Little change is observed in features A_1 and A_2 across the series of $REFeO_3$ compounds studied, as they result from local, 1s→3d transitions. The background due to the dipolar excitation was modeled using an arctan function. (b) Once the background was removed, it was found that the intensity of feature A_3 decreases with decreasing octahedral tilt angle. The dashed line is added to show a trend only, and does not imply a linear relationship. (The inset of (b) shows a schematic representation of the Fe 3d–O 2p–Fe 4p intersite hybrid interaction.)

of overlap between the Fe 4p and NNN Fe 3d orbitals, through a single O 2p orbital, is reduced, and is observed as a decrease in the intensity of the intersite hybrid spectral feature. This explanation is consistent with a previous study of Co oxides; however, this study only explored how the intersite-hybrid feature was affected by large changes in structure, which included simultaneous variations of bond angle and bond length [32].

4.3.3.2 Main-edge Excitations

Two important features are found in the main-edge region of the Fe K-edge spectra (B_1 and B_2 in Figure 4.7), and result from excitations of Fe 1s electrons to final states with mostly Fe 4p character. B_2 is the strongest feature in the spectra and is caused by a direct, local excitation of 1s electrons to unoccupied Fe 4p states. Comparison of the absorption edge energy, which is defined by the inflection point of the spectral edge, between the $REFeO_3$ spectra and the spectrum from Fe_2O_3 shows that the energies are nearly equal and confirms the previous conclusion that Fe adopts a +3 state in the $REFeO_3$ compounds. However, as the size of the RE atom decreases, the energy of the main edge peak maximum (labeled in Figure 4.7 as B_2) shifts to higher energy and becomes broader and slightly less intense. This may be related to the increase in the intensity of feature B_1, with decreasing size of the RE atom, but is most likely a result of variations in the multiscattering resonances, which overlap the high-energy region of these spectra. Multiscattering resonances occur when the core electron is excited to continuum states and the resulting photoelectron backscatters off multiple-neighboring atoms resulting in constructive and destructive interference [7]. As the ionic radius of the RE decreases, the RE–Fe bond distances decrease and result in a shorter path length, shifting the multi-scattering peak to higher energy [215].

While the changes in feature B_2 are well described by multi-scattering resonances, the origin of the changes in feature B_1, which increases in intensity as the radius of the RE decreases (Figure 4.8), are not as well understood. The partial DOS calculations from $YFeO_3$ (Figure 4.6) indicate that there is overlap between the Y 4d and Fe 4p states in this energy region, suggesting that an interaction between RE and Fe may be the origin of this feature. This interaction could either

occur directly or may be mediated through O 2p states. An alternate, more probable explanation that does not involve an Fe–RE interaction is that feature B_1 results from local excitations to lower-energy Fe 4p-states, as has been suggested for TiO_2 and brownmillerite-phase oxides [19, 30]. In this case, the increased intensity of feature B_1 is linked to the decreased intensity of feature A_3, which arises from excitations involving Fe 4p orbitals on the absorbing atom (see section 4.3.3.1). Because there must be a fixed number of Fe 4p states, as the Fe 4p character of the intersite hybrid state decreases (intensity of A_3 decreases, *vide supra*), the resulting excess of Fe 4p states that are not interacting with next-nearest-neighbor (NNN) Fe 3d states would shift to higher energy, increasing the density of Fe 4p states in this region and resulting in the increased intensity of feature B_1.

4.4 Conclusions

Rare-earth orthoferrites, having the chemical formula $REFeO_3$, have been synthesized and examined using XANES. The Fe L_3-edge and O K-edge spectra indicate that bonding within the FeO_6 octahedra are independent of the identity of the RE atom. In addition, the O K-edge spectra indicate that the RE atom interacts with the O atoms and that the absorption energy of this interaction appears to be dependent on both the RE–O bond distance and the coordination geometry of the RE centre. A non-local excitation due to intersite-hybrid interactions was observed in the pre-edge region of the Fe K-edge spectra, and the strength of this interaction was found to be directly related to the Fe–O–Fe bond angle. The relationship between this bond angle and the intensity of the intersite hybrid feature originates from the amount of overlap between the Fe 4p states on the absorbing Fe centre and the next-nearest-neighbor Fe 3d states through O 2p states. As the Fe–O–Fe bond angle decreases, the overlap between the local Fe 4p orbitals and NNN Fe 3d orbitals is reduced, resulting in a lowering of the intensity of the intersite hybrid peak. This orbital interaction is similar to those associated with superexchange interactions responsible for antiferromagnetic ordering [86, 154]. Thus, the observation of an intersite hybrid feature in transition-metal K-edge

XANES spectra may yield information on if superexchange is possible in a particular material.

Chapter 5

CONCLUSIONS

5.1 Summary and Significance

X-ray absorption spectroscopy is a powerful technique which can be used to determine the electronic and physical structures of a material. Transition-metal K-edge XANES is a technique that provides information about the oxidation state and coordination environment of the metal centre. One particularly informative region of a transition-metal K-edge XANES spectrum is the pre-edge, which may be used to elicit information about the electronic structure of a material and to track changes in the oxidation state and coordination environment of the metal centre. In order to fully extract all the information contained in the pre-edge region, it is necessary to understand the origins of the features found in this region and the factors that can affect them. To this end, this thesis has studied a series of materials that were selected to isolate the various factors which may affect the pre-edge features. As such, this thesis has increased the understanding of how the pre-edge features may be used to understand the physical and chemical properties of solid-state materials.

5.1.1 The pre-edge and changes in coordination environment and oxidation state

The effects of simultaneous changes in the oxidation state and coordination environment on the pre-edge region of transition-metal K-edge XANES spectra were studied in Chapter 2. In this study,

a series of $Sr_2Fe_{2-x}Mo_xO_6$ ($0.25 \leq x \leq 1.0$) materials were synthesized and studied using powder XRD and XANES in order to investigate how the oxidation state and coordination environments of Fe and Mo changed with varying Mo content. The powder XRD patterns revealed an increase in the lattice constant when the Mo content was increased from x = 0.50 to x = 0.65. This change appeared to correspond to a previously reported distortion of the cubic unit cell to a tetragonal unit cell [62, 63, 160]. Concurrent with this change, the pre-edge region of the Fe K-edge XANES shifted to lower energy, indicating Fe was partially reduced from Fe^{3+} to an $Fe^{2+/3+}$ mixture. The features in the Mo K-edge XANES spectra also shifted to lower energy, as a result of the partial reduction of Mo^{6+} to a mixture of Mo^{5+} and Mo^{6+}. The results from the XANES and powder XRD patterns presented in this chapter indicate that the change from a cubic to tetragonal unit cell is largely driven by the reduction of Fe^{3+} to $Fe^{2+/3+}$, as Fe^{2+} has a much larger ionic radius than Fe^{3+} [153].

In addition to observing changes in the pre-edge region due to changes in the oxidation state, significant changes in the intensity of the pre-edge features were also observed. These changes were attributed to changes in the coordination number around the Fe centres. When the coordination number decreases, the local Fe 4p states mix with the Fe 3d states, increasing the dipolar character of the pre-edge excitations. Here, the changes in coordination number corresponded to a change in the oxygen deficiency of the system. When the Mo content was low, the pre-edge of the Fe K-edge spectra were observed decrease in intensity, indicating that the system became less O-deficient. However, as the Mo content was increased past x = 0.50, the pre-edge features increased in intensity, indicating that the oxygen deficiency of the system increased.

The role of the synthetic method in determining the oxygen deficiency of the system was investigated by annealing the as-synthesized samples under a vacuum environment. The Fe K- and Mo K-edge XANES spectra showed that after annealing under vacuum, the samples became less oxygen deficient and that the Fe^{2+} was oxidized to Fe^{3+}. These results indicate that the presence of small quantities of $O_{2(g)}$ during synthesis may strongly impact the quality and properties of the $Sr_2Fe_{2-x}Mo_xO_6$ materials produced.

The analysis presented in this chapter serves as an example of how simultaneous changes in oxidation state and changes in coordination number can be analyzed using the pre-edge features from transition-metal XANES spectra. Careful comparison of the Fe K-edge spectra from the $Sr_2Fe_{2-x}Mo_xO_6$ system to the spectra from known standard compounds showed that changes in the oxidation state caused the pre-edge to shift to lower energy, while changes in coordination number lead to changes in intensity (and no shifts in energy). Studies such as this one, where both changes in coordination number and changes in oxidation state are concurrently analyzed, are important because changes in oxidation state are often linked to changes in coordination number through oxygen deficiency in many solid-state systems. These types of analyses will lead to a better understanding of the origins of the physical and chemical properties exhibited by solid-state materials.

5.1.2 The pre-edge and changes in bonding structure

The effects of changes in the covalency of the metal-ligand bond were explored by studying a series of $Cu_2FeSn_{3-x}Ti_xS_8$ ($0 \leq x \leq 3$) thiospinels in Chapter 3. The $Cu_2FeSn_{3-x}Ti_xS_8$ materials were successfully synthesized using a standard solid-state synthesis route, and the materials were characterized using XANES and LMTO-based electronic structure calculations. The intensity of the pre-edge in the Fe K-edge XANES spectra was observed to increase as the Fe–S bond length decreased. This increase in intensity was observed because decreasing the Fe–S bond length allowed for better overlap between the Fe 3d and S 3p states, increasing the dipolar character of the pre-edge excitations. Further, substituting Ti for Sn reduced the average electronegativity of the next-nearest-neighbour metal centres around the Fe sites, possibly allowing for better mixing between the Fe 3d and S 3p states. A similar increase was observed in the pre-edge region of the Ti K-edge spectra, though it was much smaller, due to the fact that Fe is more electronegative than Ti. The main-edge regions of the Fe K- and Ti K-edge spectra also indicated that long-range Fe/Ti–S–Sn interactions were present.

S K-edge XANES spectra were also collected from these materials to determine how the elec-

tronic structure of these materials changed as Ti was substituted for Sn. Because the features in the S K-edge arise from excitations to S 3p states interacting with metal orbitals, the S K-edge is highly reflective of the distribution of unoccupied conduction states of the materials. The pre-edge region of the S K-edge may also reveal important information about the coordination geometry around the metal centre, as was found in S K-edge XANES spectra from the Ti-rich $Cu_2FeSn_{3-x}Ti_xS_8$ materials. In general, these spectra were in close agreement with the electronic structure calculations performed in this study. The electronic structure calculations and S K-edge spectra showed that significant interactions between the S 4p and Sn 5s states occur, in agreement with a previous study [112]. The S K-edge spectra served to further confirm the interpretation of the Fe K-edge spectra from the $Cu_2FeSn_{3-x}Ti_xS_8$ materials.

The $Cu_2FeSn_{3-x}Ti_xS_8$ materials are known to undergo a SCO transition in which the Fe transitions from a HS to a LS state upon cooling. Based on this, it was thought these materials would offer a rare opportunity to study how the SCO transition affects the pre-edge region of the XANES spectrum from crystalline materials. To this end, a series of temperature-dependent Fe K-edge XANES spectra were collected from the $Cu_2FeSn_{3-x}Ti_xS_8$ thiospinels. Interestingly, no significant changes in the pre-edge were observed as the temperature was varied. This was probably caused by the covalent nature of the metal-ligand bonds found in the $Cu_2FeSn_{3-x}Ti_xS_8$ system, which results in the increased dipolar character of the pre-edge features (compared to most oxide-based compounds). Here, dipolar contributions from the S 3p orbitals dominated the pre-edge intensity, and effectively masked any changes which may have occurred due to the SCO transition. However, while no change in the pre-edge region was observed, large changes in the main-edge region were observed, which enabled a qualitative analysis of the SCO transition. Such an analysis could be used to provide insight into how the HS/LS equilibrium varies as a function of temperature within a given composition, but comparison of the absolute number of HS centres between different compositions was not possible.

The study presented in this chapter provided important insight regarding the impact of the changes in the covalency of the metal-ligand bond on the intensity of the pre-edge features. It may

be necessary to consider these changes in highly covalent systems, as they could be easily mistaken for changes in coordination number instead. Such a conclusion was ruled out in this study through a comparison of the Fe K-edge XANES spectra from the $Cu_2FeSn_{3-x}Ti_xS_8$ system to the Fe K-edge XANES spectra from known standards. This emphasizes the usefulness of collecting and comparing spectra from compounds with known structures and properties when interpreting the pre-edge. By including considerations regarding the covalency of the metal-ligand bond, future interpretations of the pre-edge will be more accurate, and will provide a better understanding of the bonding structures present in solid-state systems.

5.1.3 The pre-edge and changes in non-local excitations

The relationship between bond angle and the intensity of intersite hybrid peaks was explored in Chapter 4 through the study of a series of rare-earth orthoferrites, having the general formula $REFeO_3$ (RE = rare-earth, Y). These materials adopt a distorted perovskite structure, in which the octahedra are tilted, leading to Fe–O–Fe bond angles that are between 90° and 180°. One of the advantages of studying these materials is that the Fe–O–Fe bond (tilt) angle is directly proportional to the size of the RE atom, creating a controlled system where the relationship between the Fe–O–Fe bond angle and the intensity of the intersite hybrid peak could be directly examined.

The materials were successfully synthesized using a standard solid state synthesis method and examined using XANES. Fe L_3-edge XANES spectra were collected from these materials, and showed that no significant changes in the local structure of the FeO_6 octahedra occurred as the RE atom was changed. O K-edge spectra were also collected from these materials, and these spectra showed that the RE atom interacts with the O atoms. While the exact nature of this interaction has not been determined, this study shows that it depends on both the RE–O bond distance, and the coordination geometry of the RE centre. In general, the Fe L_3- and O K-edge spectra showed that the local structure around the Fe centres did not change as the RE atom was varied.

In the $REFeO_3$ orthoferrites, the intersite hybrid peak results from the excitation of Fe 1s electrons to next-nearest-neighbor Fe 3d states interacting with Fe 4p states on the absorbing atom

through O 2p states. In this study, by analyzing the pre-edge region of the Fe K-edge spectra from these materials, it was experimentally confirmed that there is a direct relationship between the Fe–O–Fe bond angle and the intensity of the intersite hybrid peak. The relationship between this bond angle and the intensity of the intersite hybrid feature originates from the amount of overlap between the Fe 4p states on the absorbing Fe centre and the next-nearest-neighbor Fe 3d states, through O 2p states. As the Fe–O–Fe bond angle decreases, the overlap between the local Fe 4p orbitals and next-nearest-neighbour Fe 3d orbitals is reduced, resulting in a lowering of the intensity of the intersite hybrid peak. This was the first study to present direct evidence of the relationship between the Fe–O–Fe bond angle and the intensity of the intersite hybrid. Thus this study has provided fundamental insight into the nature of a specific pre-edge feature reported only for solid-state systems and how it can be separated from both the pre-edge and main-edge features.

5.2 Future Work

This thesis has provided insight into the origins of the features in the pre-edge of a transition-metal K-edge XANES spectrum, and how they can be used to understand material properties. However, many questions regarding both the pre-edge region and the materials studied here remain. As such, continuing to research the properties of the systems explored in this thesis would lead to a richer understanding of these materials and the pre-edge region in XANES spectra. To this end, proposed directions of future research for each study presented in this thesis are described below.

The Sr_2FeMoO_6 double perovskite is a technologically relevant compound because it has been shown to exhibit colossal magnetoresistance (CMR) [57]. However, several other double perovskites have also been shown to be half-metallic and exhibit CMR (e.g. Ba_2FeMoO_6) [157, 166]. Interestingly, in many studies of the double perovskites, the exact effects of the A-site cation are often ignored. A possible way to explore the impact of the A-site cation in these materials would be to study a series of $Sr_{2-x}Ba_xFe_{2-y}Mo_yO_6$ compounds. In these materials, because Ba and Sr have different sizes, the switch from a cubic to a tetragonal unit cell may occur at a different Fe/Mo

composition than in $Sr_2Fe_{2-x}Mo_xO_6$. Collecting pXRD patterns and XANES spectra from these materials could lead to a better understanding of how the A-site cation affects the structure of the material and the oxidation states of the B and B' cations. Such a study would provide further insight into the mechanism that causes the switch from a cubic to tetragonal unit cell found in the $Sr_2Fe_{2-x}Mo_xO_6$ materials. Further, if these experiments are coupled with measurements of the materials magnetoresistive properties, a better understanding of the origin of these properties (and how they can be optimized) may also be achieved.

The $Cu_2FeSn_{3-x}Ti_xS_8$ thiospinels were studied in Chapter 3 as a means of studying how the spin-crossover transition may affect the pre-edge region of Fe K-edge XANES spectra. In this regard, no change was found in the pre-edge and the study was unsuccessful. This was a result of both the large changes in main-edge features which could not be fully resolved from the pre-edge features, and the highly covalent nature of the system, which may have overshadowed small changes in the pre-edge due to the SCO transition. Using a higher resolution technique, such as Resonant Elastic Inelastic X-ray Scattering (REIXS), may help to fully resolve the pre-edge from the main-edge, allowing for changes due to the SCO to be observed in the pre-edge. The influence of core-hole lifetime broadening effects are reduced in this technique by collecting only one emission line in the fluorescence spectrum [16, 22]. Also, instead of using the pre-edge region of Fe K-edge XANES spectra to study the SCO transition, it may be more beneficial to study the SCO transition using Fe $L_{2,3}$-edge XANES. The Fe $L_{2,3}$-edges consist of excitations of Fe 2p electrons to Fe 3d states, and thus contain strong features which directly probe the 3d states. In this regard, an initial study of the $Cu_2FeSn_{3-x}Ti_xS_8$ materials using the Fe L_3-edge has been completed and shows changes consistent with those observed in the Fe L_3-edge spectra from molecular SCO compounds [216]. Based on these initial results, a quantitative study of the HS/LS equilibrium in the $Cu_2FeSn_{3-x}Ti_xS_8$ thiospinels may be possible using Fe L_3-edge XANES.

In addition to the study of the SCO transition, the study of the $Cu_2FeSn_{3-x}Ti_xS_8$ thiospinels revealed that the covalency of the Fe–S bond changed as Ti was substituted for Sn. Two changes lead to this observation in these materials: the decreased Fe–S bond length allowing for bet-

ter overlap between the Fe 3d and S 3p orbitals, and the substitution of less electronegative Ti for the more electronegative Sn. To separate the influences of changes in orbital overlap versus changes in the electronegativity of the next-nearest-neighbor atom, a XANES-based study of the $Ag_{2-x}Cu_xFeSn_3S_8$ compounds would be useful [99]. (The synthesis of thiospinels which contain both Ag and Ti was attempted in this work, but did not yield phase-pure products.) While the electronegativity differences of Ag and Cu are large, based on the research presented in Chapter 3, these ions are not expected to impact the Fe–S bond covalency [27]. (The electronic structure calculations indicated the presence of only minor interactions between Cu and Fe in the $Cu_2FeSn_{3-x}Ti_xS_8$ compounds.) Thus, only changes in the overlap of the Fe 3d and S 4p orbitals due to changes in the Fe–S bond length as the larger Ag is substituted for Cu are expected to impact the covalency of the Fe–S bond [99]. Because of this, such a study would provide better insight into the importance of the electronegativity of the next-nearest-neighbor atom on the covalency of the metal-ligand bond, and how these changes may affect the pre-edge region of transition-metal K-edge spectra.

Chapter 4 presented a XANES study of the rare-earth orthoferrites, and focused on investigating the ill-studied non-local excitation known as an intersite hybrid peak. Interestingly, while the intersite hybrid peak has been observed for several transition-metal oxides, it has not been observed in transition-metal chalcogenides. This is probably due to the difficulty of finding transition-metal chalcogenides that contain corner-sharing octahedra. (Corner-sharing of the octahedra allows for favorable overlap between np and (n-1)d orbitals through S 3p states because the M-S-M' bond angle will be between 90° and 180°.) To this end, a XANES study of the $UFeS_3$-type compounds may be useful. These materials adopt a *Cmcm* unit cell, in which layers of corner-sharing FeS_6 octahedra are sandwiched between layers of US_8 polyhedra [217]. Because this system contains corner-sharing FeS_6 octahedra, the Fe K-edge spectra from this system may provide evidence of an intersite hybrid peak in a chalcogenide-based system. Further, these systems also have the advantage of being highly substitutable, as Th can be substituted for U and Mn and Sc may be substituted for Fe [217]. This could allow for advantageous manipulation of the structure of these materials via composition (i.e. bond lengths and angles; similar to the $REFeO_3$ study). The observation of

an intersite hybrid peak in a chalcogenide-based system would further the understanding of this interesting peak, which to this point has only been reported in oxides. Such an observation (or the continued lack of such an observation) would further our knowledge about the features that may be observed in the pre-edge region of transition-metal K-edge XANES spectra.

This thesis has shown how the pre-edge features found in transition-metal K-edge XANES spectra may be used in the investigation of several different solid-state compounds. These studies have not only furthered the understanding of the physical properties of these materials, but have also furthered the understanding of the origins of the features found in the pre-edge. To this end, the studies presented here have attempted to discern how the pre-edge region varies as the metal centre changes (i.e., changes in coordination number and oxidation state) and as the structure changes (i.e., changes in bond distance, covalency, and bond angle). As such, these studies have been successful in helping make the pre-edge region of transition-metal XANES spectra a powerful tool for investigating solid-state materials.

REFERENCES

[1] De Groot, F.; Vogel, J. In *Neutron and X-ray Spectroscopy*; Hippert, F.; Al, E., Eds.; Springer: Netherlands, 2006; pp 3–66.

[2] Waychunas, G. A.; Apted, M. J.; Brown, G. E. *Phys. Chem. Mineral.* **1983**, *10*, 1–9.

[3] Jiang, D.-T. In *Synchrotron Radiation: Earth, Environmental and Materials Sciences Applications*; Henderson, G.; Baker, D. R., Eds.; Mineralogical Association of Canada: Ottawa, ON, 2002; Chapter 4, pp 65–98.

[4] Della Longa, S.; Girasole, M.; Congiu Castellano, A.; Bianconi, A.; Kovtun, A.; Soldatov, A. *Euro. Biophys. J.* **1998**, *1998*, 541– 548.

[5] Farges, F.; Chalmin, E.; Vignaud, C.; Pallot-Frossard, I.; Susini, J.; Bargar, J.; Brown, G. E.; Menu, M. *Phys. Scr.* **2005**, *T115*, 885–887.

[6] Ashley, C.; Doniach, S. *Phys. Rev. B* **1975**, *11*, 1279–1288.

[7] Rehr, J. J.; Albers, R. C. *Rev. Mod. Phys.* **2000**, *72*, 621–654.

[8] Koningsberger, D. C.; Mojet, B. L.; van Dorssen, G. E.; Ramaker, D. E. *Top. Catal.* **2000**, *10*, 143–155.

[9] Thompson, A.; Attwood, D.; Gullikson, E.; Howells, M.; Kim, K. J.; Kirz, J.; Kortright, J.; Lindau, I.; Pianetta, P.; Robinson, A.; Scofield, J.; Underwood, J.; Vaughn, D.; Williams, G.; Winick, H. *X-ray Data Booklet*; Lawrence Berkeley National Laboratory: Berkeley, 2009.

[10] Attwood, D. *Soft X-rays and Extreme Ultraviolet Radiation: Principles and Applications*; Cambridge University Press: New York, 1999.

[11] Griffiths, D. J. *Introduction to Quantum Mechanics*, 2nd ed.; Pearson Prentice Hall: Upper Saddle River, NJ, 2005.

[12] Atkins, P.; De Paula, J. In *Physical Chemistry*, 9th ed.; W.H. Freeman and Company: New York, 2010; Chapter 9, pp 324–367.

[13] Almbladh, C.; Minnhagen, P. *Phys. Rev. B* **1978**, *17*, 929–939.

[14] de Groot, F.; Vankó, G.; Glatzel, P. *J. Phys. Condens. Matter* **2009**, *21*, 104207.

[15] Gougoussis, C.; Rueff, J.; Calandra, M.; D'Astuto, M.; Jarrige, I.; Ishii, H.; Shukla, A.; Yamada, I.; Azuma, M.; Takano, M. *arXiv*, 1–6.

[16] Rueff, J.-P.; Journel, L.; Petit, P.-E.; Farges, F. *Phys. Rev. B* **2004**, *69*, 1–9.

[17] Arrio, M.; Rossano, S.; Brouder, C.; Galoisy, L.; Calas, G. *Europhys. Lett.* **2000**, *51*, 454–460.

[18] Westre, T. E.; Kennepohl, P.; DeWitt, J. G.; Hedman, B.; Hodgson, K. O.; Solomon, E. I. *J. Am. Ceram. Soc.* **1997**, *119*, 6297–6314.

[19] Cabaret, D.; Joly, Y.; Renevier, H.; Natoli, C. R. *J. Synchrotron Rad.* **1999**, *0495*, 258–260.

[20] Yamamoto, T. *X-Ray Spectrom.* **2008**, *37*, 572–584.

[21] George, S. D.; Brant, P.; Solomon, E. I. *J. Am. Chem. Soc.* **2005**, *127*, 667–74.

[22] Glatzel, P.; Mirone, A.; Eeckhout, S.; Sikora, M.; Giuli, G. *Phys. Rev. B* **2008**, *77*, 1–7.

[23] Farges, F.; Rossano, S.; Lefrère, Y.; Wilke, M.; Jr., G. E. B. *Phys. Scr.* **2005**, *957*, 957.

[24] Wilke, M.; Farges, F.; Petit, P. E.; Brown, G. E. J.; Martin, F. *Am. Mineral.* **2001**, *86*, 714–730.

[25] Gaultois, M. W.; Grosvenor, A. P. *J. Phys. Chem. C* **2010**, *114*, 19822–19829.

[26] Farges, F.; Siewert, R.; Brown, G. E.; Guesdon, A.; Morin, G. *Can. Mineral.* **2006**, *44*, 731–753.

[27] Allred, A. L. *J. Inorg. Nucl. Chem.* **1961**, *17*, 215–221.

[28] Sigrist, J. A.; Gaultois, M. W.; Grosvenor, A. P. *J. Phys. Chem. A* **2011**, *115*, 1908–1912.

[29] Wu, Z. Y. *AIP Conf. Proc.* **2003**, *652*, 497–508.

[30] Grosvenor, A. P.; Greedan, J. E. *J. Phys. Chem. C* **2009**, *113*, 11366–11372.

[31] Chen, J.; Lee, J.; Huang, S.; Lu, K.; Jeng, H.; Chen, C.; Haw, S.; Chou, T.; Chen, S.; Hiraoka, N.; Ishii, H.; Tsuei, K.; Yang, T. *Phys. Rev. B* **2010**, *82*, 1–8.

[32] Vankó, G.; de Groot, F. M. F.; Huotari, S.; Cava, R. J.; Lorenz, T.; Reuther, M. *arXiv* **2008**, 1–7.

[33] Muñoz Páez, A.; Ruiz-López, M. F. *J. Phys. Chem.* **1995**, *99*, 16499–16499.

[34] Krinsky, S. In *Third Generation Hard X-ray Synchrotron Radiation Sources*; Mills, D. M., Ed.; John Wiley & Sons: New York, 2002; Chapter 1, pp 1–41.

[35] Crease, R. P. *Phys. Perspect.* **2008**, *10*, 438–467.

[36] Johnston, R.; Tomboulian, D. *Phys. Rev.* **1954**, *94*, 1585–1589.

[37] Chasman, R.; Green, G. K.; Rowe, E. M. *IEEE Trans. Nucl. Sci.* **1975**, *22*, 1765–1767.

[38] Sham, T. K. In *Synchrotron Radiation: Earth, Environmental and Materials Sciences Applications*; Henderson, G.; Baker, D. R., Eds.; Mineralogical Association of Canada: Ottawa, ON, 2002; Chapter 1, pp 1–24.

[39] Crease, R. P. *Phys. Perspect.* **2009**, *11*, 15–45.

[40] Zbasnik, J.; et al. *IEEE Trans. Appl. Supercond.* **2001**, *11*, 2531–2534.

[41] Brown, G.; Halbach, K.; Harris, J.; Winick, H. *Nucl. Instr. Meth. Phys. Res.* **1983**, *208*, 65–77.

[42] Mills, D. M. In *Third Generation Hard X-ray Synchrotron Radiation Sources2*; Mills, D. M., Ed.; John Wiley & Sons: New York, 2002; Chapter 2, pp 41–100.

[43] Arfelli, F.; Bravin, A.; Barbiellini, G.; Cantatore, G.; Castelli, E.; Di Michiel, M.; Poropat, P.; Rosei, R.; Sessa, M.; Vacchi, A.; Dalla Palma, L.; Longo, R.; Bernstorff, S.; Savoia, A.; Tromba, G. *Rev. Sci. Instrum.* **1995**, *66*, 1325.

[44] Paterson, D. J.; Boldeman, J. W.; Cohen, D. D.; Ryan, C. G. *AIP Conf. Proc.* **2007**, *879*, 864–867.

[45] Hussain, Z. *LBNL Paper* **1981**, *LBL*, 12729.

[46] Cramer, S. P.; Tench, O.; Yocum, M.; George, G. N. *Nucl. Instrum. Methods Phys. Res., Sect. A* **1988**, *266*, 586–591.

[47] Lee, P.; Citrin, P.; Eisenberger, P.; Kincaid, B. *Rev. Mod. Phys.* **1981**, *53*, 769–806.

[48] Goodenough, J. B. *Reports on Progress in Physics* **2004**, *67*, 1915–1993.

[49] Liu, L.-G. *Surv. Geophys.* **1989**, *10*, 63–81.

[50] Kotecki, D. E. *Integr. Ferroelectr.* **1997**, *16*, 1–19.

[51] Routbort, J.; Goretta, K. C.; Cook, R. E.; Wolfenstine, J. *Solid State Ionics* **2000**, *129*, 53–62.

[52] Serrate, D.; Teresa, J. M. D.; Ibarra, M. R. *J. Phys. Condens. Matter* **2007**, *19*, 023201.

[53] Howard, C. J.; Kennedy, B. J.; Woodward, P. M. *Acta Crystallogr. B* **2003**, *59*, 463–471.

[54] King, G.; Woodward, P. M. *J. Mater. Chem.* **2010**, *20*, 5785.

[55] Galasso, F.; Darby, W. *J. Phy. Chem.* **1962**, *66*, 131–132.

[56] Anderson, M. T.; Greenwood, K. B.; Taylor, G. A.; Poeppelmeier, K. R. *Prog. Solid St. Chem.* **1993**, *22*, 197–233.

[57] Kobayashi, K.-I.; Kimura, T.; Sawada, H.; Terakura, K.; Tokura, Y. *Nature* **1998**, *395*, 677–680.

[58] Yamamoto, T.; Liimatainen, J.; Lindén, J.; Karppinen, M.; Yamauchi, H. *J. Mater. Chem.* **2000**, *10*, 2342–2345.

[59] J. Rager, M. Zipperle, A. Sharma; MacManus-Driscoll, J. L. *J. Am. Ceram. Soc.* **2004**, *87*, 1330–1335.

[60] Lindén, J.; Yamamoto, T.; Karppinen, M.; Yamauchi, H.; Pietari, T. *Applied Physics Letters* **2000**, *76*, 2925.

[61] MacManus-Driscoll, J.; Sharma, A.; Bugoslavsky, Y.; Branford, W.; Cohen, L.; Wei, M. *Adv. Mater.* **2006**, *18*, 900–904.

[62] Liu, G. Y.; Rao, G. H.; Feng, X. M.; Yang, H. F.; Ouyang, Z. W.; Liu, W. F.; Liang, J. K. *J. Alloys Compd.* **2003**, *34*, 42–47.

[63] Fang, T.-T.; Ko, T.-F. *J. Am. Ceram. Soc.* **2003**, *86*, 1453–1455.

[64] Momma, K.; Izumi, F. *J. Appl. Crystallogr.* **2008**, *41*, 653–658.

[65] Woodward, P.; Hoffmann, R.-D.; Sleight, A. *J. Mater. Res.* **1994**, *9*, 2118–2127.

[66] Sleight, A. W.; Weiher, J. F. *J. Phys. Chem Solids* **1972**, *33*, 679–687.

[67] Azuma, M.; Kaimori, S.; Takano, M. *Chemistry of Materials* **1998**, *10*, 3124–3130.

[68] Karen, P.; Woodward, P. M. *J. Mater. Chem.* **1999**, *9*, 789–797.

[69] Torres-Pardo, A.; Krumeich, F.; González-Calbet, J. M.; García-González, E. *J. Am. Chem. Soc.* **2010**, *132*, 9843–9.

[70] Niebieskikwiat, D.; Prado, F.; Caneiro, A.; Sánchez, R. *Phys. Rev. B* **2004**, *70*, 9–12.

[71] Muñoz García, A. B.; Pavone, M.; Carter, E. A. *Chem. Mater.* **2011**, *23*, 4525–4536.

[72] Meneghini, C.; Ray, S.; Liscio, F.; Bardelli, F.; Mobilio, S.; Sarma, D. *Phys. Rev. Lett.* **2009**, *103*, 1–4.

[73] Sharma, A.; Berenov, A.; Rager, J.; Branford, W.; Bugoslavsky, Y.; Cohen, L. F.; MacManus-Driscoll, J. L. *Appl. Phys. Lett.* **2003**, *83*, 2384.

[74] Jurca, B.; Berthon, J.; Dragoe, N.; Berthet, P. *J. Alloys Compd.* **2009**, *474*, 416–423.

[75] Menéndez, N.; García-Hernández, M.; Sánchez, D.; Tornero, J. D.; Martínez, J. L.; Alonso, J. a. *Chemistry of Materials* **2004**, *16*, 3565–3572.

[76] Balcells, L.; Navarro, J.; Bibes, M.; Roig, A.; Martínez, B.; Fontcuberta, J. *Appl. Phys. Lett.* **2001**, *78*, 781.

[77] Shimada, T.; Nakamura, J.; Motohashi, T.; Yamauchi, H.; Karppinen, M. *Chem. Mater.* **2003**, *15*, 4494–4497.

[78] Fang, T.-T.; Lin, J.-C. *J. Mater. Sci.* **2005**, *40*, 683–686.

[79] Zhang, L.; Zhou, Q.; He, Q.; He, T. *J. Power Sources* **2010**, *195*, 6356–6366.

[80] Ray, S.; Kumar, A.; Sarma, D.; Cimino, R.; Turchini, S.; Zennaro, S.; Zema, N. *Phys. Rev. Lett.* **2001**, *87*, 5–8.

[81] Retuerto, M.; Alonso, J. a.; Martínez-Lope, M. J.; Martínez, J. L.; García-Hernández, M. *Appl. Phys. Lett.* **2004**, *85*, 266.

[82] Tovar, M.; Causa, M.; Butera, A.; Navarro, J.; Martínez, B.; Fontcuberta, J.; Passeggi, M. *Phys. Rev. B* **2002**, *66*, 1–5.

[83] Sarma, D.; Ray, S.; Tanaka, K.; Kobayashi, M.; Fujimori, A.; Sanyal, P.; Krishnamurthy, H.; Dasgupta, C. *Phys. Rev. Lett.* **2007**, *98*, 1–4.

[84] Bibes, M.; Barthélémy, A. *IEEE Trans. Electron Devices* **2007**, *54*, 1003–1023.

[85] Jooss, C.; Wu, L.; Beetz, T.; Klie, R. F.; Beleggia, M.; Schofield, M. A.; Schramm, S.; Hoffmann, J.; Zhu, Y. *PNAS* **2007**, *104*, 13597–602.

[86] Getzlaff, M. *Fundamentals of Magnetism*; Springer: Berlin, Heidelberg, New York, 2008.

[87] Kuepper, K.; Balasz, I.; Hesse, H.; Winiarski, a.; Prince, K. C.; Matteucci, M.; Wett, D.; Szargan, R.; Burzo, E.; Neumann, M. *Physica Status Solidi (a)* **2004**, *201*, 3252–3256.

[88] Moreno, M. *Solid State Communications* **2001**, *120*, 161–164.

[89] Kanchana, V.; Vaitheeswaran, G.; Alouani, M.; Delin, a. *Physical Review B* **2007**, *75*, 3–6.

[90] Herrero-Martín, J.; García, J.; Subías, G.; Blasco, J.; Sánchez, M. C. *J. Phys. Condens. Matter* **2004**, *16*, 6877–6890.

[91] Retuerto, M.; Jiménez-Villacorta, F.; Martínez-Lope, M. J.; Huttel, Y.; Roman, E.; Fernández-Díaz, M. T.; Alonso, J. A. *Phys. Chem. Chem. Phys.* **2010**, *12*, 13616–25.

[92] Makovicky, E. *Rev. Mineral. Geochem.* **2006**, *61*, 7–125.

[93] Vaughan, D. J. *Rev. Mineral. Geochem.* **2006**, *61*, 231–264.

[94] Tossell, J. A.; Vaughan, D. J. In *Theoretical Geochemistry: Application of Quantum Mechanics in the Earth and Mineral Sciences*; Oxford University Press: New York, 1992; Chapter 6, pp 274–325.

[95] Bernardini, G. P.; Borrini, D.; Caneschi, A.; Di Benedetto, F.; Gatteschi, D.; Ristori, S.; Romanelli, M. *Phys. Chem. Miner.* **2000**, *27*, 453–461.

[96] Buckley, A. N.; Skinner, W. M.; Harmer, S. L.; Pring, A.; Fan, L.-J. *Geochim. Cosmochim. Acta* **2009**, *73*, 4452–4467.

[97] Dysleski, L.; Frank, S. E.; Strauss, S. H.; Dorhout, P. K. In *Interfacial Applications in Environmental Engineering*; Keane, M. A., Ed.; New York, 2003; Chapter 7, pp 111–126.

[98] Womes, M.; Reibel, C.; Mari, A.; Zitoun, D. *J. Solid State Chem.* **2011**, *184*, 753–763.

[99] Garg, G.; Gupta, S.; Maddanimath, T.; Gascoin, F.; Ganguli, A. K. *Solid State Ionics* **2003**, *164*, 205–209.

[100] Laganovsky, A.; Kormosh, Z.; Sachanyuk, V.; Parasyuk, O. *Mater. Sci. Eng., C* **2008**, *28*, 1112–1116.

[101] Suekuni, K.; Tsuruta, K.; Ariga, T.; Koyano, M. *J. Appl. Phys.* **2011**, *109*, 083709.

[102] Ramirez, A.; Cava, R.; Krajewski, J. *Nature* **1997**, *386*, 156–159.

[103] Park, M.; Kwon, S.; Min, B. *Phys. Rev. B* **2001**, *64*, 2–5.

[104] Tachibana, M. *Solid State Commun.* **2012**, *152*, 849–851.

[105] Robbins, M. *Geochim. Cosmochim. Acta* **1975**, *39*, 883–888.

[106] Vaughan, D. J.; Burns, R. G.; Burns, V. M. *Geochim. Cosmochim. Acta* **1971**, *35*, 365–381.

[107] Jumas, J. C.; Philippot, E.; Maurin, M. *Acta Crystallogr., Sect. B: Struct. Sci* **1979**, *35*, 2195–2197.

[108] Branci, C.; Sarradin, J. *Mol. Cryst. Liq. Cryst. Sci. Technol., Sect. A* **1998**, *311*, 69–74.

[109] Branci, C.; Sarradin, J.; Olivier-Fourcade, J.; Jumas, J. *J. Power Sources* **1999**, *81-82*, 282–285.

[110] Kormosh, Z.; Fedorchuk, A.; Wojciechowski, K.; Tataryn, N.; Parasyuk, O. *Mater. Sci. Eng., C* **2011**, *31*, 540–544.

[111] Sachanyuk, V.; Fedorchuk, A.; Olekseyuk, I.; Parasyuk, O. *Mater. Res. Bull.* **2007**, *42*, 143–148.

[112] Branci, C.; Womes, M.; Lippens, P. E.; Olivier-Fourcade, J.; Jumas, J. C. *J. Solid State Chem.* **2000**, *150*, 363–370.

[113] Real, J. A.; Castro, I.; Bousseksou, A.; Verdaguer, M.; Burriel, R.; Castro, M.; Linares, J.; Varret, F. *Inorg. Chem.* **1997**, *36*, 455–464.

[114] Paulsen, H.; Grünsteudel, H.; Meyer-Klaucke, W.; Gerdan, M.; Grünsteudel, H.; Chumakov, A. I.; Rüffer, R.; Winkler, H.; Toftlund, H.; Trautwein, A. X. *Euro. Phys. J. B* **2001**, *23*, 463–472.

[115] Gütlich, P.; Goodwin, H. A. *Top. Curr. Chem.* **2004**, *233*, 1–47.

[116] Hauser, A. *Adv. Polym. Sci.* **2004**, *233*, 49–58.

[117] Gütlich, P.; Garcia, Y.; Goodwin, H. a. *Chem. Soc. Rev.* **2000**, *29*, 419–427.

[118] Kawakami, T.; et al. *Nature Chem.* **2009**, *1*, 371–6.

[119] Gudyma, I. V.; Maksymov, A. I. *Physica B* **2010**, *405*, 2534–2537.

[120] Hannay, C.; Hubin-Franskin, M.-J.; Grandjean, F.; Briois, V.; Itié, J.-P.; Polian, A.; Trofimenko, S.; Long, G. J. *Inorg. Chem.* **1997**, *36*, 5580–5588.

[121] Halder, G. J.; Kepert, C. J.; Moubaraki, B.; Murray, K. S.; Cashion, J. D. *Science* **2002**, *298*, 1762–5.

[122] Takano, M.; Nasu, S.; Abe, T.; Yamamoto, K.; Endo, S.; Takeda, Y.; Goodenough, J. *Phys. Rev. Lett.* **1991**, *67*, 3267–3270.

[123] Létard, J.-F.; Guionneau, P.; Goux-Capes, L. *Top. Curr. Chem.* **2004**, *255*, 221–249.

[124] Kahn, O. *Science* **1998**, *279*, 44–48.

[125] Halcrow, M. A. *Chem. Soc. Rev.* **2011**, *40*, 4119–42.

[126] Tsai, Y.; Chang, W.; Huang, S.; Lin, J.-Y.; Lee, J.; Chen, J.; Wu, K.; Uen, T.; Gou, Y.; Juang, J. *Physica B* **2009**, *404*, 1404–1408.

[127] Haas, O.; Ludwig, C.; Bergmann, U.; Singh, R.; Braun, A.; Graule, T. *J. Solid State Chem.* **2011**, *184*, 3163–3171.

[128] Medarde, M.; Dallera, C.; Grioni, M.; Voigt, J.; Podlesnyak, A.; Pomjakushina, E.; Conder, K.; Neisius, T.; Tjernberg, O.; Barilo, S. *Phys. Rev. B* **2006**, *73*, 1–10.

[129] Rao, C. N. R.; Seikh, M.; Narayana, C. *Top. Curr. Chem.* **2004**, *254*, 1–21.

[130] Wu, D.-Y.; Sato, O.; Einaga, Y.; Duan, C.-Y. *Angew. Chem.* **2009**, *121*, 1503–1506.

[131] Grunes, L. A. *Phys. Rev. B* **1983**, *27*, 2111–2131.

[132] Erenburg, S. B.; Bausk, N.; Lavrenova, L.; Mazalov, L. *Nucl. Instrum. Methods Phys. Res., Sect. A* **2000**, *448*, 351–357.

[133] Marcelli, A.; Cibin, G.; Di Matteo, S.; Chaboy, J.; Di Gioacchino, D.; Tripodi, P.; Brigatti, M.; Mottana, A.; Laguna Marco, M. *J. Phys. Chem. Solids* **2004**, *65*, 1491–1500.

[134] Erenburg, S. B.; Bausk, N. V.; Lavrenova, L. G.; Mazalov, L. N. *J. Synchrotron Rad.* **1999**, *6*, 576–8.

[135] Minh, N. Q. *J. Am. Ceram. Soc.* **1993**, *76*, 563–588.

[136] Siemons, M.; Simon, U. *Sens. Actuators, B* **2007**, *126*, 181–186.

[137] Niu, X.; Li, H.; Liu, G. *J. Mol. Catal. A* **2005**, *232*, 89–93.

[138] Peña, M. A.; Fierro, J. L. *Chem. Rev.* **2001**, *101*, 1981–2017.

[139] Li, X.; Tang, C.; Ai, M.; Dong, L.; Xu, Z. *Chemistry of Materials* **2010**, *22*, 4879–4889.

[140] Didosyan, Y.; Hauser, H.; Reider, G.; Nicolics, J. *Proc. IEEE Sensors* **2004**, 1032–1035.

[141] Brinks, H.; Fjellvå g, H.; Kjekshus, A.; Hauback, B. *J. Solid State Chem.* **2000**, *150*, 233–249.

[142] Iglesias, M.; Rodríguez, A.; Blaha, P.; Pardo, V.; Baldomir, D.; Pereiro, M.; Botana, J.; Arias, J.; Schwarz, K. *J. Magn. Magn. Mater.* **2005**, *290-291*, 396–399.

[143] Xu, G.; Ming, W.; Yao, Y.; Dai, X.; Zhang, S.-C.; Fang, Z. *Europhys. Lett.* **2008**, *82*, 67002.

[144] Liferovich, R. P.; Mitchell, R. H. *J. Solid State Chem.* **2004**, *177*, 2188–2197.

[145] Marezio, M.; Remeika, J. P.; Dernier, P. D. *Inorg. Chem.* **1968**, *7*, 1337–1340.

[146] Marezio, M.; Remeika, J. P.; Dernier, P. D. *Acta Crystallogr. B* **1970**, *26*, 590–597.

[147] Zhao, J.; Ross, N. L.; Angel, R. J. *Acta Crystallogr. B* **60**, 263–271.

[148] Navarro, M. C.; Pannuzio-Miner, E. V.; Pagola, S.; Gomez, M. I.; Carbonio, R. E. *J. Solid State Chem.* **2005**, *178*, 847–854.

[149] Sosnowska, I.; Fischer, P. *J. Less-Common Met.* **1985**, *111*, 109–111.

[150] Sangaletti, L.; Depero, L. E.; Allieri, B.; Nunziante, P.; Traversa, E. *J. Eur. Ceram. Soc.* **2001**, *21*.

[151] Dann, S. E.; Currie, D. B.; Weller, M. T.; Thomas, M. F.; Al-Rawwas, A. D. *J. Solid State Chem.* **1994**, *109*, 134–144.

[152] Sirota, N. N.; Karavai, A. P. *Vestsi Akademii Navuk Belaruskai SSR, Serya Fizika-Matematychnykh Navuk* **1978**, *2*, 74.

[153] Shannon, R. D. *Acta Crystallogr., Sect. A: Found. Crystallogr.* **1976**, *32*, 751–767.

[154] Lyubutin, I. S.; Dmitrieva, T. V.; Stepin, a. S. *J. Exp. Theor. Phys.* **1999**, *88*, 590–597.

[155] Bombik, A. *J. Magn. Magn. Mater.* **2003**, *257*, 206–219.

[156] Solovyev, I. *J. Magn. Magn. Mater.* **2004**, *268*, 194–197.

[157] Prellier, W.; Smolyaninova, V.; Biswas, A.; Galley, C.; Greene, R.; Ramesha, K.; Gopalakrishnan, J. *J. Phys. Condens. Matter* **2000**, *12*, 965–973.

[158] Millis, A. J. *Nature* **1998**, *392*, 147–150.

[159] Yousif, S. E. A.; Yassin, O. *J. Alloys Compd.* **2010**, *506*, 456–460.

[160] Rao, G.; Liu, G.; Feng, X.; Zhang, Q.; Liang, J. *Sci. Technol. Adv. Mater.* **2005**, *6*, 750–754.

[161] Jalili, H.; Heinig, N.; Leung, K. *Phys. Rev. B* **2009**, *79*, 1–8.

[162] Kobayashi, K.-I.; Okuda, T.; Tomioka, Y.; Kimura, T.; Tokura, Y. *J. Magn. Magn. Mater.* **2000**, *218*, 17–24.

[163] Ray, S.; Kumar, A,; Majumdar, S.; Sampathkumaran, E.V.; Sarma, D. *J. Phys. Condens. Matter* **2001**, *13*, 607–616.

[164] Dinia, A.; Vénuat, J.; Colis, S.; Pourroy, G. *Catal. Today* **2004**, *89*, 297–302.

[165] Liao, X. Z.; Sharma, A.; Wei, M.; MacManus-Driscoll, J. L.; Branford, W.; Cohen, L. F.; Bugoslavsky, Y.; Zhu, Y. T.; Peterson, D. E.; Jiang, Y. B.; Xu, H. F. *J. Appl. Phys.* **2004**, *96*, 7747.

[166] Kang, J.-S.; et al. *Phys. Rev. B* **2002**, *66*, 4–7.

[167] López, C. A.; Viola, M. D. C.; Pedregosa, J. C.; Alonso, J. A.; Fernández-Díaz, M. T. *Eur. J. Inorg. Chem.* **2010**, *2010*, 4110–4120.

[168] Jette, E. R.; Foote, F. *J. Chem. Phys.* **1932**, *1*, 29–36.

[169] Chi, L.; Green, A.; Hammond, R.; Wiebe, C.; Greedan, J. *J. Solid State Chem.* **2003**, *170*, 165–175.

[170] Holland, T. J. B.; Redfern, S. A. T. *Mineral. Mag.* **1997**, *61*, 65–77.

[171] Heald, S. M.; Brewe, D. L.; Stern, E. A.; Kim, K. H.; Brown, F. C.; Jiang, D. T.; Crozier, E. D.; Gordon, R. A. *J. Synchrotron Rad.* **1999**, *6*, 347–9.

[172] Ravel, B.; Newville, M. *J. Synchrotron Rad.* **2005**, *12*, 537–41.

[173] Kuepper, K.; Raekers, M.; Taubitz, C.; Hesse, H.; Neumann, M.; Young, A. T.; Piamonteze, C.; Bondino, F.; Prince, K. C. *J. Appl. Phys.* **2008**, *104*, 036103.

[174] Yokoi, K.; Matsubayashi, N.; Miyanaga, T.; Watanabe, I.; Murata, K.; Ikeda, S. *Chem. Lett.* **1987**, 1453–1456.

[175] Samuel, P. P.; Horn, S.; Döring, A.; Havelius, K. G. V.; Reschke, S.; Leimkühler, S.; Haumann, M.; Schulzke, C. *Eur. J. Inorg. Chem.* **2011**, *2011*, 4387–4399.

[176] Yan, H.; Mayanovic, R. A.; Anderson, A. J.; Meredith, P. R. *Nucl. Instrum. Methods Phys. Res., Sect. A* **2011**, *649*, 207–209.

[177] Bernuy-Lopez, C.; Allix, M.; Bridges, C. A.; Claridge, J. B.; Rosseinsky, M. J. *Chem. Mater.* **2007**, *19*, 1035–1043.

[178] Leisegang, T.; Levin, A. A.; Walter, J.; Meyer, D. C. *Cryst. Res. Tech.* **2005**, *40*, 95–105.

[179] Kuzmin, A.; Purans, J. *J. Phys. Condens. Matter* **2000**, *12*, 1959–1970.

[180] Wang, H. *J. Cryst. Growth* **2001**, *226*, 261–266.

[181] Nagai, I.; Shirakawa, N.; Ikeda, S.-I.; Iwasaki, R.; Nishimura, H.; Kosaka, M. *Appl. Phys. Lett.* **2005**, *87*, 024105.

[182] Parasyuk, O.; Olekseyuk, I.; Piskach, L.; Volkov, S.; Pekhnyo, V. *J. Alloys Compd.* **2005**, *399*, 173–177.

[183] Garg, G.; Ramanujachary, K.; Lofland, S.; Lobanov, M.; Greenblatt, M.; Maddanimath, T.; Vijayamohanan, K.; Ganguli, A. *J. Solid State Chem.* **2003**, *174*, 229–232.

[184] Bonazzi, P.; Bindi, L.; Bernardini, G. P.; Menchetti, S. *Can. Mineral.* **2003**, *41*.

[185] Chianelli, R. R.; Scanlon, J. C.; Thompson, A. H. *Mater. Res. Bull.* **1975**, *10*, 1379–1382.

[186] Keller-Besrest, F.; Collin, G. *J. Solid State Chem.* **1990**, *84*, 194–210.

[187] Hu, Y. F.; Coulthard, I.; Chevrier, D.; Wright, G.; Igarashi, R.; Sitnikov, A. *AIP Conf. Proc.* **2010**, *1234*, 343–346.

[188] Andersen, O.; Jepsen, O. *Phys. Rev. Lett.* **1984**, *53*, 2571–2574.

[189] Arezki, B.; Schwarz, G.; Bodenthin, Y.; Luetzenkirchen-Hecht, D.; Markert, C.; Wagner, R.; Frahm, R.; Kurth, D. G.; Pietsch, U. *ChemPhysChem.* **2011**, *12*, 405–10.

[190] Kim, M. G.; Cho, H. S.; Yo, C. H. *J. Phys. Chem Solids* **1998**, *59*, 1369–1381.

[191] Joseph, B.; Iadecola, A.; Simonelli, L.; Mizuguchi, Y.; Takano, Y.; Mizokawa, T.; Saini, N. L. *J. Phys. Condens. Matter* **2010**, *22*, 485702.

[192] Briois, V.; Sainctavit, P.; Long, G. J.; Grandjean, F. *Inorg. Chem.* **2001**, *40*, 912–918.

[193] Della Longa, S.; Pin, S.; Cortès, R.; Soldatov, a. V.; Alpert, B. *Biophys. J.* **1998**, *75*, 3154–62.

[194] Allred, A. L.; Rochow, E. G. *J. Inorg. Nucl. Chem.* **1958**, *5*, 264–268.

[195] Menil, F. *J. Phys. Chem Solids* **1985**, *46*, 763–789.

[196] Etourneau, J.; Portier, J.; Menil, F. *J. Alloys Compd.* **1992**, *188*, 1–7.

[197] Negishi, H.; Negishi, S.; Sasaki, M.; Inoue, M.; Ohara, S. *Mol. Cryst. Liq. Cryst. Sci. Technol., Sect. A* **2000**, *341*, 63–68.

[198] Yamasaki, T.; Suzuki, N.; Motizuki, K. *J. Phys. C: Solid State Phys.* **1987**, *20*, 395–404.

[199] De Groot, F.; Grioni, M.; Fuggle, J.; Ghijsen, J.; Sawatzky, G.; Petersen, H. *Phys. Rev. B* **1989**, *40*, 5715–5723.

[200] Solomon, E. I.; Hedman, B.; Hodgson, K. O.; Dey, A.; Szilagyi, R. K. *Coord. Chem. Rev.* **2005**, *249*, 97–129.

[201] Rose Williams, K.; Hedman, B.; Hodgson, K. O.; Solomon, E. I. *Inorg. Chim. Acta* **1997**, *263*, 315–321.

[202] Soldatov, A. V.; Kravtsova, A. N.; Fleet, M. E.; Harmer, S. L. *J. Phys. Condens. Matter* **2004**, *16*, 7545–7556.

[203] Wu, Z.; Ouvrard, G.; Moreau, P. *Phys. Rev. B* **1997**, *55*, 9508–9513.

[204] Kutzler, F. W.; Natoli, C. R.; Misemer, D. K.; Doniach, S.; Hodgson, K. O. *J. Chem. Phys.* **1980**, *73*, 3274.

[205] Fischer, D. W. *Phys. Rev. B* **1972**, *5*, 4219–4226.

[206] Ishiwata, S.; Kaneko, Y.; Tokunaga, Y.; Taguchi, Y.; Arima, T.-h.; Tokura, Y. *Phys. Rev. B* **2010**, *81*, 4–7.

[207] Ryu, K. S.; Joo, S. J.; Yo, C. H. *Bull. Korean Chem. Soc.* **1994**, *15*, 256–260.

[208] Piña, P. C.; Buentello, R.; Arriola, H.; Nava, E. N. *Hyperfine Interact.* **2008**, *185*, 173–177.

[209] Regier, T.; Krochak, J.; Sham, T.; Hu, Y.; Thompson, J.; Blyth, R. *Nucl. Instrum. Methods Phys. Res., Sect. A* **2007**, *582*, 93–95.

[210] Cressey, G.; Henderson, C.; Laan, G. *Phys. Chem. Miner.* **1993**, *20*.

[211] van der Laan, G.; Kirkman, I. *J. Phys. Condens. Matter* **1992**, *4*, 4189–4204.

[212] Saeki, M.; Onoda, M. *J. Solid State Chem.* **1993**, *102*, 100–105.

[213] Cho, D.-Y.; Oh, S.-J.; Kim, D.; Tanaka, A.; Park, J.-H. *Phys. Rev. B* **2009**, *79*, 1–9.

[214] Jan, J. C.; Tsai, H. M.; Pao, C. W.; Chiou, J. W.; Asokan, K.; Kumar, K. P. K.; Pong, W. F.; Tang, Y. H.; Tsai, M.-H.; Kuo, S. Y.; Hsieh, W. F. *Appl. Phys. Lett.* **2005**, *87*, 012103.

[215] Stöhr, J.; Gland, J.; Eberhardt, W.; Outka, D.; Madix, R.; Sette, F.; Koestner, R.; Doebler, U. *Phys. Rev. Lett.* **1983**, *51*, 2414–2417.

[216] Briois, V.; dit Moulin, C. C.; Sainctavit, P.; Brouder, C.; Flank, A.-M. *J. Am. Ceram. Soc.* **1995**, *117*, 1019–1026.

[217] Jin, G. B.; Ringe, E.; Long, G. J.; Grandjean, F.; Sougrati, M. T.; Choi, E. S.; Wells, D. M.; Balasubramanian, M.; Ibers, J. a. *Inorganic chemistry* **2010**, *49*, 10455–67.